Multifunctional Patchy Silica Particles via Microcontact Printing

---

Marc Zimmermann

Univ.-Diss.

zur Erlangung des akademischen Grades
"doctor rerum naturalium"
(Dr. rer. nat.)
in der Wissenschaftsdisziplin "Kolloidchemie"

eingereicht an der
Mathematisch-Naturwissenschaftlichen Fakultät
Institut für Polymermaterialien und Polymertechnologien
der Universität Potsdam

Ort und Tag der Disputation: Universität Potsdam am 18.04.2019
Hauptbetreuer/in: Prof. Dr. Alexander Böker
2. Gutachter/in: Prof. Dr. Bart Jan Ravoo
3. Gutachter/in: Prof. Dr. Regine von Klitzing

Version: April 17, 2019

Published online at the
Institutional Repository of the University of Potsdam:
https://doi.org/10.25932/publishup-42773
https://nbn-resolving.org/urn:nbn:de:kobv:517-opus4-427731

Diese Forschungsarbeit wurde in der Zeit von April 2015 bis September 2018 am Fraunhofer Institut für Angewandte Polymerforschung IAP in Potsdam durchgeführt. Die Betreuung erfolgte durch Prof. Dr. Alexander Böker.

Amtierender Dekan: Prof. habil. Helmut Elsenbeer, PhD

1. Gutachter/in:	Prof. Dr. Alexander Böker
2. Gutachter/in:	Prof. Dr. Bart Jan Ravoo
3. Gutachter/in:	Prof. Dr. Regine von Klitzing

Love,

it will not betray you dismay or enslave you, it will set you free!

Be more like the man you were made to be.

Marcus Mumford

Contents

List of Abbreviations

µCP Microcontact printing

µm Micrometer (1×10^{-6} m)

2D two-dimensional

3D three-dimensional

$\boldsymbol{A_f}$ Patch surface area

AAP Arylazopyrazoles

AFM Atomic force microscopy

APTES (3-Aminopropyl)triethoxysilane

CD Cyclodextrin

$\boldsymbol{d_x}$ Patch diameter of particle size x

DPP Double patched particles

$\boldsymbol{E}$ Elastic modulus

e.g. exempli gratia (lat.) - for example

$\boldsymbol{e_x}$ Calculated error of PSD influence

EDC *N*-(3-Dimethylaminopropyl)-*N'*-ethylcarbodiimide hydrochloride

et al. et alii (lat.) - and others

$\boldsymbol{F}$ Force

FITC Fluorescein isothiocyanate

FM Fluorescence microscopy

$\boldsymbol{h}$ Height

$\boldsymbol{h_0}$ Height (Wrinkle model)

IEP Iso-electric point

$\boldsymbol{K_a}$ Acid dissociation constant

kHz Kilohertz (1×10^3 Hz)

$\boldsymbol{\lambda}$ Wavelength (Wrinkle model)

LED Light emitting diode

LOC Lab-on-a-chip

$\vec{m}$ Vector of magnetic dipole

mbar Millibar (1×10^{-3} bar)

min Minute

MNP Magnetic nanoparticles

MPP Multi patched particles

NHS *N*-Hydroxysuccinimide

nm Nanometer (1×10^{-9} m)

PAA Polyacrylic acid

PBS Phosphate buffered solution

PDMS Polydimethylsiloxane

PEI Polyethylenimine

pH Negative common logarithm of the hydrogen ion activity

PSD Particle size distribution

QD Quantum dots

R Ratio between larger and smaller patch diameter

R_q Root mean squared roughness

RBITC Rhodamin B isothiocyanate

s Second

SEM Scanning electron microscopy

SPP Single patched particles

t_x Patch thickness of particle size x

USB Ultrasonic bath

$v_e(x)$ Echting speed for patch diameter x

w Width

W Watt

wt% Weight percentage

XPS X-ray Photoelectron Spectroscopy

Y_x Patch yield of particle size x

ν Poisson ratio

σ Swelling degree

List of Figures

List of Tables

CHAPTER 1

Introduction

The first steps working on a new chemical topic are often accompanied by an extensive literature research, finding the necessary tools and knowledge to achieve your task or grasp ideas to create a completely new path. The same situation has been the starting point for this work. But during this enquiry the overwhelming amount of possible solutions was the inception for the very fundamental idea of this thesis and the most important motivation: It should be simpler.

Some of the most important research topics in the field of nanotechnology are focused on the synthesis, modification and assembly of colloids in the size range of micrometers down to double-digit nanometer sized objects.[1–4] Beginning with isotropic particles, the simplest way for the production of colloidal assemblies is the aggregation of objects in a gel or a solid phase.[5] While these microstructures are usually disordered and fractal-like, they are easy to apply and basic starting materials, like polystyrene spheres, can be used.[6] A higher degree of organisation in these systems leads to three-dimensional colloidal crystals which are producible by concentration of monodisperse spherical particles using sedimentation, centrifugation and electrophoretic deposition.[7–9] These materials possess uniform pores and exceptional optical properties.[10,11] Two-dimensional particle films can be produced by using oppositely charged surfaces for random sequential adsorption with various densities or targeted binding using biomolecules.[12,13] The crystallisation of colloids at a moving meniscus, named convective assembly, is useful for large scale deposition.[14–16] Another possibility is the adsorption of particles at a free liquid interface comparable to the Langmuir approach for molecular self-assembly.[17–19] Some of these techniques have been used for the creation of diodes or solar cells.[20] The production of one-dimensional structures using isotropic particles can be achieved using electric fields.[21–23] These structures are limited in extend and formation in two dimensions, while expanding into a single direction. Similar

results can be achieved using template assisted deposition of colloids such as wrinkled and patterned structures[24,25] or the precise surface functionalization of substrates.[26] However, microfluidic devices as used in lab-on-a-chip approaches (LOC) represent a more elegant way for the manipulation of particles, but lack a high throughput.[27,28] To further increase the self-assembling potential of colloids into more complex structures, it is not enough to apply external stimuli for alignment, but to introduce direction-dependent interactions onto potential building blocks.[29,30] These anisotropic colloids, commonly referred to as Janus particles named after the two-faced Roman god or simply patchy particles, possess at least two distinct chemical or physical properties on their surface.[31,32] This potential can be utilized to induce self-assembly on the building block level, rather then applying an external force. Such an approach can result in a vast selection of feasible structures.

The resulting synthesis procedures are as numerous as they are diverse and imaginative (see Fig. 1.1). A straightforward approach is the usage of liquid two-phase systems with surface active colloids. This method allows to selectively choose one phase for surface modification reactions, leading to anisotropic particles such as modified silica particles or magnetic polymer composites.[33–36] This procedure provides considerable up-scaling potential and it can adjust the Janus balance by using different solvent systems. However, the patch number and geometry are fixed parameters. Another technique is used to deposit particles on suitable flat substrates, thereby shielding the underlying surface from deposition of polyelectrolytes or even DNA.[37–39] Furthermore, it is possible to link different etching and annealing steps, assisted by shielding with sacrificial layers, to generate multivalent polymer or silica particles.[40,41] These methods are able to produce multivalent particles, but are bound to difficult and time consuming treatment steps (e.g. thermal treatment, reactive ion etching). The application of various wrinkled structures on the other hand enables the tuned deposition of gold nanoparticles onto silica spheres by adjusting the embedment of the particles.[42] It is however also limited to divalent colloids. The deposition of thin metal layers onto micro- or nanospheres is typically achieved by glancing angle or electron-beam assisted deposition.[43–45] The produced particles can obtain gold, chromium and nickel coatings. Alternatively, it is also possible to deposit organic macromolecules to produce polymer patches.[46] Research groups have shown a broad selection of patch numbers and geometries using these techniques, although there are limits concerning their up-scaling performance. A different approach utilizes small organic or inorganic

particles for further seed mediated nucleation and growth polymerization.[47–52] It enables the production of anisotropic particles with a modulus or roughness gradient and furthermore magnetic or plasmonic properties due to their initial seed. A related technique uses the phase separation during copolymerization of monomers inside a swollen polymeric colloid to create an anisotropic surface.[53,54] Due to varying swelling behaviours in solvents or changing pH response of the components, different geometries can be realised using these particles. Additionally, controlled chemical surface modification is feasible. Although a high reproducibility and up-scaling potential is given, starting materials are relatively specific (e.g. blockcopolymers). The description and production of regular particle clusters opened the way for another seed mediated approach.[55] By forming differently sized starting structures and subsequent encapsulation using polymerizable silanes, the production of divalent building blocks with increasing number of patches is possible.[56–58] The limiting factor of this technique is the purification and isolation step, which is commonly conducted using analytical centrifuges. Such a set-up is able to separate single cluster types for further modification. To achieve smaller patchy particles the synthesis and self-assembly of triblock terpolymers shows very promising results.[59,60] It was even shown to adjust geometry and valency of the achieved colloids, by using different solvents feasible for single blocks.[61] However, the synthetical effort is very large in comparison to other approaches.

As most of the previously mentioned techniques are conducted in liquid, microcontact printing (μCP) is a more direct concept by applying chemicals, or inks, directly onto the dry colloid surface. Sometimes this stamping technique was used for the simple removal of excess particles, to produce an uniform monolayer.[62] Furthermore, this approach was used to apply silanes directly onto silica particles for subsequent adsorption of gold nanoparticles onto the created patches and additionally it was shown how the elasticity of the used stamping materials could influence the size of the applied patches.[63] However, in this example it was not possible to further change the geometry of the patches and no particle self-assembly was investigated. Other research groups transferred ATRP initiators onto silica particles to start polymerization directly on the colloid surface for further self-assembly experiments.[64] These systems possess a broad variety of physical properties, namely fluorescence labelled patches, magnetic manipulation of the colloids and light-responsive coupling, but are synthetically very demanding and long production times are required. The flexibility of the microcontact printing process was meanwhile shown for various inks and also proteins,

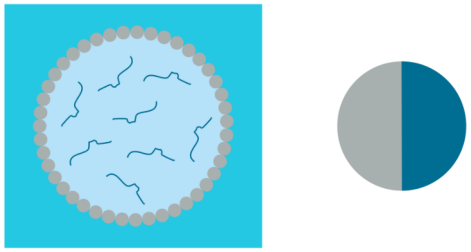

(a) Two Phase System[34]

(b) Particle Shielding[38]

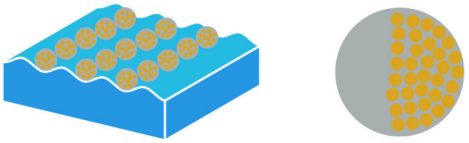

(c) Structured Templates[42]

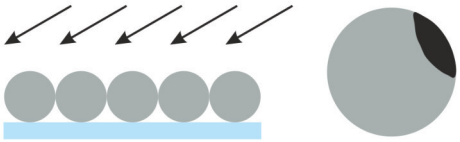

(d) Glancing Angle Deposition[43]

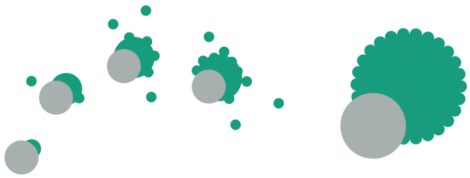

(e) Seed Mediated Nucleation[48]

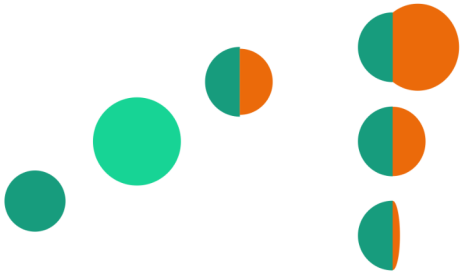

(f) Copolymerisation in Seeds[53]

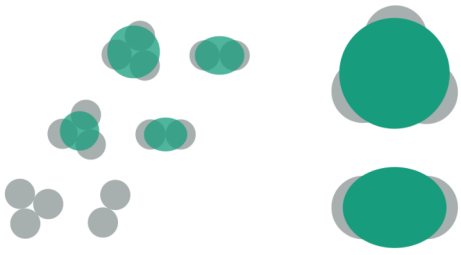

(g) Cluster Encapsulation[57]

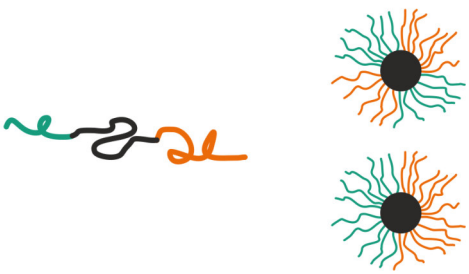

(h) Assembly of Triblock Terpolymers[61]

Figure 1.1 Overview of established synthesis routes for anisotropic colloids.

which were applied onto organic and inorganic particles.[65–68] In comparison to previously mentioned techniques, microcontact printing possesses a high precision and reproducibility. Nevertheless, synthesis routes for μCP procedures mentioned here are still too complex, time consuming and expensive for reasonable up-scaling.

Motivation

The driving force behind this research was to find a very basic system which shows the same precision and reproducibility for the production of multivalent anisotropic colloids as previously mentioned systems. It should be possible to use different ink systems, change patch geometry and number as printing should be conducted on different sized particle spheres. However, to furthermore access a robust up-scaling, additional simplifications to the systems have to be made in comparison to other microcontact printing concepts. Starting materials have to be accessible, relatively cheap or should possess at least a simple synthesis route. In consideration of these factors, the self-assembly potential, using different chemical and physical approaches, should still be feasible.

Outline of this Research

The presentation of the results starts in chapter 2 with a detailed introduction of the investigated microcontact printing approach together with materials, procedures and the underlying mechanisms followed by the analytical methods required for particle characterization. The subsequent chapter 3 will describe the results concerning anisotropic particles with special attention to the accomplished patch geometries for single and double patched particles. Chapter 4 will discuss the applied physical and chemical coupling systems including their functionality and applicability. To further understand and discuss the results a couple of mathematical evaluations will be presented in chapter 5. The same chapter will introduce a new mechanical approach for the production of anisotropic particles via microcontact printing using centrifugal forces. Finally, a conclusion of the received results is given in chapter 6, which is followed by the materials and methods section in chapter 7 describing all applied procedures and calculations in detail.

CHAPTER 2

The Microcontact Printing Approach

The production of anisotropic particles by microcontact printing would not have been possible, without the right choice of materials and their precise interaction. Due to this requirement, it is only fair to dedicate this first part to the general process, elucidation of components, explanation of mechanisms and the introduction of key parameters which are needed to evaluate the quality of this process. The mechanisms behind this approach open the way for new innovative aspects of this otherwise well-known approach.

2.1 A Process Overview

In the beginning of this research strategic objectives were determined to narrow the selection of chemical materials. The goal was to obtain a simple, fast and economic method for the preparation of multifunctional patched particles, with the potential for future up-scaling[69] while retaining a high quality, particle yield and excellent control over the patch geometry. The μCP process, as illustrated in Fig. 2.1, is divided into three major steps: Loading of the stamp material with ink, the printing process and release of modified particles from the stamp. Necessary for achieving those steps are a soft stamping material, a reliable and flexible ink system, suitable particles with a broad size range, and a convenient release method.

The soft stamping material polydimethylsiloxane (PDMS) is a very common material for μCP, relatively cheap and easy to use.[70–74] There is a large selection of different surface functionalizations using silanization, patterning techniques via moulding and simple variation of the composition to change its properties. Thus, it is an ideal material for this approach and future applications.[75–79] Particles for surface functionalization are divided into two groups: organic and inorganic particles. There is a considerable amount of synthesis procedures for organic patchy particles.[43,80,81] However, incompatibility with

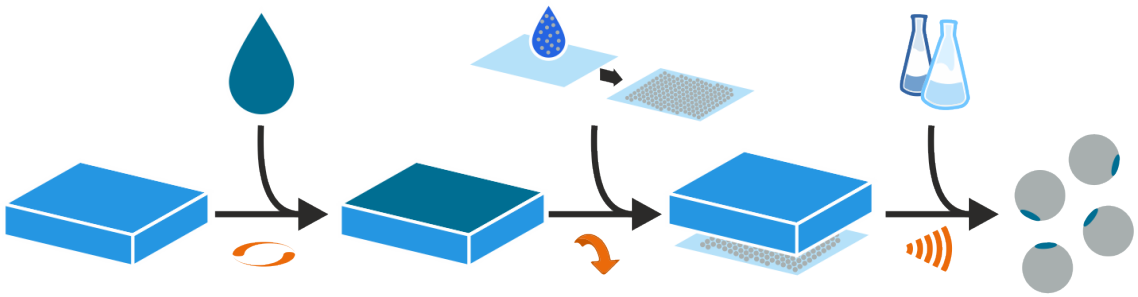

Figure 2.1 Illustration of the microcontact printing approach. From left to right: Production of PDMS stamps loaded with different concentrated polymer solutions; drop casting of silica particle dispersion on cleaned glass substrates for monolayer creation; printing process and solvent assisted particle release from stamp using ultrasonic treatment.

different solvents could be a problem for further applications. Spherical inorganic particles consisting of noble metals are expensive and difficult to synthesize in the size range above 1 µm.[82] During this research a fast characterization should be achieved using light or fluorescence microscopy, which would not be possible using considerable smaller nanospheres. Since the work of Stöber *et al.* silica particles are easily achievable and are commercial available in large amounts.[83] Additionally, they possess a great stability against solvents and temperature.[84,85] Furthermore, the monolayer production on hard substrates (e.g. glass slides) is rather simple. Therefore these particles were chosen for this work. Following the investigations of µCP on flat surfaces the straightforward approach was the usage of molecular inks for the preparation of anisotropic particles.[86] However, these chemicals exhibit in general a low viscosity and therefore are prone to ink diffusion or absorption into porous particle surfaces.[87] Polymeric inks with tunable molecular weight promise to easily circumvent this problem and also have been studied in µCP applications.[88] For this reason a high molecular weight polymer with a great density of functional groups, which is commercially available and not subjected to great synthetic effort was needed.[89] The opportunity of a strong electrostatic bond between the particle surface and the polymeric ink was postulated. Due to these points polyethylenimine (PEI) as a cationic and polyacrylic acid (PAA) as an anionic polyelectrolyte were chosen. Finally, a suitable particle release method was needed. In general the silica particles will stick to the loaded stamp after the printing procedure. The reason for this behaviour, is a stronger attraction between ink and particle surface in comparison to the glass substrate. This fact is true for molecular[88] and polymeric inks.[89] Commonly a solvent assisted particle release is conducted using an ultrasonic bath.[90] Although this sounds quite simple, it is an essential step during

this investigation and will be discussed, as all components, in detail during the following sections.

2.2 Polydimethylsiloxan as Stamping Material

PDMS is a flowable transparent silicone elastomer, which is commercially available under the brand name *Slygard 184*. It is sold as a preparation kit consisting of two liquids: the monomer and a crosslinking agent. Its main application fields are LED lighting encapsulation, power supplies, connectors, sensors and high voltage resistors packs.[91] Furthermore it has great use in the field of microfluidics[92] and as stamping material for microcontact printing.[93] The monomer liquid is actually a mixture of two polymeric compounds, namely dimethylmethylhydrogen siloxane (trimethylsiloxy terminated) and dimethyl siloxane (dimethylvinylsiloxy terminated).[94] The curing agent contains a platinum component catalysing the addition reaction between the polymer chains (compare Fig. 2.2) and therefore creating an elastic network. The velocity of this crosslinking process can be elevated significantly by increasing the temperature after mixing the two components.

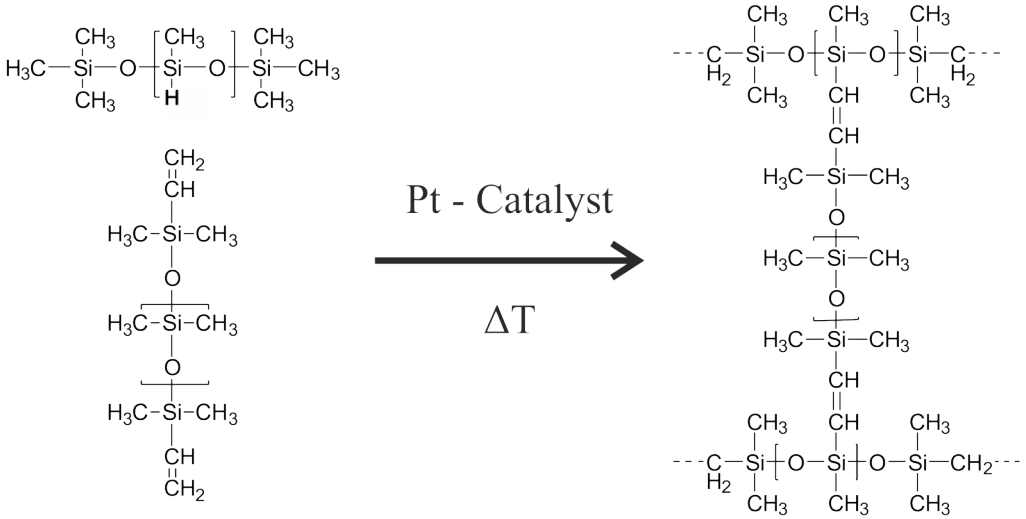

Figure 2.2 Reaction scheme displays the crosslinking event between the two polymer components during the addition of platinum catalyst.

Fig. 2.3 displays the general synthesis procedure for PDMS stamps. After mixing the two components, the liquid needs to be degassed to prevent encapsulation of air bubbles which could deform the surface or influence the mechanical properties. After this, the polymer is cured at elevated temperatures enabling complete crosslinking throughout the material. The flat air-liquid interface is used as the stamping side for all experiments.

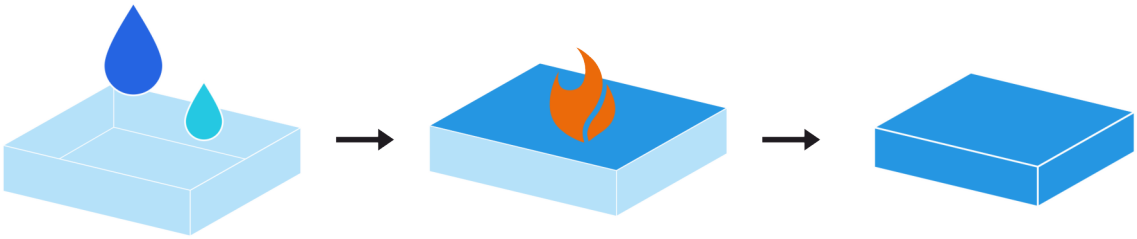

Figure 2.3 Schematic of the synthesis procedure of polydimethylsiloxane stamps.

AFM was used to determine the roughness of the product and is displayed in Fig. 2.4(a). Although the AFM image shows a relatively smooth surface, further improvement was achieved using another synthesis route. This process is described in more detail in section 8.2.1, but includes the modification of silica wafers and the moulding of said flat surface. Admittedly, the AFM image in Fig. 2.4(b) shows two impurities. However the irregularities of the overall surface have been minimized even further. This approach was chosen, to exclude any interference between the roughness of the PDMS stamp and loading the ink using spin coating, or the general μCP process.

Due to the high amount of methyl groups on the stamp surface, they possess a hydrophobic character and are therefore not accessible for water based inks (e.g. PEI). For the introduction of hydrophilic groups air plasma treatment was used resulting in a thin silicon oxide layer on top of the stamp.[95] After this process loading of stamps with water solutions via spin-coating was feasible.

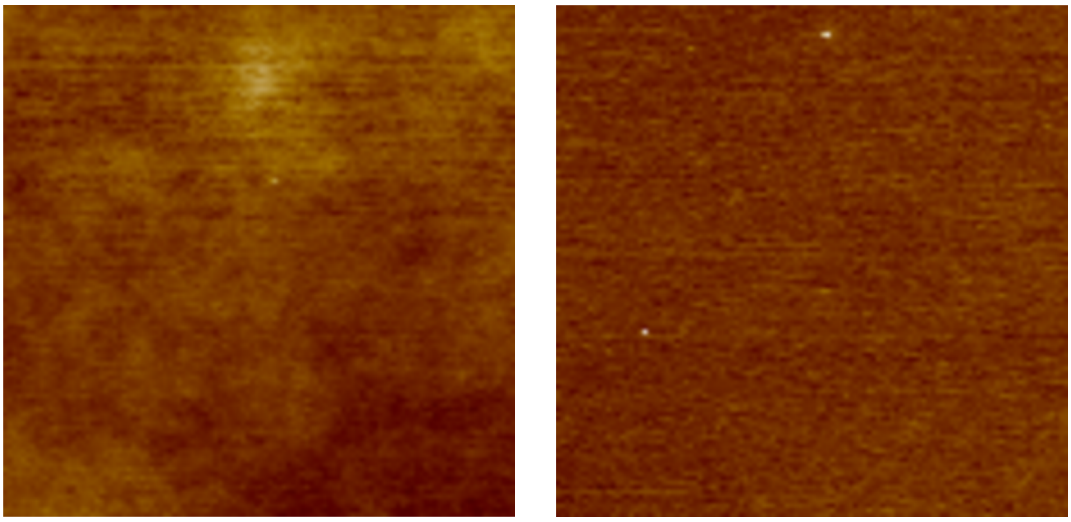

(a) PDMS surface (b) Flat PDMS surface

Figure 2.4 AFM height images with a size of 20 x 20 μm^2: First measurement shows the air-liquid interface normally formed (R_q = 0.769 nm) and the second shows the flat PDMS interface after moulding of a modified silica wafer (R_q = 0.489 nm). Height scale 20 nm

2.3 Preparation of Wrinkled Stamps using Air Plasma[†]

Additionally to flat unstructured PDMS substrates, structured stamps were introduced to the μCP process. A well-known procedure of PDMS structuring operates with the same air plasma treatment mentioned above.[78] As illustrated in Fig. 2.5 the PDMS stamp will be constantly elongated into one dimension while exposing it to air plasma. After the process the PDMS stamp will be released and wrinkles are forming on the surface.

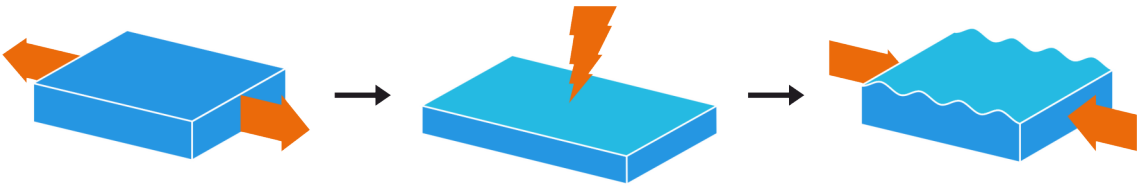

Figure 2.5 Wrinkle structuring of PDMS stamps using air plasma treatment.

These structures occur during the presence of at least two superimposed layers, with differing modulus of elasticity, while being exposed to an increasing or decreasing external stress. In the case of PDMS substrates the first layer consists of a thin inelastic silicon dioxide layer, produced by the plasma treatment, and the second layer represented by the remaining elastic material. Relaxation of external stress is induced during the contraction of the substrate after plasma treatment. There are other published methods for the generation of hard layers on PDMS substrates. For example coating with polymers or polyelectrolyte,[97–99] ozone radiation[100–102] or the deposition of metal films.[79,103,104] Fig. 2.6 illustrates the profile of generated wrinkles including the most important parameters, the periodicity or wavelength λ, the amplitude A and the thickness h_o of the hard oxide layer. Theoretical predictions for the generation of these structures have been made, based on the mechanical properties of the used materials.[78,105] Starting from a thin hard film (height = h_o, width = w) superimposed on a infinite elastic bottom layer without consideration of any sheer forces between the two layers. As material properties only the elastic modulus and the Poisson ratio of the oxide layer (E_o, ν_o) and the substrate (E_s, ν_s) are used. Therefore the compression force F inside the skin is formulated as:

$$F = E_\mathrm{o}\left[\left(\frac{\pi}{\lambda}\right)^2 \cdot \frac{wh_\mathrm{o}}{3(1-\nu_\mathrm{o}^2)} + \frac{\lambda}{\pi}\cdot\frac{E_\mathrm{s}w}{4(1-\nu_\mathrm{s}^2)E_\mathrm{o}}\right] \tag{2.1}$$

[†]The results concerning the research in this section were conducted in cooperation with Daniela John from Fraunhofer IAP.[96]

In this case the wavelength λ indicates a sinusoidal bending profile of the oxide layer along the direction of applied stress acting on the elastic substrate. Wrinkle structuring of the oxide layer only occurs over a critical compression force value F_c, which corresponds to a critical wavelength λ_c obtained by $\frac{dF}{d\lambda}$:

$$\lambda_c = 2\pi h_o \left[\frac{(1-\nu_s^2)E_o}{3(1-\nu_o^2)E_s}\right]^{\frac{1}{3}} \tag{2.2}$$

Equation 2.2 shows that the wavelength of wrinkles is only dependent on material properties of two layers and the thickness h_o of the hard oxide film. The thickness can be changed using different plasma treatment parameters. In general, longer treatment times, higher power usage and a decreased partial oxide pressure during the treatment leads to a thicker oxide layer and therefore longer wavelengths.[87] Nevertheless, it should be mentioned that amplitude and wavelength are connected parameters and therefore cannot be varied independently.

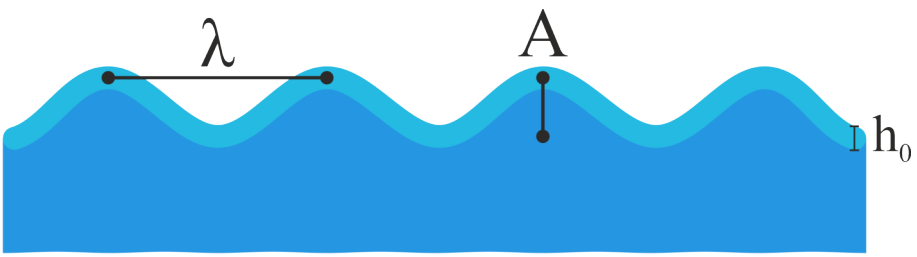

Figure 2.6 The schematic diagram shows the profile of a typical wrinkled PDMS stamp consisting of a thin silicon oxide top layer and the underlying remaining stamp material. Wrinkled structures are characterized by periodicity λ and the amplitude A.

2.4 Silica Particles

The ideal particle choice for the foundation of multifunctional patchy particles was determined almost immediately. Silicon dioxide (silica) spheres are a cheap and reliable commercial product, and they are available in a huge range of different sizes (150 nm - 25 µm).[106] Silica particles have been the subject of several biomedical applications due to their biocompatibility and low toxicity.[107,108] For example as enhancement of ultrasound imaging,[109–111] optical images on cellular level[112] and as carrier material for magnetic nanoparticles[113–116] or radioactive ions.[117–119] There are various synthetic procedures for different silica geometries aiming on distinct implementations: monodisperse silica particles,[120–130] mesoporous silica spheres[131–134] and hollow or core-shell particles.[135–137]

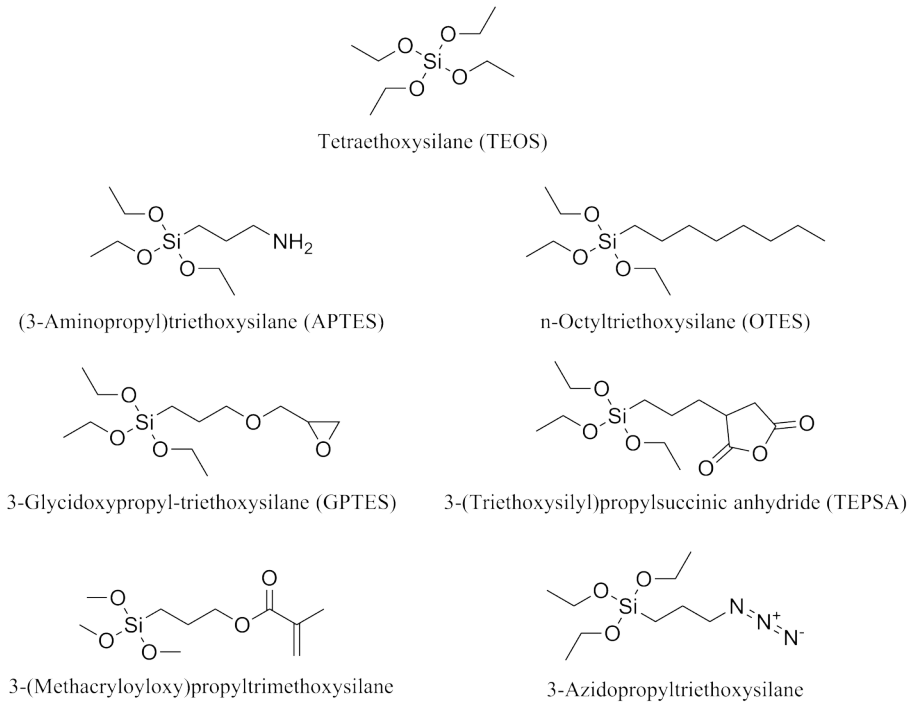

Figure 2.7 Chemical structures and abbreviations of common alkoxysilanes with functional groups for the surface modification of silica particles.

The surface functionalization of silica particles is conveniently achieved with one of many commercially available alkoxy- or halosilanes. Alkoxysilanes bind to silanol groups on the particle surface in a condensation reaction, whereas halosilanes initially undergo a substitution process, changing the halide for an alcohol group, followed by the same condensation.[138] The reactivity of alkoxysilanes decreases with longer alkyl chains, whereas halosilanes exhibit the highest reactivity. These reactions can be executed in alcohols (e.g. methanol or ethanol), under anhydrous conditions using toluene or by chemical vapour deposition under reduced pressure or elevated temperatures.[139,140] Prior to this, an increase of surface silanol groups can be beneficial by boiling the particles in hydrochloric acid[64] or using air plasma treatment. Fig. 2.7 gives a small excerpt of common alkoxysilanes. Tetraethoxysilane should be mentioned separately, because it is starting material for most particles synthesis approaches. In the course of this research several attempts of surface functionalization of silica particles were tested. Initially, prior to the μCP process, functional groups were attached which should undergo a covalent bonding with molecular inks (e.g. TEPSA). Alternatively the surface charge was inverted using APTES enabling the use of anionic inks. The complete coverage of the particle surface with amine groups should shift the isoelectric point to higher pH values. To verify the effect of this functionalization approach, pH dependent zeta potential measurements were conducted.

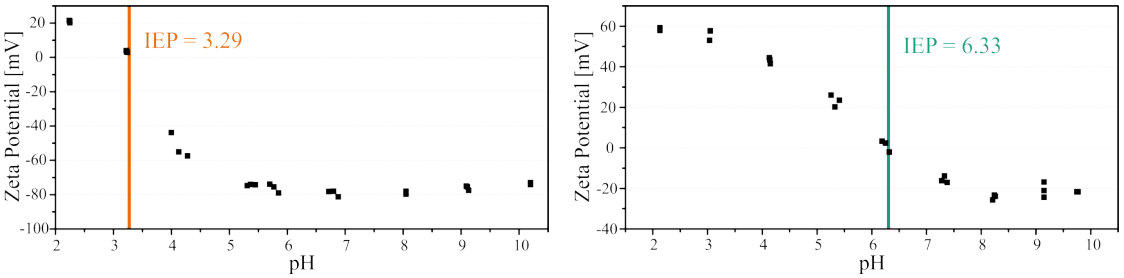

(a) Silica Particles (b) APTES Functionalized Silica Particles

Figure 2.8 Zeta potential measurements of blank and amine functionalized silica particles at increasing pH values for determination of the isoelectric point.

Fig. 2.8(a) shows the zeta potential measurement of unmodified silica particles in a pH range between 2 and 10. The surface potential decreases with increasing pH due to deprotonation of surface silanol groups. At a pH value of 3.3 the graph crosses the zero point into the negative region. This point indicates, that the concentration of protonated and deprotonated silanol groups are in equilibrium. Lower pH values lead to an increase in zeta potential as a majority of surface groups are protonated. This effect will become more important in later discussions (see section 4.1). After the surface functionalization of silica particles using APTES (see section 8.2.5), the same measurement was conducted and the results are shown in Fig. 2.8(b). The shift of the isoelectric point is clearly visible and its location is now at a pH value of 6.3. Following the incorporation of amine groups, the concentration of protonated surface groups at this pH values increased. These results show a successful surface functionalization using alkoxysilanes.

The stability against air plasma treatment is another advantage of silica particles. This method is not only used to increase the hydrophilicity of surfaces, but also to remove organic residues. This effect can be utilized to selectively etch organic layers, which was exploited during this research and will be discussed later (see section 3.2.1).[141] This approach would not been possible using polymeric particles for longer etching times.

Finally, the production of silica particle monolayers was required for the μCP approach. This process is described in detail later (see section 8.2.2). It includes cleaning of glass substrates and drop casting of differently concentrated particles solutions in ethanol. The concentration of the solutions was depended on the size of the used silica particles, as the volume fraction is changing. With this approach, an economical micro- and nanosphere system with flexible surface chemistry for further investigations was found.

2.5 Polyelectrolytes as Inks

On the basis of a very tunable particle system with a versatile surfaces chemistry (compare section 2.4), the choice of an appropriate μCP ink had to be found. As mentioned earlier, an electrostatic connection between the particle surface and the oppositely charged ink should be obtained. To eliminate diffusion and absorption issues a high molecular weight polyelectrolyte with a high density of charged and functionalisable groups with a good commercial availability was targeted.

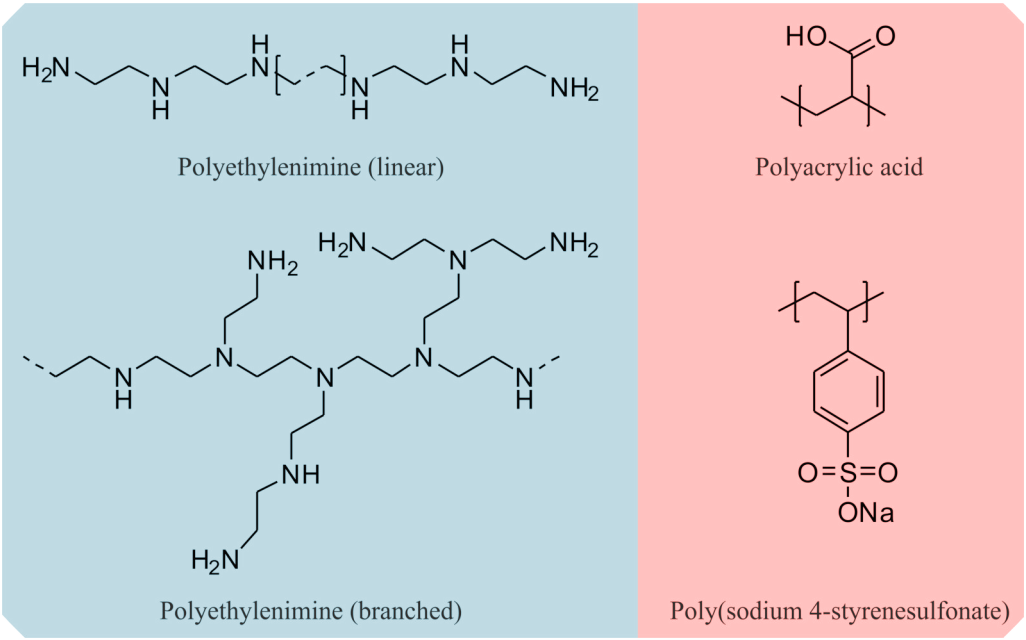

Figure 2.9 Chemical structures of common anionic and cationic polyelectrolytes.

A small selection of cationic and anionic polyelectrolytes for the usage as inks is displayed in Fig. 2.9. The first and most important candidate for this research was polyethylenimine (PEI). It exhibits the highest positive charge density of polyelectrolytes when fully protonated in aqueous solution and thus represents an ideal counterpart for the negatively charged silica surface.[142–148] Due to its unique properties, like its buffering capabilities[149] or pH dependent structure in solution,[150] it is used in a broad range of applications. Its chelating effect is useful in the purification of waste water[151,152] and in the paper industry as flocculation material for negatively charged fibres.[153] Moreover it is used as release nanocarrier[154] and as a DNA delivery tool.[155–158] Different synthesis procedures are available for linear PEI[159,160] using a microwave approach,[161] low temperatures for the reduction of side products[162] and also a patent for a living anionic polymerization route.[163] The synthesis of branched PEI[164,165] has the main advantage of reaching very

high molecular weights by using simple crosslinking techniques.[166] For branched PEI it is possible to include all types of amine groups, whereas linear PEI only possess primary and secondary amines. Theoretical, branched PEI should exhibit a ratio of 1:2:1 for these amine types, however investigations of commercial samples showed a ratio of 1:1:1 which translates into an even higher degree of branching.[167] This finding is not a disadvantage, because a strong entanglement of the polymer chains during the loading step would be beneficial and therefore branched PEI was chosen for the μCP experiments.

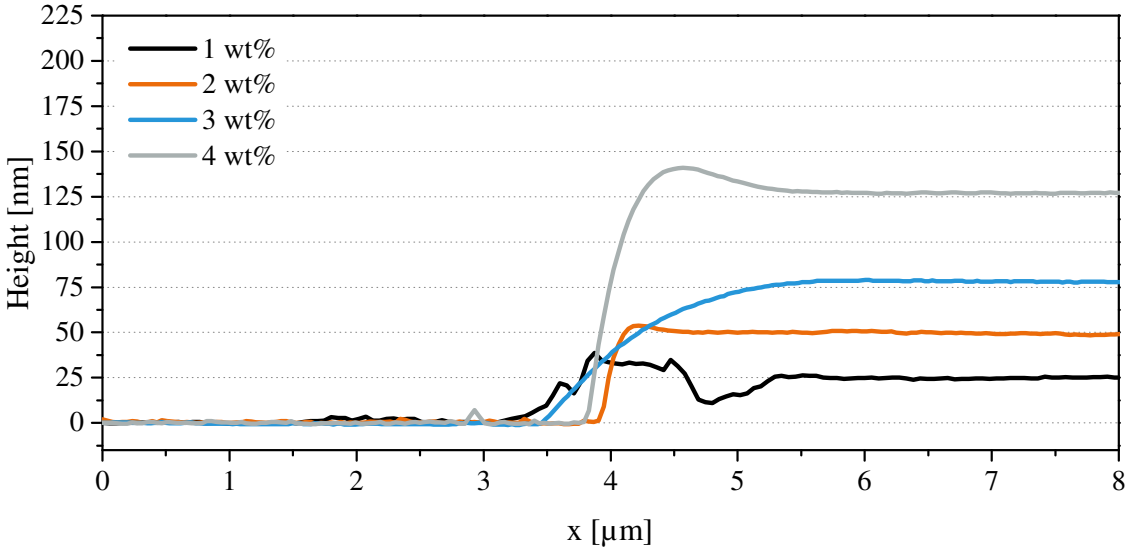

Figure 2.10 Diagrams show the AFM height profile of different concentrated polyethylenimine solutions spin coated onto silica wafers. The scratch was caused by using a syringe cannula which does not penetrated the hard surface.

The stamp loading was conducted by spin coating of PEI solutions on prepared PDMS (see section 8.2.3). To reduce hydrophobicity, the PDMS surface was treated with air plasma and afterwards different diluted aqueous solutions of high molecular weight PEI were spin coated onto the stamp to produce a thin ink layer.[168] To evaluate the thickness of these PEI films, model experiments were conducted using flat silica wafers as substrates. After spin coating the PEI film on top of the silica wafer, the ink was scratched and measured with AFM. Figure 2.10 displays the height profile of four PEI solutions corresponding to a thickness range between 25 nm and 125 nm. During this research, these four concentration were used for all μCP experiements. Although PEI was by far the most used ink during this investigation, experiments with polyacrylic acid (PAA) were also conducted. PAA possesses a high density of accessible carboxyl groups with a $pK_a = 4.5$[169] and is producible by various methods.[170–173] It was used as a negatively charged polyelectrolyte ink.

2.6 Printing Procedure

The next step of the microcontact printing approach was the practical implementation. In this case, it describes the parallel alignment of the silica particle monolayer with the loaded PDMS stamp while applying pressure on the substrates.

First the glass substrate of the particle monolayer was fixated horizontally using a vacuum sample holder. A PDMS stamp loaded with polymeric ink was pressed against the glass substrate and immediately afterwards the two substrates were separated again. This approach does not need any reaction time between the particles and the ink due to its electrostatic nature. Therefore a considerable amount of manufacturing time can be saved using this approach. Higher adhesive forces between silica particles and ink film in comparison to the glass substrate lead to the adherence of the particles to the stamp during lift off. This procedure was conducted by hand and was not guided by a mechanical press. However, the applied pressure during this process was still inspected (see section 8.2.4). At this point the particles were embedded into the polymeric ink film on the PDMS stamp which were afterwards stored dust-free until particle release, which will be discussed in the following, or further modification (compare section 4.5).

2.7 Solvent Assisted Particle Release Mechanism

The release of the silica particles from the loaded stamp was conducted using an ultrasonic bath. This method is commonly used to redisperse micro- and nanoparticles or synthesis smaller particles from powders.[174–180] The functional principle behind this approach is the creation of cavitation bubbles inside a cleaning solvent induced by ultrasound (movement faster than 18 kHz).[181] Cavitation bubbles are small vapour areas inside a liquid, which apply pressure while they are rupturing. The bubble size is dependent on the speed of the applied movement. Typically ultrasonic baths work at a speeds between 20 kHz and 100 kHz and higher values translate into smaller bubbles with reduced rupturing force. The kinetic energy achieved during this treatment interacts with the particles and is responsible for their release. The diameter of the silica spheres used in this work is in general 10 to 200 times larger then the thickness of the polymer layer, depending on ink concentration and particle size. As a consequence of this mismatch the particles will separate easily from the stamp into the surrounding solvent. However, experiments have shown that an

increase of treatment time is necessary for smaller particles or thicker ink films, respectively. The release procedure is pictured in Fig. 2.11. A loaded PDMS stamp after the printing procedure is placed into a closable centrifuge tube. The tube is filled with a suitable solvent, which will be further discussed in the following section 2.8, and then placed into an ultrasonic bath. After 10 to 25 min the tube is removed and the PDMS stamp is carefully extracted from the liquid. If necessary the stamp was dried and stored for further analytical processes (compare section 2.10).

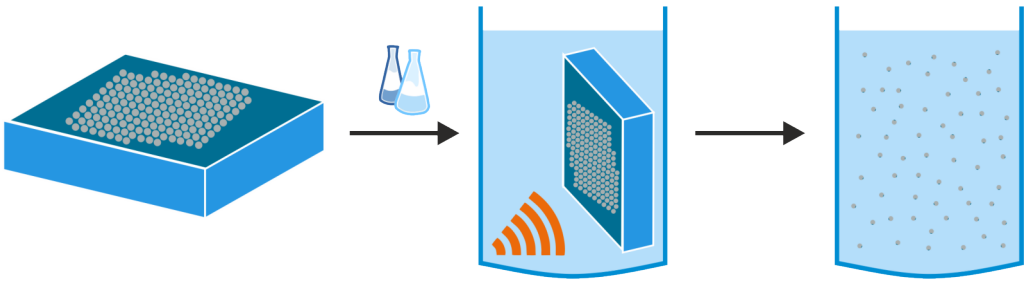

Figure 2.11 Schematic diagram displays the solvent assisted particle release mechanism of silica spheres from a loaded PDMS stamp using an ultrasonic bath. The stamp is removed after the ultrasonic treatment.

The fluorescence microscope images in Fig. 2.12 give first impressions of the resulting single patched particles achieved by this μCP approach. For visualization of the patches FITC was used as labelling agent (compare section 8.2.5). At this point no detailed information about the obtained patch geometry will be given, as it is the main discussion in the following chapter 3. However, another important influence during the particle release will be discussed. Fig. 2.12(a) shows patched particles released at reduced temperature by using ice cooled water in the ultrasonic bath. In contrast to this, particles in Fig. 2.12(b) are released at higher temperatures by using the build-in heating component. It is clearly visible that the quality of the patches received at lower temperature is significantly higher compared to the ones achieved at elevated temperatures. Additionally, multiple residues of free floating PEI are visible at higher release temperature. These residues detach most probably from the PDMS stamp caused by the increasing solubility of the polymeric ink.[182] The application of ultrasound leads to an increase in temperature in the solvent system over time. Therefore it is not sufficient to keep the bath at ambient conditions, but to add ice at the beginning of the process. Following these findings, all μCP experiments in this research were conducted under cooled conditions during the particle release process to improve the patch quality and minimize contaminations inside the particle dispersions.

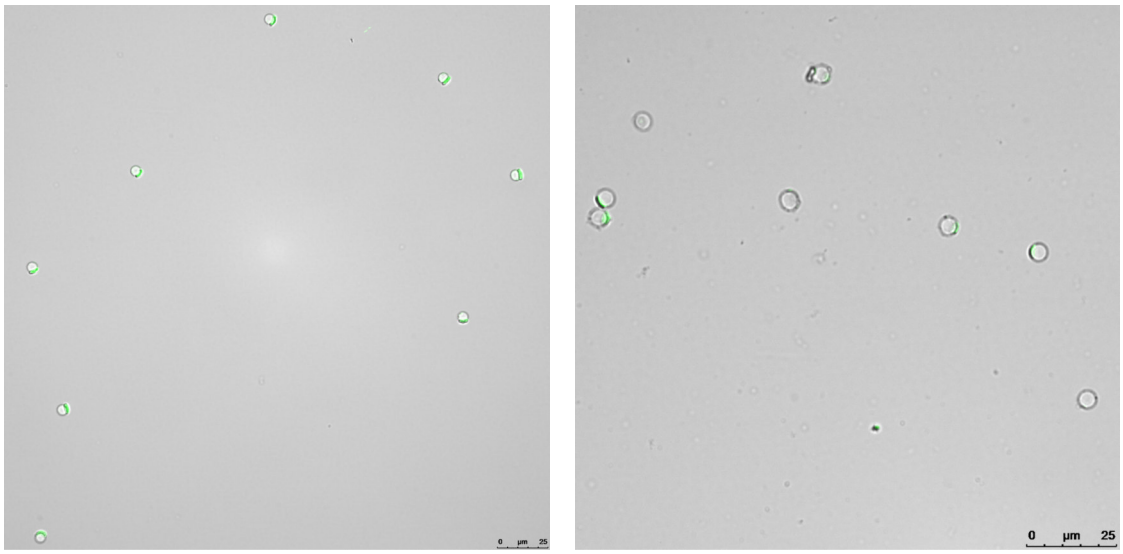

(a) Release at 15 °C (b) Release at 40 °C

Figure 2.12 Fluorescence microscope images show the influence of temperature during the solvent assisted particle release via ultrasonication on the patch quality.

2.8 Switching from 2D Modification to 3D Structure Printing

In the previous section the solvent assisted particle release using ultrasonication was introduced. Additionally, the influence of temperature during this treatment on the patch quality was explained. This section describes the investigations leading to the two chosen release solvent, namely ethanol and acetone, and their distinct contribution to this microcontact printing approach.

The SEM images displayed in Fig. 2.13 show patched particles printed under the same conditions, but released in different solvents. Water was not an option for this experiments as it is a good solvent for PEI[183] and therefore could dissolve the ink layer before the particle release and the formation of patches would not take place. The first experimentally used solvent was ethanol, because it is able to dissolve low molecular weight PEI and it is a common solvent for handling silica particles.[184] Fig. 2.13(a) displays the SEM image of a patched particle released in ethanol and it shows a smooth, thin and symmetrical circular patch on the surface of the silica particle. In the following non-solvents for PEI were tested as release solvent to verify a resulting difference in the patch geometry. One aspect for these non-solvents was the alteration of the PDMS stamp geometry. Several common organic solvents (e.g. toluene, hexane) swell crosslinked PDMS to a significant degree. For this reason three different solvents were chosen, which are non-solvents for PEI and exhibit different swelling degrees for PDMS: toluene ($\sigma = 1.31$), acetone ($\sigma = 1.06$)

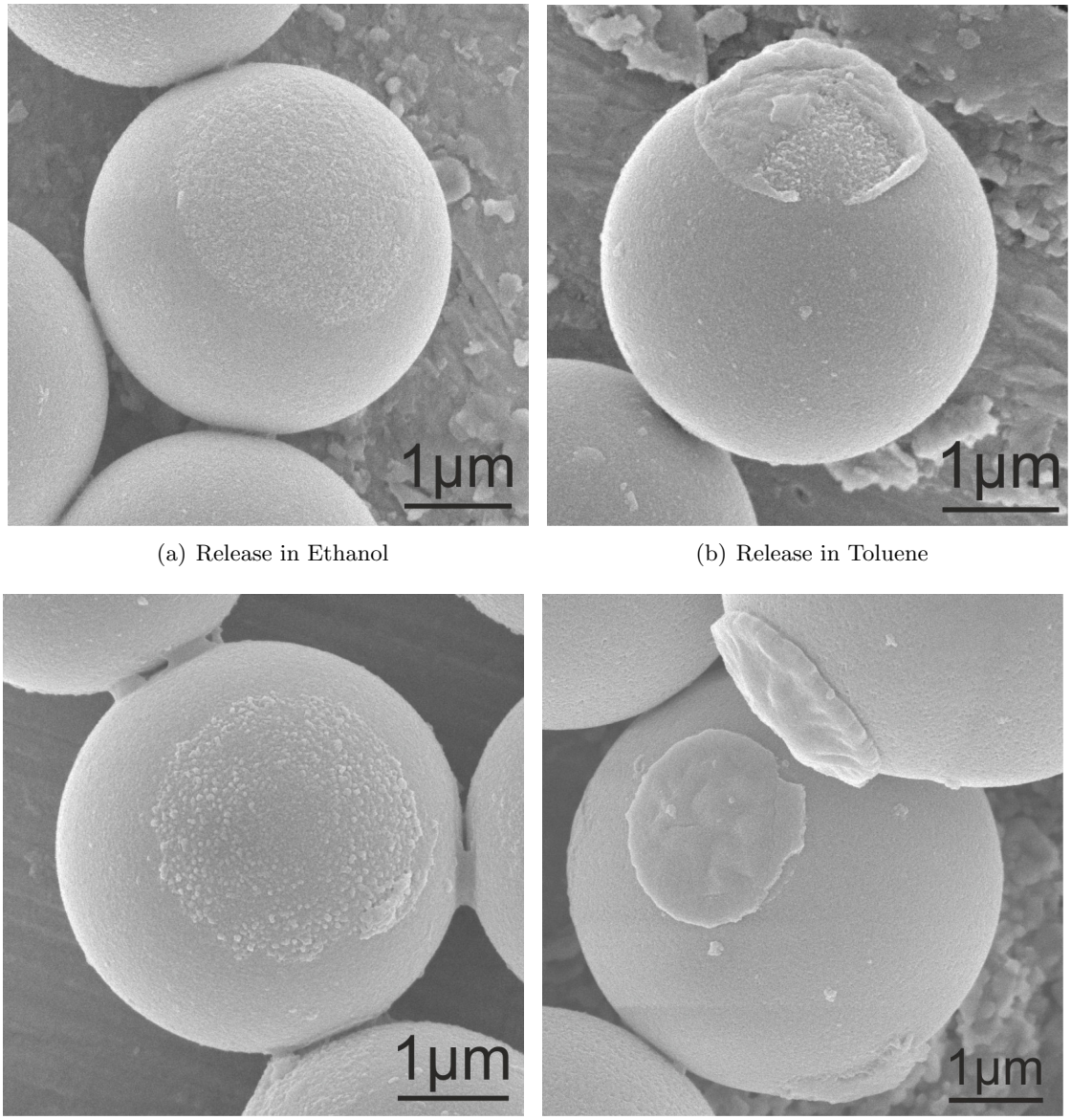

(a) Release in Ethanol

(b) Release in Toluene

(c) Release in Acetonitrile

(d) Realease in Acetone

Figure 2.13 SEM images of silica particles printed with 3 wt% PEI and released in four different solvents to investigate the solvent influence on patch geometry.

and acetonitrile ($\sigma = 1.01$).[185] The result for toluene is displayed in Fig. 2.13(b). The patch shows a slightly thicker but highly irregular shape compared to the release in ethanol. The patch released in acetonitrile in Fig. 2.13(c) reveals a similar geometry compared to the ethanol sample, however its surface is not as smooth. A significant difference is visible for the acetone sample. The patch geometry shows a considerable increase in thickness and an almost plane surface. Repeated experiments confirmed that this observations was reproducible and directly influenced by the chosen release solvent.

The hypothesis for this effect is illustrated in Fig. 2.14. PEI possesses a slight solubility in ethanol,[183] which is capable of penetrating the ink layer during ultrasonic treatment.

Due to this behaviour the particles are able to detach from the stamp while a cohesion fracture inside the PEI film occurs. This detachment takes place in a rather short timespan as a full release of particles was possible within 10 min. In contrast, the release time during use of acetone had to be increased to 25 min to achieve an adequate particle yield. The insolubility of PEI in acetone, the longer necessary release time and the significant increase of patch thickness indicates an adhesion failure between stamp and ink film. The surrounding non-solvent must lead to a higher adhesion force between the particle and the ink surface in comparison to the cohesion force inside the polymeric film. As a consequence of this effect the particles attempt to rupture the ink layer whereby a longer release time is necessary.

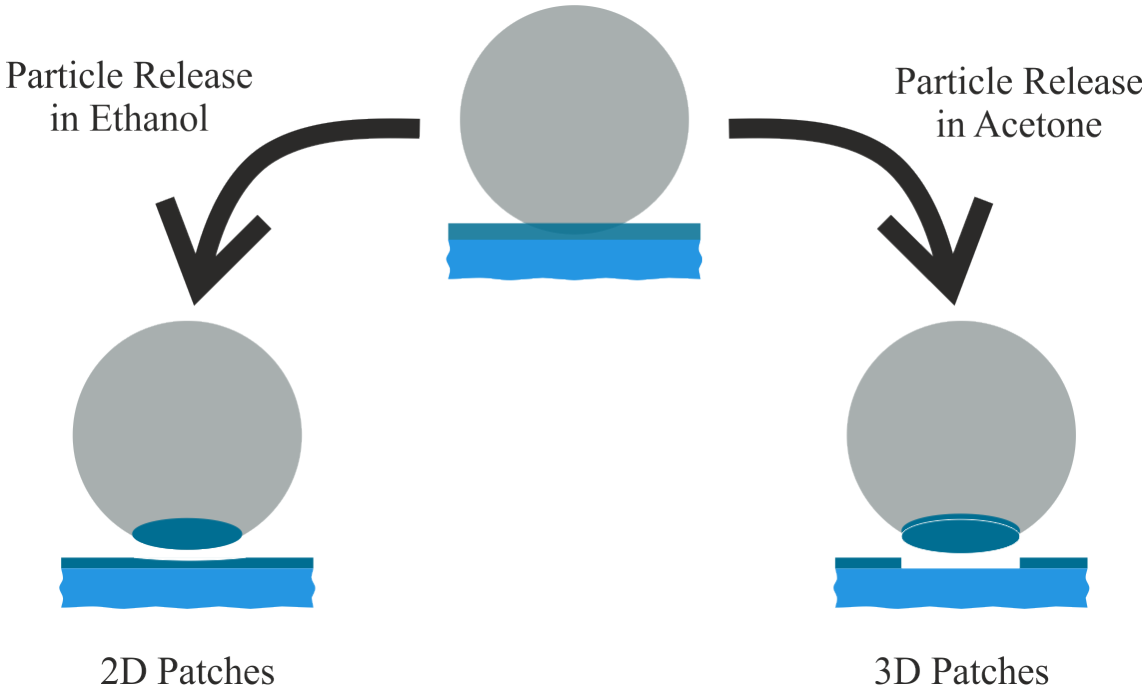

Figure 2.14 Illustration showing the switch from 2D surface modification to 3D structure printing by changing the release solvent: Ethanol induces a cohesion fracture inside the PEI layer whereby acetone causes an adhesion failure between the ink and the stamp.

Further evidence were gathered to support this explanation by using ellipsometric measurements (compare section 8.2.7). Very thin PEI films (below 30 nm) were prepared on silica wafers and subsequently enclosed with different solvent reservoirs into a ellipsometry vapour chamber while continuously measuring the film thickness. Fig. 2.15 shows the normalized swelling behaviour of PEI films in an ethanol and acetone atmosphere. The PEI film exposed to the ethanol vapour showed almost immediate and continuous swelling. After 35 min the film thickness reached a plateau at a swelling degree of 200 %. This value

was stable for approximately 8 min until dewetting of polymer film occurred. In contrast, the film exposed to the acetone vapour did not show any transition for 45 min. Although conditions differentiate from the complete submersion of a stamp into the respective solvent during ultrasonication, it does shows very well the stability of PEI in acetone.

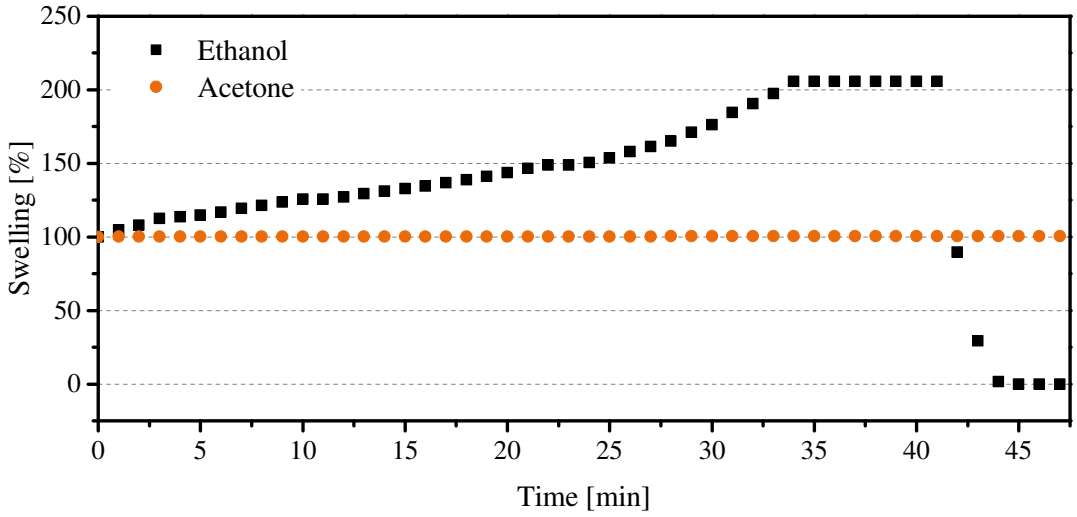

Figure 2.15 Diagram showing swelling experiments of PEI films measured by ellipsometry. Experiment with ethanol shows constant swelling and finally dewetting of the PEI film after 40 min. No changes are visible for the acetone measurement.

These results clearly state a new opportunity for precise surface modification using spherical particles. By changing the solvent during particle release it is possible to significantly change the patch geometry from two-dimensional modification (2D) to three-dimensional structure printing (3D). The range of these adjustments are presented in detail in chapter 3 while additional capabilities of this new concept will follow in the next section.

2.9 Incorporation of Nano Additives

The particle release process using acetone as release solvent enables the significant increase of the patch thickness. This switch from 2D modification to 3D structure printing gives a new unexploited volume inside the patches, which can be used for further incorporation of physical properties and functionalities. Fig. 2.16 shows the expanded μCP procedure, introducing the incorporation of nano additives into the accessible volume without alteration of the surface properties. This process is implemented by blending small amounts of nano additives (e.g. quantum dots) into the ink solution prior to spin coating (compare section 8.2.3). By selecting a suitable surface charge, compatible with the used polyelectrolyte, the nano additives disperse inside the ink film. After printing, the nano additives

are enclosed in the ink film and remain so while particles are released in acetone, because PEI will not dissolve. The additives are entrapped in the surrounding polymer matrix without chemically altering the patch surface, giving the opportunity for additional physical properties.

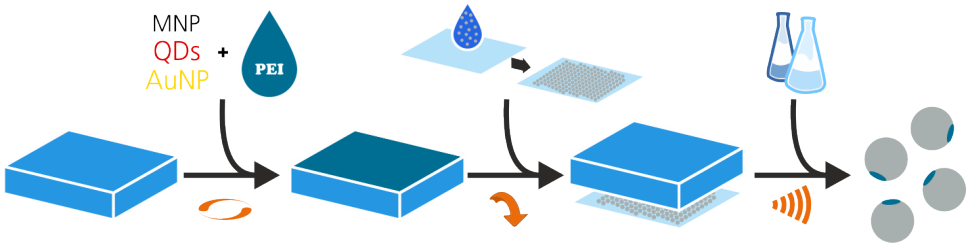

Figure 2.16 Illustration of the microcontact printing process with the incorporation of nano additives into the polyelectrolyte film during spin coating.

The microscope images in Fig. 2.17 show possible applications for this procedure. Fig. 2.17(a) displays particles with fluorescent labelling by introducing quantum dots into the patches. With this technique it is feasible to determine the position of the patches while retaining the functional groups on the surface for further modification (compare section 4.3). Furthermore no leakage of fluorescent quantum dots was observed during these experiments, even while non labelled particles were present. The negatively charged quantum dots could otherwise easily attached to other positively charged PEI patches. The introduction of superparamagnetic nanoparticles is shown in Fig. 2.17(b). With this system, the possibility of particle alignment inside an magnetic field was examined (compare section 4.2). Additionally, the incorporation of gold nanoparticles inside the patches was investigated and is shown in Fig. 2.17(c). Due to the greatly differing refractive index of gold[186,187] in comparison to the surrounding materials, the patch become visible even on a transmitting light microscope image.[188,189]

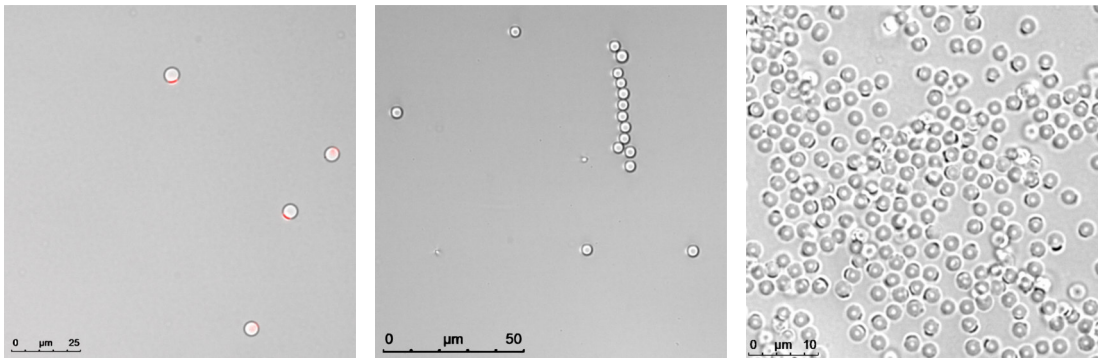

(a) Fluorescent Quantum Dots (b) Superparamagnetic NP (c) Gold Nanoparticle

Figure 2.17 Microscope images show patched silica particles with incorporated nano additives.

2.10 Key Parameters and Characterization

For the comparison of different printing scenarios (e.g. particle sizes, ink concentrations) two key parameters were selected. These key figure were measured by suitable analytical methods and are essential for the discussions in the following chapter. These characterization methods will be shortly introduced.

The first parameter was the patch diameter d. This key figure was measured by labelling of the achieved patches (see section 8.2.5) and recording of an adequate amount of fluorescence microscope images. Afterwards, the patch diameter was obtained using a microscope imaging software, measuring the fluorescence signal of the patches, and a mean value with standard deviation was calculated for every printing system (compare section 8.4.1). The microscope images in Fig. 2.18 give an impression of the measured distance for different printing samples and particle orientation, which is highlighted using a striped line.

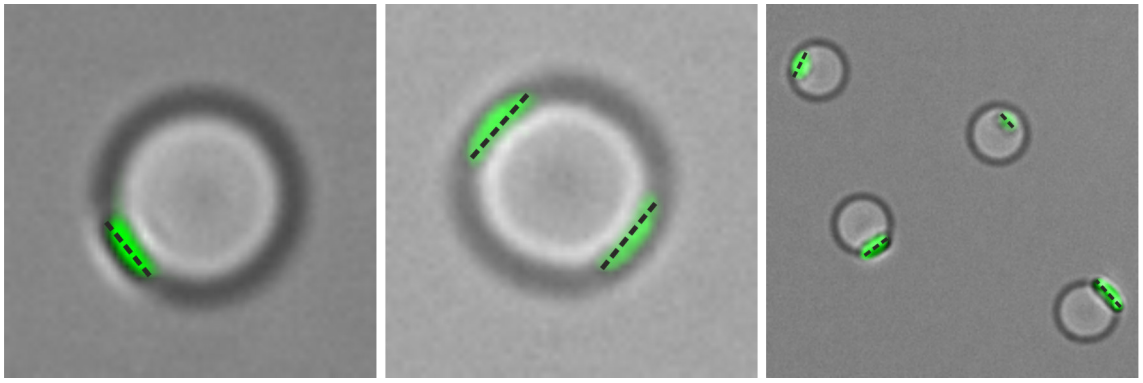

Figure 2.18 The illustrated fluorescence microscope images show different patched particles labelled with FITC. The striped black line was inserted to give an impression of the measured distance for the calculation of the patch diameter d.

The second key parameter was the patch thickness t. As described in section 2.8 it is possible to significantly increase the patch geometry by switching the release solvent. Therefore it is necessary to measure the patch thickness for different particles sizes and ink concentrations. Measuring the thickness using the fluorescence signal was not feasible as the image resolution was not sufficient for this approach. SEM imaging gives a clear perception of the patch geometry, but provides only a small number of data points. Therefore an indirect method was used, which is illustrated in Fig. 2.19.

Using acetone as release solvent leads to a thick patch structure, which is indirectly quantifiable from the PDMS stamps after the particle release. Acetone does not dissolve

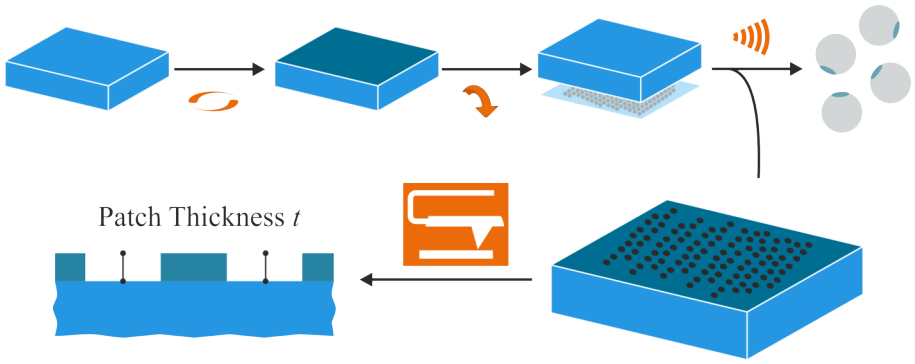

Figure 2.19 Schematic diagram shows the AFM characterization of the PDMS stamp after particle release for the indirect parameter determination of the patch thickness t.

the polyelectrolyte layer and the remaining ink structure remains intact. Therefore the thickness of the removed patch is measurable using the height channel of atomic force microscopy. This approach was only feasible for samples released in acetone. The amount of removed ink during the use of ethanol seems to be not significant enough to be detectable with AFM. Another explanation is represented by the ink layer's low solubility in ethanol, which is able to compensate for removed ink by diffusion. AFM images for comparison of the stamp surface after ethanol and acetone release are displayed in Fig. 2.20. The patch diameter was not measured via AFM, because the ink layer showed very distinct cracks in the surface after particle release. Possible an effect of slightly swelling PDMS which would rupture the film. Due to this effect the remaining holes are often deformed and a spherical geometry is not found.

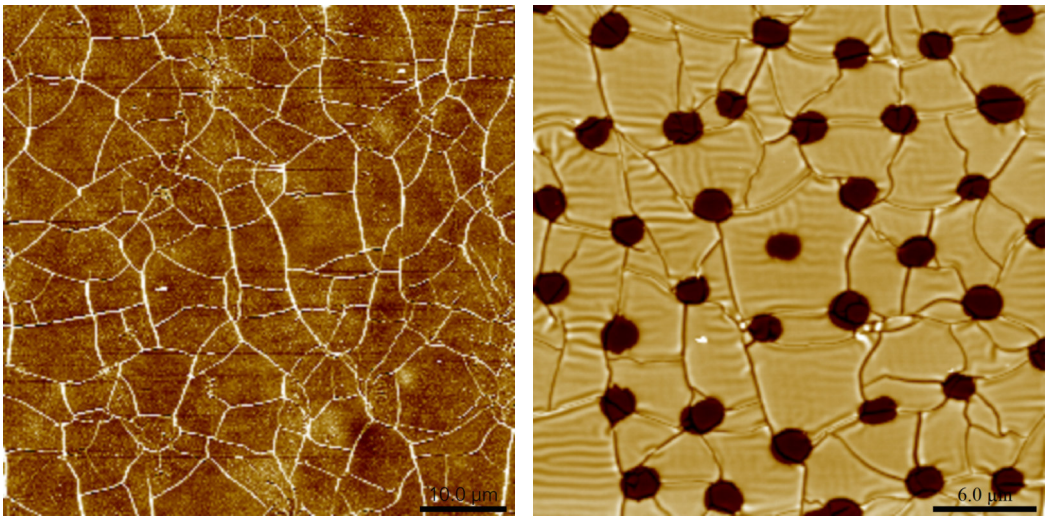

(a) Ethanol - Height Scale 17 nm (b) Acetone - Height Scale 170 nm

Figure 2.20 AFM images of PDMS stamps loaded with 3 wt% PEI after the particle release in different solvents. The use of acetone forms distinct holes inside the polyelectrolyte layer as it is transferred onto the particle surface. This is not detectable during the use of ethanol as the releasing solvent.

CHAPTER 3

Investigation on the Patch Geometry of Patchy Silica Particles

The previous chapter introduced the essential components and materials used during printing of silica spheres for the synthesis of anisotropic particles. Additionally it described new findings for the sophisticated patch geometry switch from two-dimensional modification to three-dimensional structure printing. These findings, based upon the application of polyelectrolyte inks, enable the use of an additional volume for further physical functionality by the incorporation of nano additives. The following chapter will exclusively discuss the achieved range of this approach including the patch diameter, thickness and yield for a broad range of particle sizes. The reverse use of charges is investigated by adjustment of particle surface chemistry and a suitable anionic polyelectrolyte. Finally, the increase of patch number by sandwich printing and structured stamping material is presented. These results clearly characterise the adaptable utilization of this microcontact printing toolbox.

3.1 Single Patched Particles

Initial printing experiments were conducted to produce anisotropic particles with only one patch (SSP) or in other words divalent particles.[81] For this research, unmodified and thus negatively charged silica spheres with sizes of 5 µm, 4 µm, 2 µm and 1 µm where printed using branched PEI with high molecular weight at different loading concentrations (1/2/3/4 wt%). This section will discuss the achieved results for all particle sizes, starting with the largest one, and the applicable ink concentrations. Initially, the patch geometry produced by release in ethanol and acetone will be compared using the 5 µm particles. Subsequent experiments for smaller spheres were performed using only acetone as release solvent in order to investigate the structure of these new 3D patches. All printing systems are characterized by a fluorescence microscope image of the FITC labelled single patched

particles, a SEM image visualizing the patch geometry in detail for a small exemplary sample and a histogram showing the patch diameter distribution, along with the mean patch diameter d and its standard deviation.

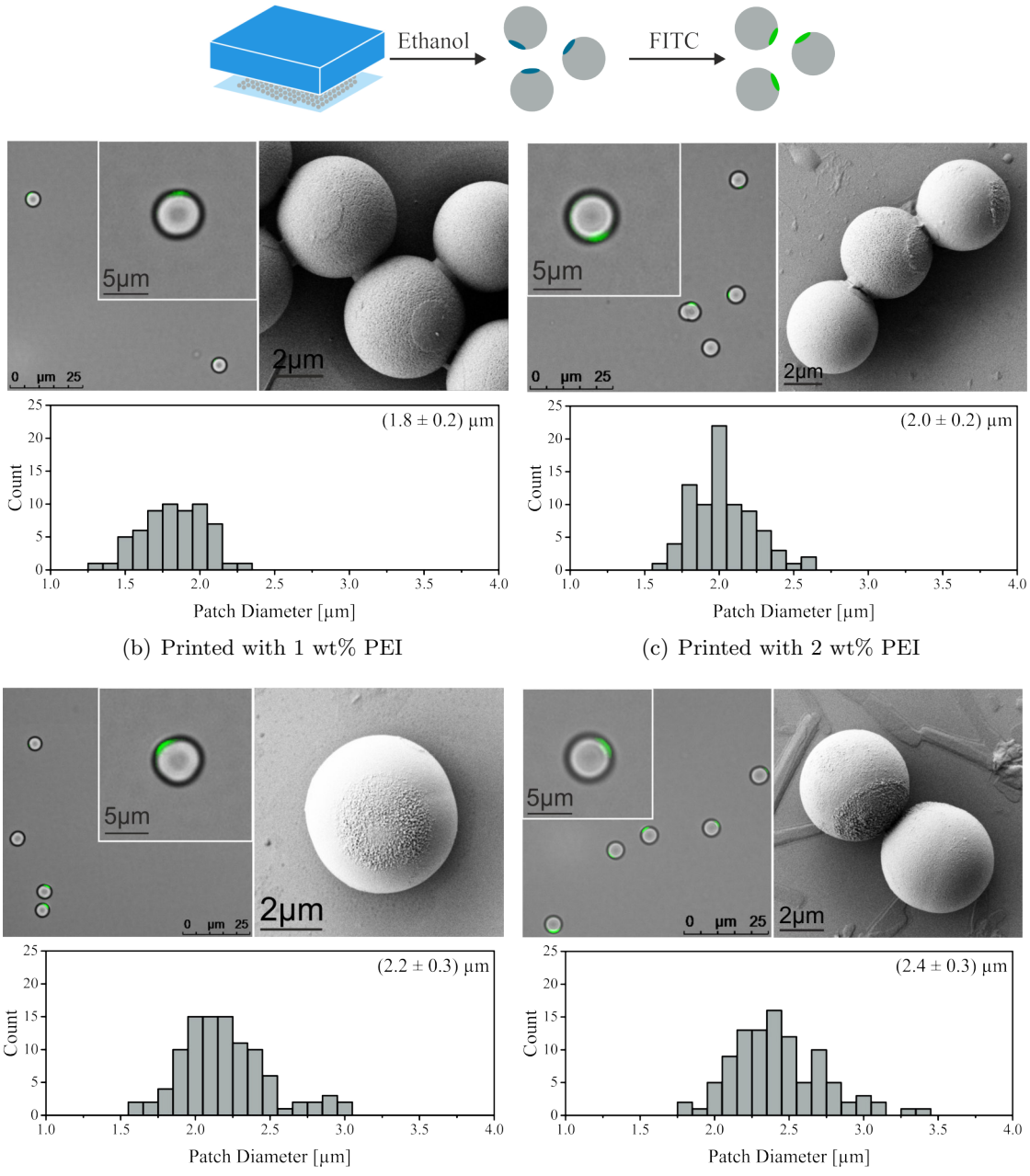

(b) Printed with 1 wt% PEI

(c) Printed with 2 wt% PEI

(d) Printed with 3 wt% PEI

(e) Printed with 4 wt% PEI

Figure 3.1 Summary of the results for 5 µm single patched particles printed with four different PEI concentrations and released in ethanol. Findings include a fluorescence microscope and SEM image, and the patch diameter distribution for all concentrations.

Fig. 3.1 displays the results for 5 µm silica particles printed with four PEI concentrations and released in ethanol for the production of 2D patches. The fluorescence signal on the microscope images is relatively weak due to the thin functionalization of the particle surface. However, the signal is still strong enough to be visible even as an overlay picture

on top of the light microscope image. An increase of patch diameter is detectable for increasing PEI concentrations. The same observation was made in the SEM images. A thin modification layer is visible, which increases in diameter with rising ink concentration. The increase of patch diameter with higher loading concentration was expected. Since the same printing force is applied to all samples, the only difference is the thickness of the polyelectrolyte film. A thicker ink layer results in a deeper embedment of the particle, which translates into a larger patch diameter. The distribution of patch diameter shows relatively broad but distinguishable results for the different ink loads. The diameter increases from (1.8 ± 0.2) µm to (2.4 ± 0.3) µm with a very slight trend for broader distributions at higher PEI concentrations, although this trend is almost non existing inside the standard deviation range. The ink surface seems relatively smooth for the 1 wt% sample, but becomes rougher for higher concentrations. The later would further confirm the theory of a cohesion fracture for the use of ethanol as release solvent (see Fig 2.14). As the ink layer slightly dissolve and the particle detaches from the stamp, bundles of polymer chains could protrude from the patch surface as a result. The 1 wt% PEI solution produces a film thickness of only 25 nm. It is possible that this thin film does not undergo a cohesion fracture, because the entanglement of high molecular weight PEI is too strong in this small-sized area. An additional indication for this assumption is the hydrodynamic radius of singular branched PEI chains with comparable molecular weight in solution, which is higher than the thickness of the ink film at this loading concentration.[190] Therefore a complete detachment of the film could take place and reveals a plain patch surface.

According to these results, comparable experiments for the synthesis of 3D SSP, by using acetone as release solvent, are displayed in Fig. 3.2. The general trend for the patch diameter is similar compared to the 2D patches. Increasing PEI concentrations translate into greater patch diameters. However, although the diameter for the 1 wt% sample remained the same with a value of (1.8 ± 0.2) µm the obtained results seem to indicate a stronger increase of diameter for patches released in acetone. The 4 wt% sample reaches the highest patch diameter with (2.6 ± 0.3) µm and is therefore 200 nm larger than the corresponding 2D patch. Fluorescence microscope images reveal a considerably improved contrast of the 3D patches, especially for the 3 and 4 wt% samples. That is even the case if particle orientation does not grant the best visibility of the patch. The reason for this effect, is not an strong increase of patch diameter, but foremost due to the significant

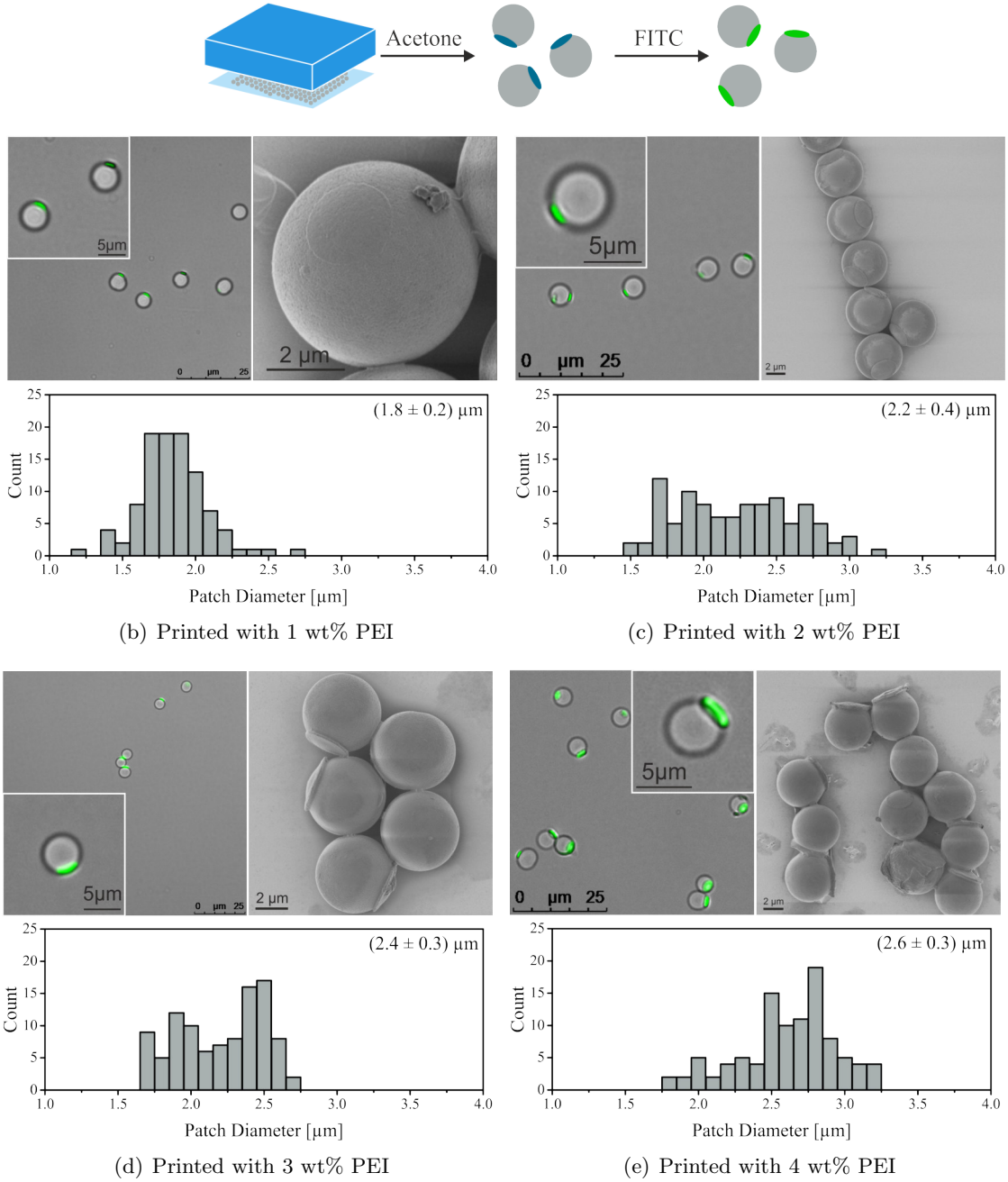

(b) Printed with 1 wt% PEI

(c) Printed with 2 wt% PEI

(d) Printed with 3 wt% PEI

(e) Printed with 4 wt% PEI

Figure 3.2 Summary of the results for 5 µm single patched printed with four different PEI concentrations and released in acetone. Findings include a fluorescence microscope and SEM image, and the patch diameter distribution for all concentrations.

change in patch thickness. The SEM images allow a detailed analysis of the change in patch geometry. This change begins rather unimpressive with the 1 wt% sample. It shows almost the same pictures as the particle released in ethanol; another indication for the previously discussed theory. Under these conditions the ink layer is too thin for a cohesion fracture and therefore no difference is visible for the patch geometry released in ethanol and acetone. But, starting from here the patch geometry turns almost into a coin-like shape for the 2 wt% and becomes even more pronounced for the 3 wt% sample. However, for both concentrations the patch geometry appears clean without protruding edges or residues. Increasing the PEI concentration to 4 wt% reveals exactly this behaviour. The coin-like structure turns even thicker, but the edges appear to become inaccurate. This effect could be an indication for an upper limit of ink concentration that is applicable, before particles tend to not detach during particle release. This observation will be discussed later again (see section 3.3.1). The patch thickness was calculated by measuring the dried PDMS stamps after particle release. Corresponding AFM images are displayed in the appendix section 9.2.1 and the results will be discussed later in comparison with all other particle sizes (see section 3.3.2). Again, this was only possible for the 3D patches, as no patch thickness was measurable for the particles released in ethanol.

The next adjusted parameter was the microsphere size and therefore 4 µm silica particles were used. The corresponding results are shown in Fig. 3.3. As already mentioned, particle release was conducted using only acetone and the applicable PEI loading was reduced to 3 wt%. Higher ink concentrations would not produce an adequate yield, as the particles would not detach from the loaded stamp. All priorly mentioned observations are also true for the smaller particle size. Patch diameter increases and the patch geometry becomes more protruded with higher ink concentrations. In comparison to the 5 µm particles, the patch diameter is larger in relation to the particle size. The patch diameter for the 5 µm sample printed with 1 wt% PEI reaches only 36 % of the particle size. The corresponding 4 µm sample shows 42 % of the particles size. The 3 wt% sample achieves for both particle sizes the same absolute value of 2.2 µm, but this translates again in 43 % and 54 % of the particle size, respectively. Although the patch diameter increases relatively for the smaller particle size, the standard deviation declines for these silica particles. As will be discussed later, this observation is not a result of the actual printing process, but the influence of the naturally occurring particle size distribution (see section 5.1). SEM

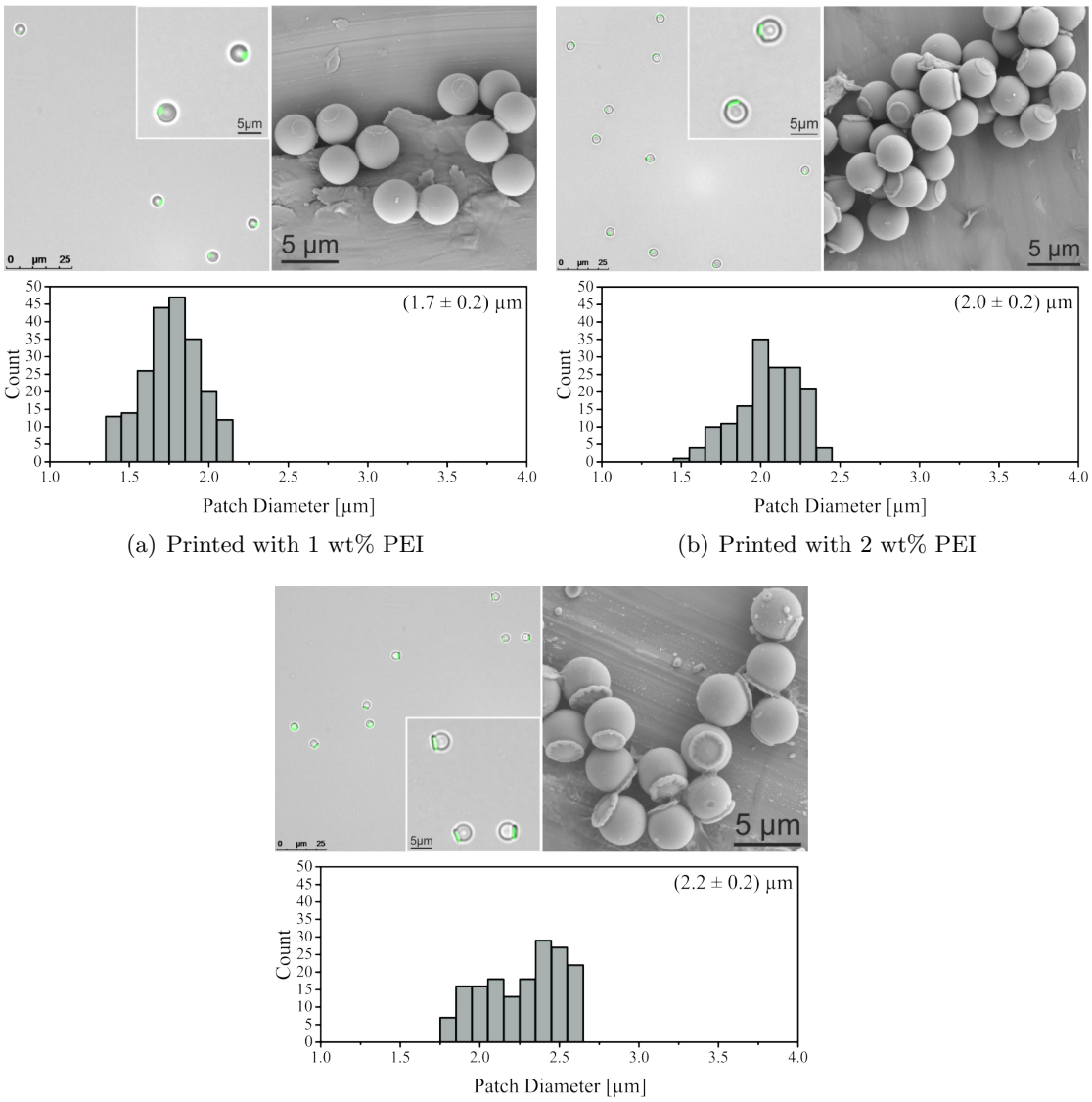

(a) Printed with 1 wt% PEI

(b) Printed with 2 wt% PEI

(c) Printed with 3 wt% PEI

Figure 3.3 Summary of the results for 4 µm single patched particles printed with three different PEI concentrations and released in acetone. Findings include a fluorescence microscope and SEM image, and the patch diameter distribution for all concentrations.

images display an almost unchanged geometry for the 1 and 2 wt% sample, but the 3 wt% PEI loading shows an unusual edge effect of the patches. Due to its relative large patch size in comparison to the sphere size, it is possible that the particle curvature is too large and therefore it is not possible for the edges of the patch to remain attached to the particle surface. However, this was not observed for other particle sizes. Another possibility could be squeezing of polyelectrolyte from below the particle as an effect of increased local pressure, forming a donut-like structure. But as calculation showed, this effect should not be the case for a constant printing force while reducing the particle size (compare section 5.3). Additionally, other particle sizes did not show this behaviour.

A final suggestion could be a different surface composition of the silica particles. Since the used microspheres originate from different suppliers, it could be possible that some synthesis routes include stabilizer which could interfere with the electrostatic interaction, although zeta potential measurement did not show any difference in surface charge. It has to be mentioned that non of these hypothesises could be proven sufficiently during the course of this research.

The next smaller silica particles with a size of 2 µm were only printed with two different PEI concentrations and the results are displayed in Fig. 3.4. In contrast to other particle sizes, microscope images show only the fluorescence channel of the measurement. In this example, particle movement was too pronounced to achieve an aligned overlay picture and an overview image showing a large amount of SPP without patch-less particles was preferred. The 1 wt% sample shows again a similar patch geometry in comparison to larger particles. The mean patch diameter of (1.13 ± 0.15) µm translates into 53 % in relation to the particle size and rises to 57 % for the 2 wt% sample with a diameter of (1.20 ± 0.15) µm. This finding follows the trend for decreasing particle sizes. SEM images show a relatively smooth patch surface for the 1 wt% sample and a noticeable roughness increase for the 2 wt% sample, which is also comparable to previous observations (also compare section 3.3.1). The patch diameter distribution does not exhibit a significant difference between the herein used ink concentrations.

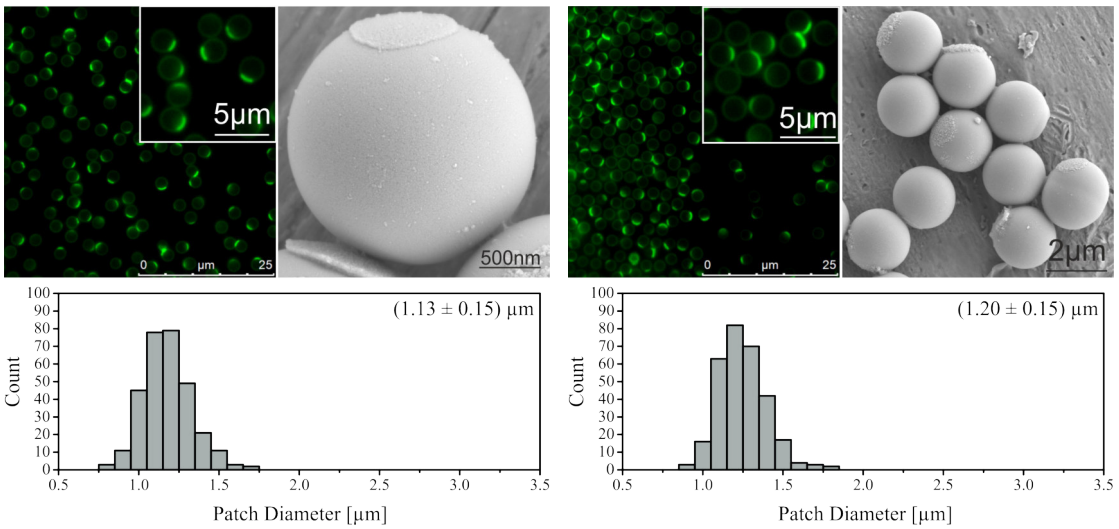

(a) Printed with 1 wt% PEI

(b) Printed with 2 wt% PEI

Figure 3.4 Summary of the results for 2 µm single patched particles printed with two different PEI concentrations and released in acetone. Findings include a fluorescence microscope and SEM image, and the patch diameter distribution for all concentrations.

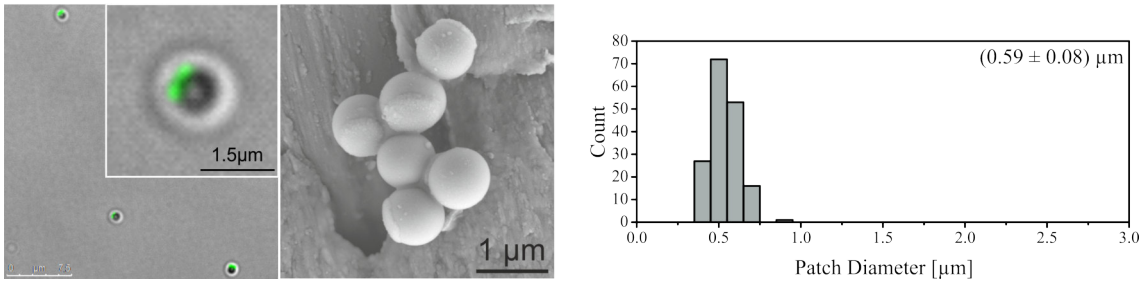

(a) Printed with 1 wt% PEI

Figure 3.5 Summary the results for 1 µm single patched particles printed with 1 wt% PEI and released in acetone. Findings include a fluorescence microscope and SEM image, and the patch diameter distribution for all concentrations.

Finally, 1 µm silica spheres were used and printed with a ink concentration of 1 wt%. The results are displayed in Fig. 3.5. Even at this particle size the printing process was successful. The SEM image shows a relatively smooth surface of the patch, which seem to obtain a quite large diameter. Fluorescence microscope image tend to be even more difficult to achieve for these particle sizes as Brownian motion becomes more of an issue. The diameter was calculated to be (0.59 ± 0.08) µm and consequently reaches a value of 58 % in relation to the particle size, being the largest value achieved for SPP and therefore confirms this trend for the used particle size range.

These results show the successful synthesis of 2D and 3D SPP with controllable patch diameter, which is influenced by the ink concentration and the suitable solvent during particle release. Four very specific polylectrolyte concentrations have been used in the course of this research. However, the full benefit of this approach becomes apparent as one can tune the concentration very finely and therefore the height of the deposited layer on the PDMS stamp. Broad standard deviations for the discussed results seem to indicate the contrary, but in the case for perfectly monodisperse particles, the error margin would decrease dramatically as will be explained later (compare section 5.1), which determines the real precision of this µCP process.

3.1.1 Inverse Printing for Positively Charged Particles

For further investigation of the potential and versatility of this approach, differently charged polyelectrolytes should be used. For this experiment, the silica particle surface had to be functionalized with positively charged groups by using a suitable alkoxysilane (compare section 2.4). In this case a common amine modification using APTES was successfully performed (see Fig. 2.8). As a potential ink the anionic polyacrylic acid (PAA) was

chosen as acetone is also a non-solvent for this polymer and therefore should follow the same mechanism as PEI printed particles. Labelling was performed by positively charged quantum dots, which were introduced directly into the PAA solution prior to spin coating onto the PDMS stamp. Positively charged quantum dots were obtained by a ligand exchange reaction (see section 8.2.3) to ensure uniform distribution of the nanoparticles inside the ink.

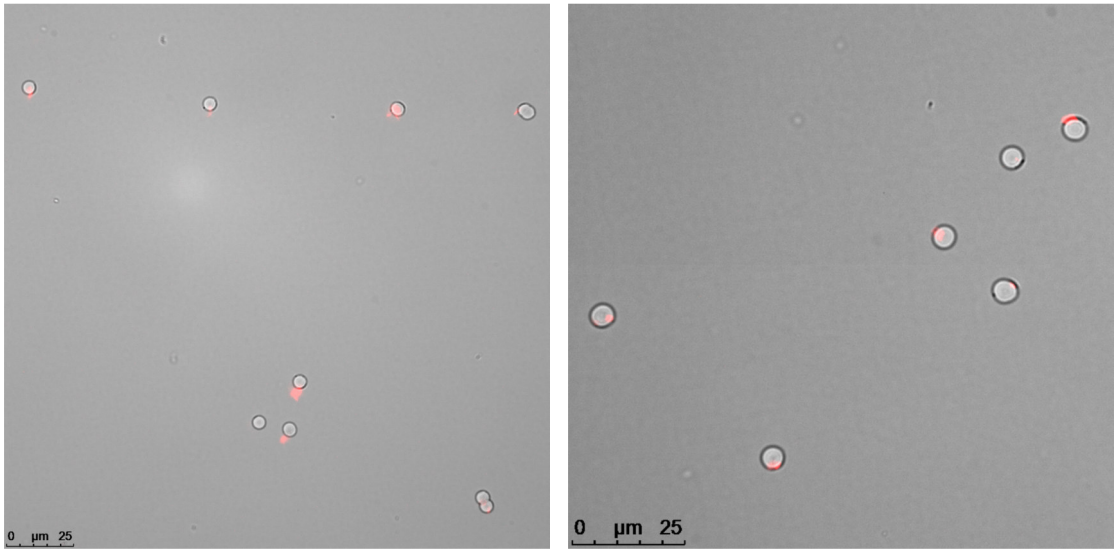

Figure 3.6 Fluorescence microscope images of amine modified silica particles printed with 3 wt% PAA. Patches were labelled with incorporated quantum dots. The strong mismatch between fluorescence and light microscope images derives from fast particle movement.

The synthesis of 3D SPP was conducted using a stamp loaded with 3 wt% of labelled PAA and 5 µm silica spheres. Fluorescence microscope images of the released particles are shown in Fig. 3.6. The successful printing of patches is visible via the transferred fluorescence signal of the embedded quantum dots on the particle surface. However, the geometry of the patches is not as distinct as previous SPP printed with PEI and also the achieved yield was significantly lower. More unmodified particles without fluorescent signal were detected. Fluorescence images seem to indicate that the patch thickness is clearly decreased in comparison with the corresponding PEI sample (compare Fig. 3.2) This observation is also confirmed by SEM images displayed in Fig. 3.7. Patches show an nonspherical and thin geometry, which significantly differs from PEI patches. These findings are explainable by several points: The PAA had a very low molecular weight compared to the used PEI ($8\,\mathrm{kg\,mol^{-1}}$ vs $600\,\mathrm{kg\,mol^{-1}}$). Therefore the patch could dissolve more rapidly in the surrounding ethanol, which is always used for washing and imaging after particle release. Nevertheless, it is a clear confirmation of the high stability of PEI patches

during the washing steps. Secondly, the PAA possesses a linear structure in contrast to the former used branched PEI. The previously mentioned increased entanglement of the branched structure is apparently another important point for the creation of 3D patches. Furthermore the isoelectric point of the amine modified particles is located at a pH of 6.3, as zeta potential measurements have shown. This means that the surface is positively charged below this pH value. For higher pH values the surface is still negatively charged or at least neutral. As the printing process shows positive results, the functionalization of particles was sufficient. Still, the concentration of accessible positive surface groups will be lower in comparison to negatively charged groups on unmodified silica spheres. This will influence the stability of the electrostatic bonding and would explain the reduced yield. With further optimization of the process including high molecular weight ink, further increase of the positive surface charge and possible screening of other release solvents a functional change to anionic polyelectrolytes is possible.

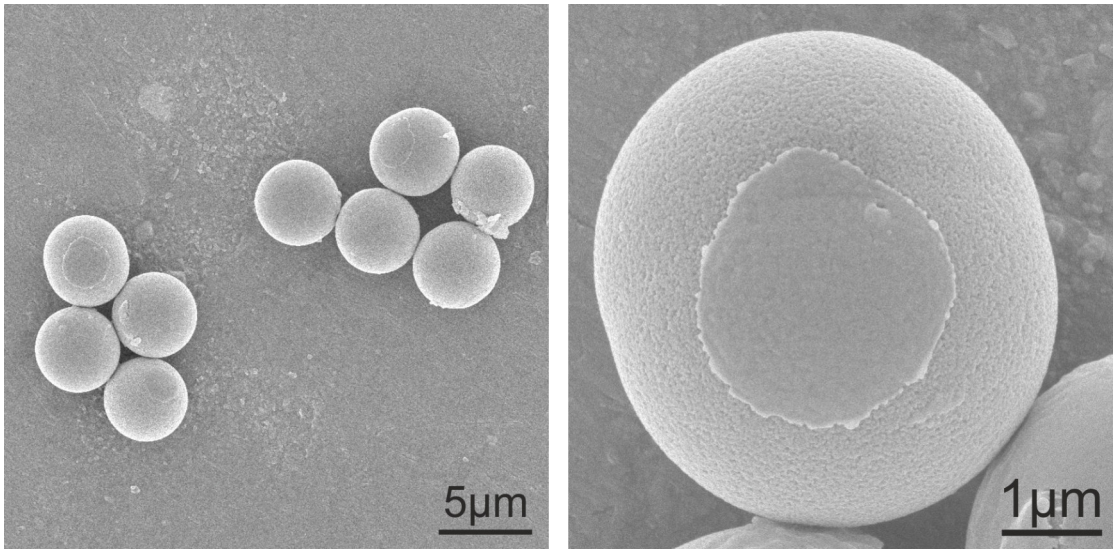

Figure 3.7 SEM images of amine modified silica particles printed with polyacrylic acid.

3.2 Double Patched Particles

The next challenge for the synthesis of anisotropic particles was to increase the number of applied patches. In the microcontact printing community it is a common approach to use two loaded stamps at once for the production of trivalent particles with two patches in a 180° angle. This approach is often called "sandwich" printing.[81] Typically, it is a simple extension of the one-sided printing and only requires the repetition of printing steps with no further adjustment. However, these results are generally obtained by using molecular inks, which would bind covalently to the particle surface. Hereby, the essential step is the chemical reaction on the surface.[65] The system presented in this research uses the electrostatic interaction between ink and particle surface. As clearly shown in the previous chapter the essential and most important step during the production of 3D patches is the solvent assisted release mechanism (compare section 2.8). During this step the geometry of the patch is determined by the choice of solvent. Without this step the particles would detach without any surface modification, for example by removal with an adhesive strip. This effect became obvious during first experiments for the production of double patched particles (DPP). Initially the same sandwich printing procedure was conducted. Particles adhered to the first PDMS stamp and a second loaded stamp was pressed against it to print another patch. These experiments lead to particles with one patch after particle release. The functionalization of particle surface would only occur on the sphere side, which is embedded in the ink layer. Additional experiments using the solvent assisted release while both PDMS stamps were still joined together only produced SPP with no distinct patches and a high amount of ink residues in the sample.

However, it was possible to introduce a simple air plasma etching process in between two consecutive printing steps to successfully produce 3D DPP with high quality and good yield.[141] The process is illustrated in Fig. 3.8. Due to the etching step, the polyelectrolyte layer is carefully removed, which leads to a reduced contribution of the lateral component of the adhesion force inside the ink film during the particle lift-off with the second stamp. This slight removal of the ink enables the rupture of the polyelectrolyte layer and the transfer onto the particle surface. All particles transferred onto the second stamp could than be removed easily using the normal particle release route. Following this procedure a feasible production of symmetrical patches is finally possible. The influence of the

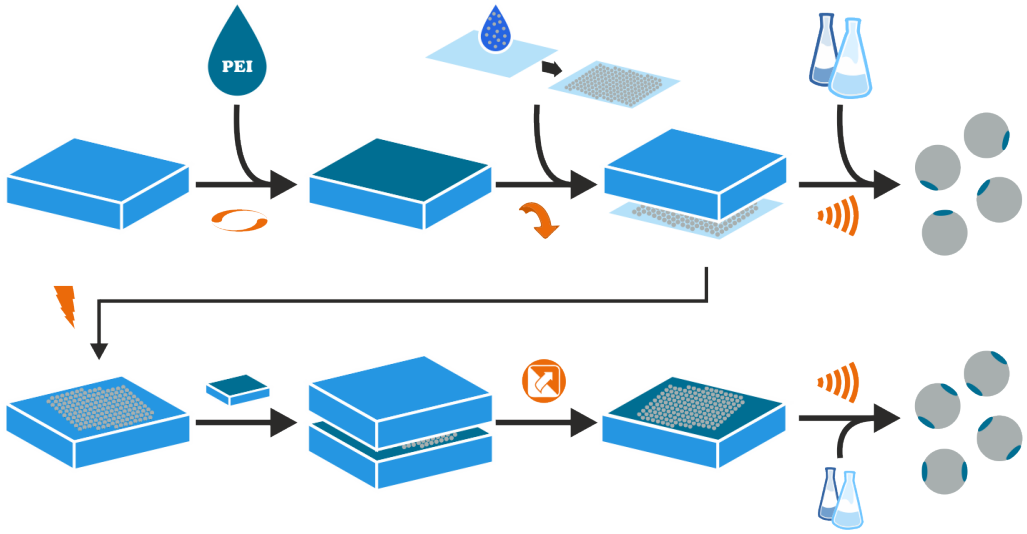

Figure 3.8 Illustration of the microcontact printing process for the synthesis of single and double patched particles. The later introduces an additional intermediate step consisting of air plasma etching, which is necessary for trivalent particles.

air plasma etching on the geometry of the first patch will be discussed in detail in the next section 3.2.1. In the following the results for all 3D DPP including applicable ink concentrations and particles sizes are discussed.

The fluorescence microscope images of 5 µm silica spheres show clearly the successful printing of DPP with very distinct patches on both sides of the particles (see Fig 3.9). From these images it is not possible to determine a difference between two patches. Also SEM images show a symmetrical patch geometry for all ink concentrations except the 4 wt%. This sample shows a significant difference between two patches. This behaviour is also observable for the patch diameter as it increases with thicker PEI films, but decreases again for the last sample. The reason for this behaviour, is an unusual broadening of the patch diameter distribution for the 4 wt% sample, which would suggest that two very distinct patch geometries are formed for this parameter. This effect will be discussed in more detail in section 3.3.1. Corresponding SEM images indicate that in comparison to 5 µm SPP, the patch thickness is decreased, which will be reviewed later in section 3.3.2.

Decreasing the particle size to 4 µm gives a similar observation for the patch geometry. Fig. 3.10 shows the achieved results for the three different ink concentrations. Again, the patch quality shown on the microscope pictures is very good, patch thickness decreases in comparison to the SPP sample and the highest PEI film produces a very broad patch size distribution. As for the former sphere size that indicates the production of highly asymmetrical patches on the particle surface, which can also be observed in Fig. 3.10(c).

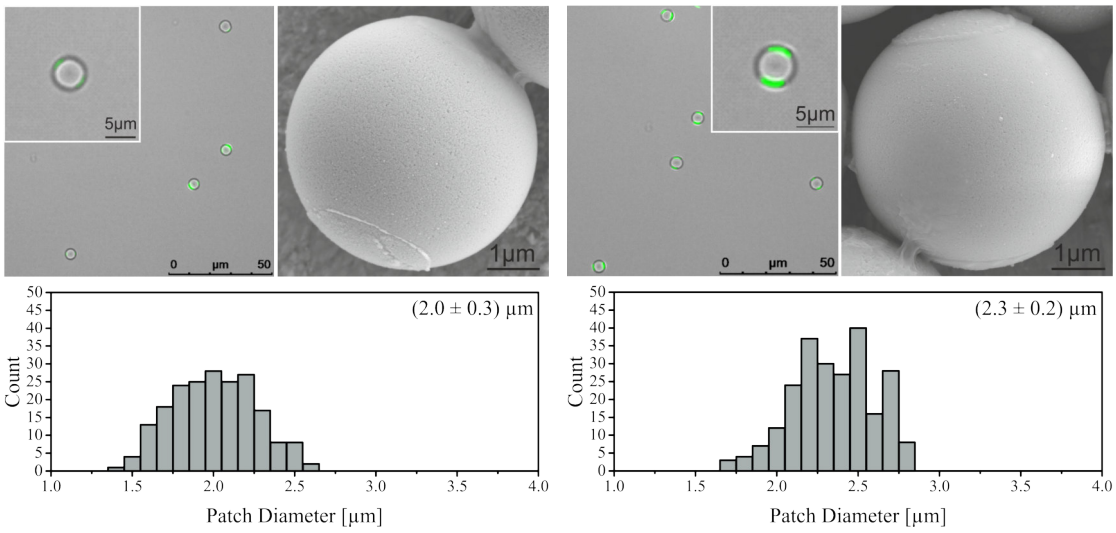

(a) Printed with 1 wt% PEI

(b) Printed with 2 wt% PEI

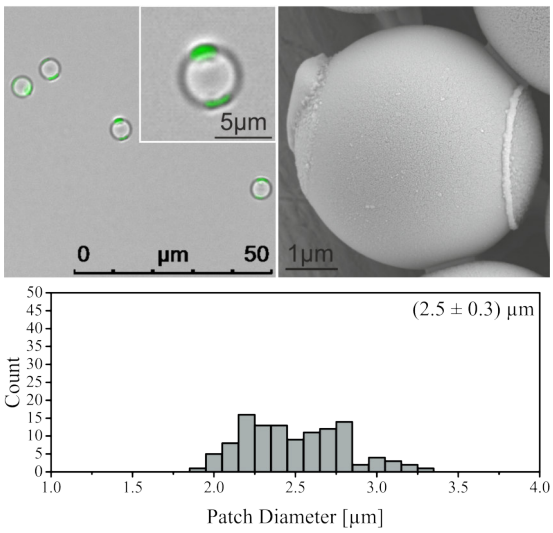

(c) Printed with 3 wt% PEI

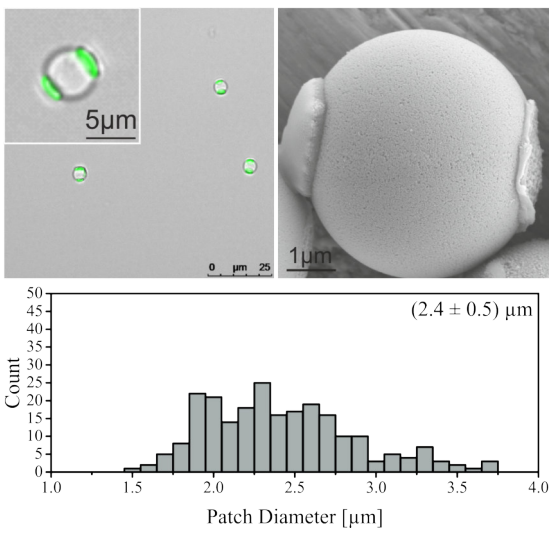

(d) Printed with 4 wt% PEI

Figure 3.9 This figure summarizes the results for 5 µm double patched particles printed with four different PEI concentrations and released in acetone. Findings include a typical fluorescence microscope and SEM image and the patch diameter distribution for all concentrations.

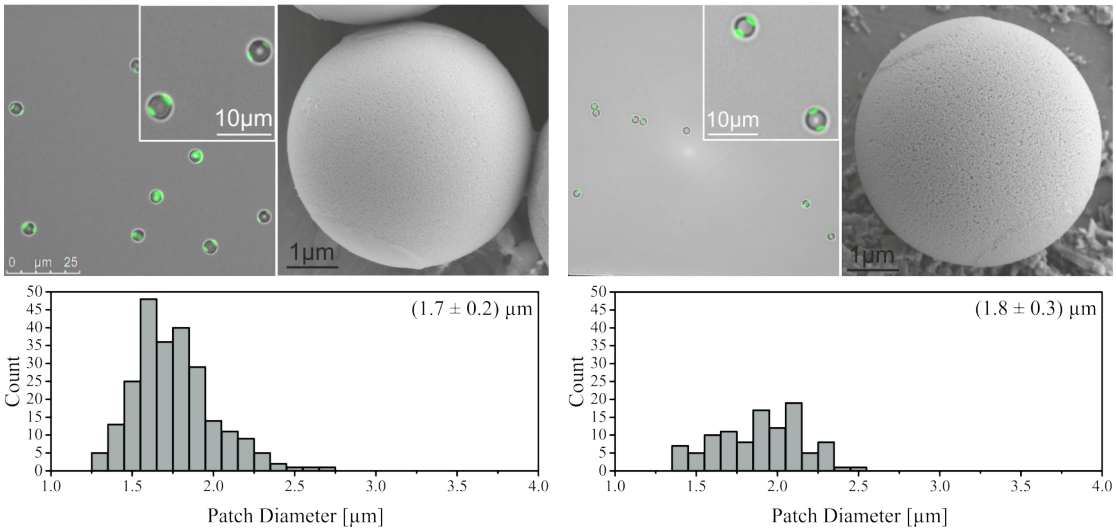

(a) Printed with 1 wt% PEI

(b) Printed with 2 wt% PEI

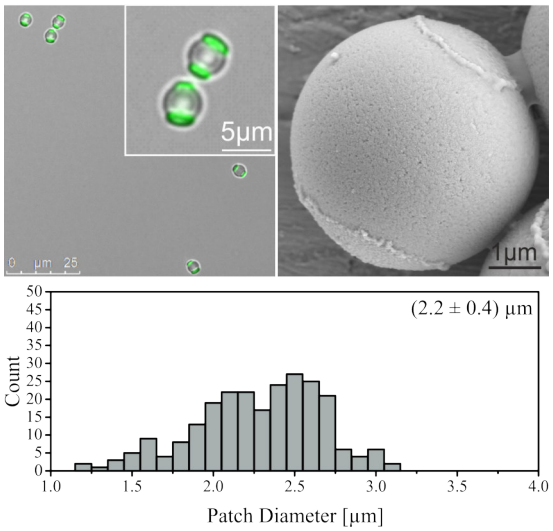

(c) Printed with 3 wt% PEI

Figure 3.10 This figure summarizes the results for 4 µm double patched particles printed with three different PEI concentrations and released in acetone. Findings include a typical fluorescence microscope and SEM image and the patch diameter distribution for all concentrations.

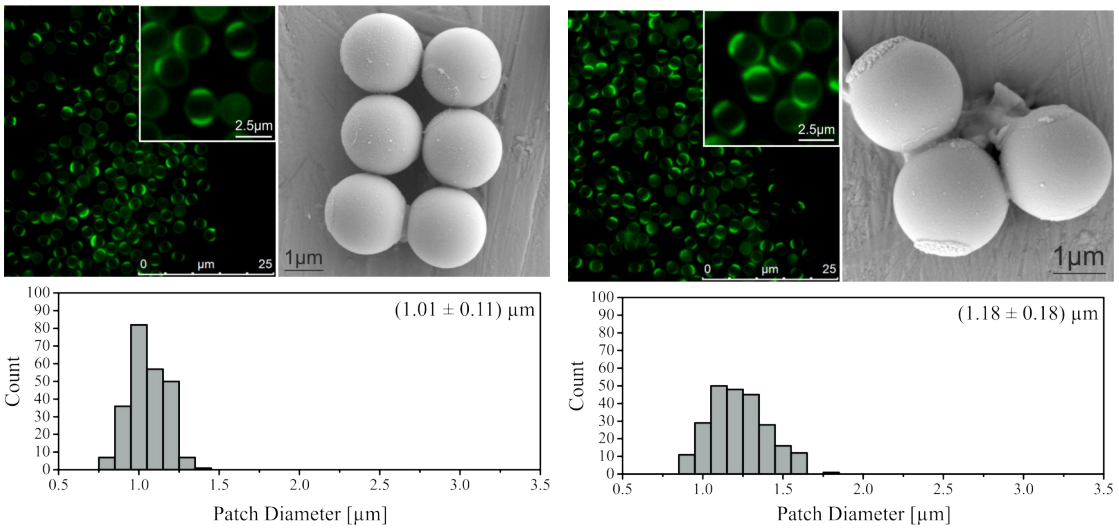

(a) Printed with 1 wt% PEI (b) Printed with 2 wt% PEI

Figure 3.11 This figure summarizes the results for 2 µm double patched particles printed with two different PEI concentrations and released in acetone. Findings include a typical fluorescence microscope and SEM image and the patch diameter distribution for all concentrations.

The microscope images of 2 µm silica particles revealed a good yield of DPP particles with very high quality and a fine patch diameter distribution (see Fig. 3.11). At least for the 1 wt% sample the same observations are true for the patched particles depicted in the SEM images. The highest applicable ink concentration of 2 wt% PEI on the other hand shows the same asymmetrical patch geometry visible for all other particle sizes during the production of DPP. The SEM image in Fig. 3.11(b) gives the best insight into this problem. One particle patch is very thin and possesses a smooth surface while the other side shows a protruding and rough patch.

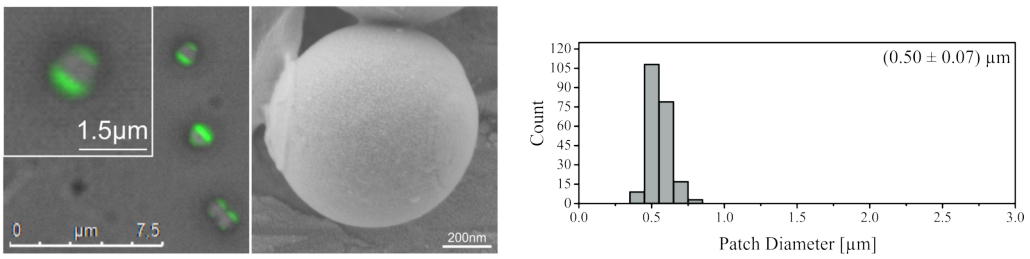

(a) Printed with 1 wt% PEI

Figure 3.12 This figure summarizes the results for 1 µm double patched particles printed with PEI and released in acetone. Findings include a typical fluorescence microscope and SEM image and the patch diameter distribution for all concentrations.

This printing method was successfully transferred on the smallest used silica particles with a size of 1 µm as it is shown in Fig. 3.12. Fluorescence microscope images also indicate a more asymmetrical patch geometry for this particle size. However, as the SEM images

point to a higher symmetry, the varying appearances of the patches are most likely due to different angles in relation to the optical plane. For the given parameters it was therefore possible to create symmetrical 3D patches on particles in this size range.

In summary, these results show how a fast and convenient intermediate step consisting of air plasma etching is capable of initializing a successful sandwich printing for the production of trivalent particles, while using polyelectrolyte inks. Also, as displayed in Fig. 3.13, it was possible to use differently labelled polyelectrolytes (FITC & quantum dots) for distinct patches on the particle surface. Apparently the thickness of patches is reduced in comparison to SPP, which will be discussed in detail in section 3.3.2. Furthermore, the highest applicable ink concentration for particle with a size of 5 µm, 4 µm and 2 µm shows a unusual broadening of the patch diameter distribution, which is the result of highly asymmetrical patches on the particle surface. In section 3.3.1 this behaviour will be further investigated by comparing different patch diameters on the same particle.

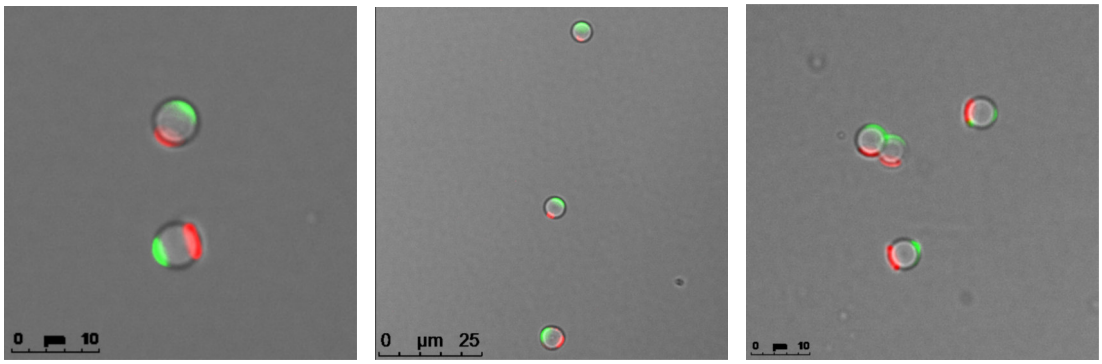

Figure 3.13 Fluorescence microscope images show double patched particles with distinctly labelled patches (FITC & quantum dots).

3.2.1 Influence of Intermediate Plasma Etching Step on Patch Geometry

During the last section, an intermediate air plasma etching step was introduced to the µCP process. This step enabled the production of double patched particles by reducing the lateral adhesion forces inside the polyelectrolyte layer or even by the complete removal of the surrounding PEI film. The effect of this process is illustrated in Fig. 3.14. However, research of the achieved patches revealed asymmetrical patch geometries for higher ink concentrations, which should be prevented during the process if it is possible. Due to this observation further investigations were conducted determining the influence of air plasma etching on the patch geometry of the first printed side. For this aim two different experiments were constructed.

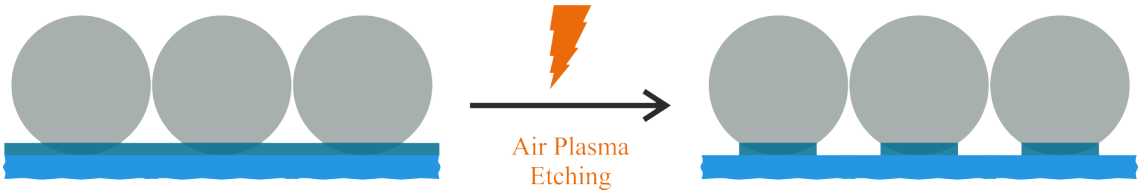

Figure 3.14 The scheme shows the effect of the air plasma treatment during the µCP process.

For the first experiment several square silicon wafer pieces with a size of 1 x 1 cm^2 were spin coated with 60 µL of the same 4 wt% PEI solution to obtain films with a similar thickness. Subsequently, the samples were exposed to air plasma treatment under the same conditions (100 W, 0.2 mbar) but increasing process time (10 s - 90 s). Afterwards the PEI film was scratched with a syringe cannula and height measurements were conducted at two different locations using AFM. The mean height values are plotted against the plasma etching time in Fig. 3.15. To calculate an etching speed v_e of the PEI film a linear fit was used. Although the fit does not achieve a high quality, a clear trend is visible. The etching speed extracted from this plot was $(1.0 \pm 0.1)\,nm\,s^{-1}$. This value confirms the actual etching effect of PEI during the process and gives a good estimation of the etching speed of uncovered PEI for the given conditions.

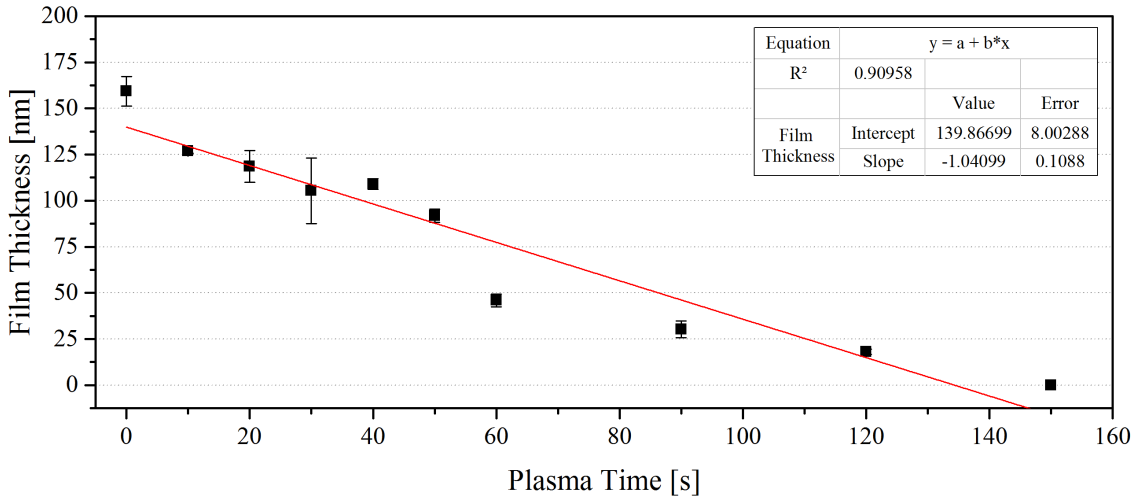

Figure 3.15 The diagram shows the AFM height measurements of PEI films exposed to air plasma with increasing process time. Every measurement was conducted at two different locations on the film surface to generate error bars. A linear fit was used to calculate the etching speed v_e of PEI from the slope.

The second experiment was conducted analogous, but with loaded PDMS stamps after the first printing approach. With this approach, a similar structure as illustrated in Fig. 3.14 was achieved. Different samples of 4 µm silica spheres were embedded by the

printing process into a ink film produced by 2 wt% PEI. Afterwards the samples were exposed to increasing plasma etching times. Subsequently, the particles were released and the patch thickness was indirectly measured using AFM on the remaining holes on the dried stamps (compare section 2.10). The mean patch thickness t was plotted against the plasma etching time in Fig. 3.16. Again, a linear fit was used to calculate the change of patch thickness during plasma treatment, which resulted in $(0.3 \pm 0.1)\,\mathrm{nm\,s^{-1}}$. These results show that the etching speed is reduced to one third due to screening by the silica particles. Still, this indicates that the introduction of an additional plasma treatment step during the µCP process would lead to a decrease in patch thickness of the first printed patch. For a plasma treatment time of 60 s the decrease in patch thickness would be 20 nm. Printing results with low ink concentrations (1 & 2 wt%) did not show a asymmetrical patch thickness decrease of this magnitude. In fact, the asymmetrical behaviour was only observed for the highest applicable ink concentration as shown in the last section 3.20. Considering the last two measuring points in Fig. 3.16, showing almost no difference in patch thickness between 60 s and 90 s, a trend is visible. A possible hypothesis is, that the etching speed is stronger reduced by the shielding silica particles, if the ratio between ink film and particle size gets smaller and could possible reach a plateau value for the film thickness (approx. (25 ± 5) nm).

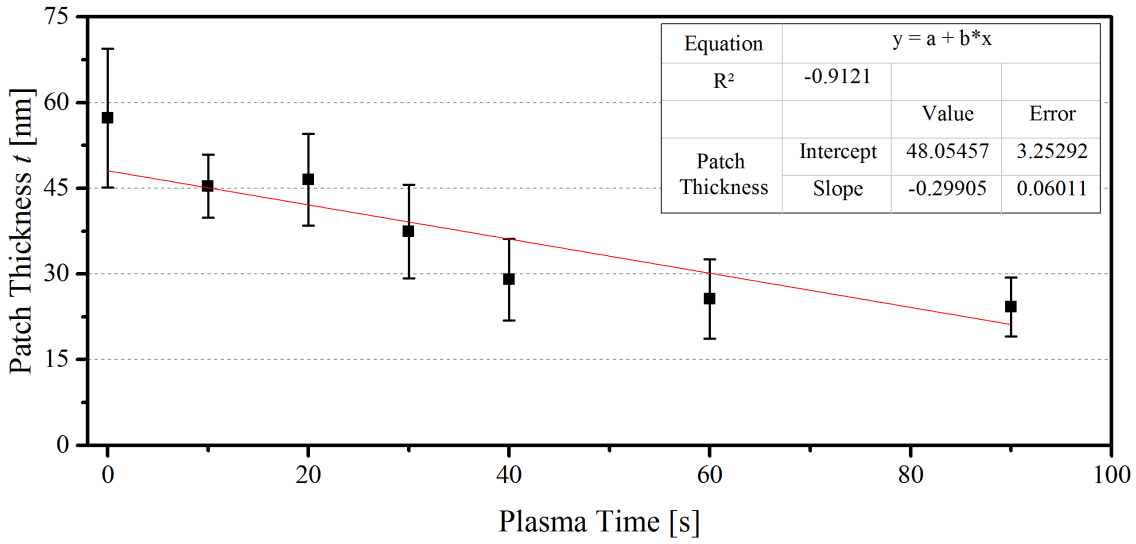

Figure 3.16 The diagram shows the indirectly measured thickness t of patches exposed to air plasma with increasing process time. A linear fit was used to calculate the change of patch thickness with time.

Additionally, the influence of plasma etching on the patch diameter was investigated, although DPP results in section 3.20 did not show a significant decrease of this value. Fig. 3.17 shows the diameter d, which was obtained directly by labelling the released particle from the previous experiment, measuring them with fluorescence microscope, and indirectly by using the AFM method on the PDMS stamps. As previously stated in section 2.10, AFM was in general not used to calculate the patch diameter of the produced patched particles, due to strong deformation of the remaining polyelectrolyte layer after release. However, it is clearly visible that the change of d cannot be measured by using the fluorescence microscope data, because no change within the error range is visible. Even a trend cannot be detected. Therefore the AFM data was obtained. In comparison to the fluorescence microscope values, the AFM measurements show an overestimation of the patch diameter due to contraction of the polyelectrolyte layer outside of the holes after particle release. This effect leads to an increase of the hole diameter on the PDMS stamps. Still, the influence of the plasma etching is visible.

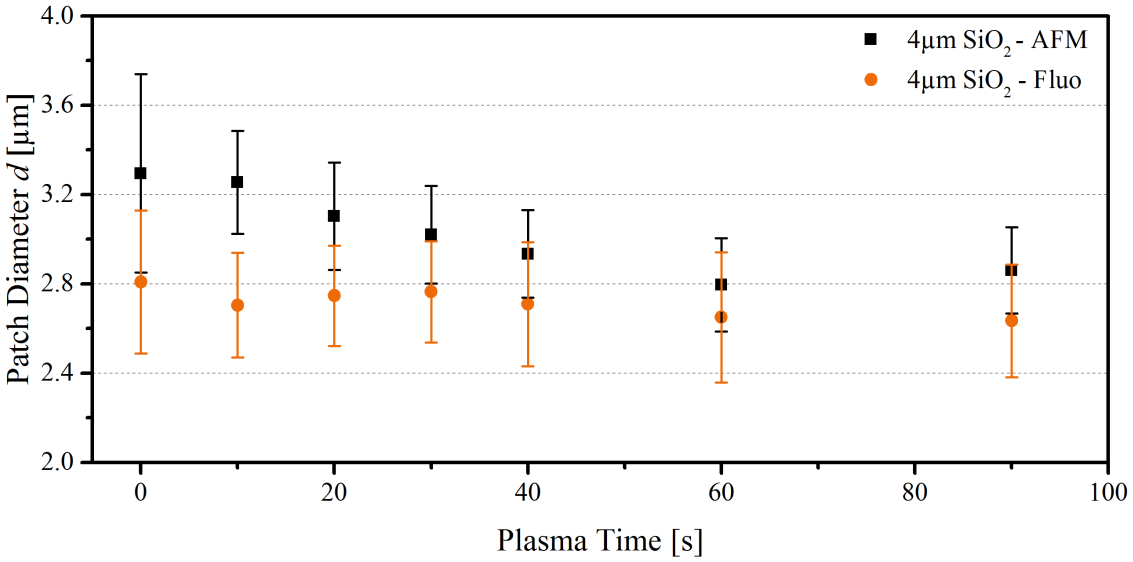

Figure 3.17 The diagram shows measured diameter d of patches exposed to air plasma with increasing process time. The parameter was investigated with labelled samples using fluorescence microscope and indirectly using AFM on the dried PDMS stamps after particle release.

The linear fit was applied to the AFM data in Fig. 3.18 and shows a decrease of the patch diameter d with a value of $(5 \pm 1)\,\mathrm{nm\,s^{-1}}$. As for the previous measurement, almost no change is detectable between 60 s and 90 s. Nevertheless, these values were included into the linear fit. Calculation of the patch decrease by using the 60 s plasma treatment during the µCP process gives a possible maximal value of 300 nm. However, this significant

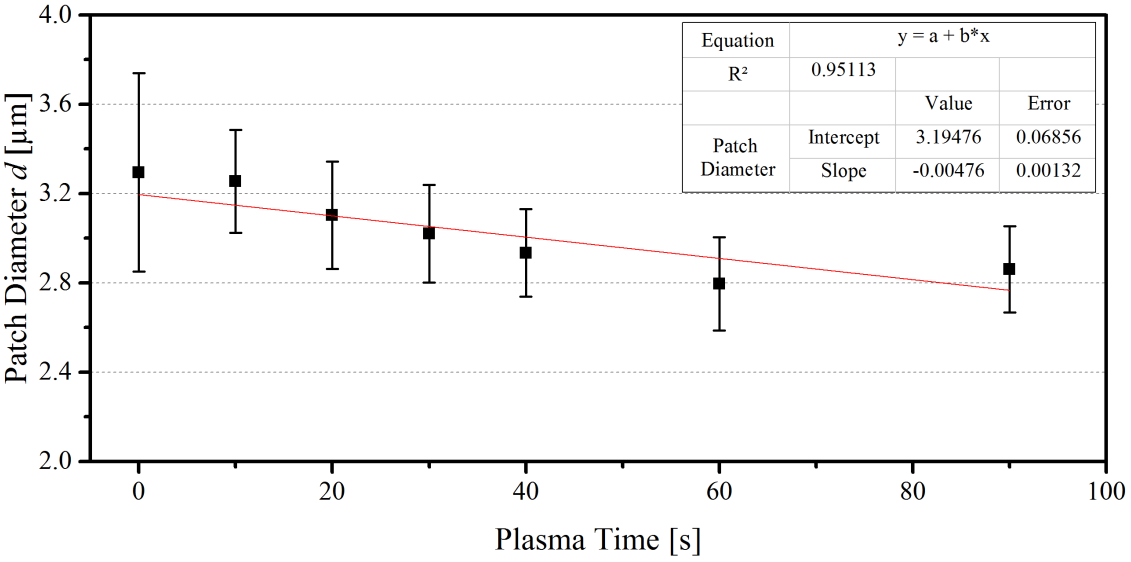

Figure 3.18 The diagram shows the measured diameter d of patches exposed to air plasma with increasing process time. The parameter was investigated indirectly using AFM on the dried PDMS stamps after particle release. A linear fit was used to calculate the change of d with time.

decrease in patch diameter was not visible for results in section 3.20.

The conducted experiments give an insight of the influence of plasma treatment during the µCP process on the patch geometry. Model experiments showed that a significant change of thickness and diameter[‡] is possible. However, these results were solely obtained by the indirect AFM method and could not be confirmed for the patch diameter by using fluorescence microscopy. Especially the patch diameter values are prone to overestimation, due to the ink layer contraction outside of the holes, which is clearly visible in Fig. 3.17. Futhermore, no significant asymmetrical geometry of the patches was observed for the DPP results, except for the highest applicable ink concentration. The most likely scenario is a complete shielding of the underlying PEI (the patch) by the silica particles. As a result, no significant etching and therefore no patch geometry change occurs. With this data it is save to say, that the plasma etching is a feasible intermediate process for the production of 3D DPP, which does not alter the geometrical shape of the first patch. Still, these results do not explain the asymmetrical patch geometry for DPP particles printed with the highest applicable ink concentration. Further discussions about this effect will be conducted in the following section.

[‡] $v_e(t) = (0.3 \pm 0.1)\,\mathrm{nm\,s^{-1}}$; $v_e(d) = (5 \pm 1)\,\mathrm{nm\,s^{-1}}$

3.3 Discussions and Comparison of Patch Parameters

This section will summarize obtained patch parameters for SPP and DPP of the previous sections. Initially, an overview of the patch geometry is given for all SPP and DPP printed with an ink concentration of 1 wt%. SEM images of these samples are displayed in Fig. 3.19 and 3.20 for SPP and DPP, respectively. The obtained patches are subsequently colourized for better visualization and all pictures possess the same scale, except Fig. 3.20(d), to give an impression of the achieved functionalization range of this μCP process.

3.3.1 Patch Diameter

The calculated patch diameters d for all samples are displayed in the diagrams of Fig. 3.21. The corresponding values can be found in section 9.1. In general, the patch diameter increases with increasing ink concentration and decreases with decreasing particle size. All SPP samples show a higher patch diameter as the corresponding DPP samples (except 5 µm with 3 wt%). Patch size distribution shows no significant change within a sphere size, but a slight broadening with increasing ink concentration. An unusual effect is the strong broadening of the DPP patch diameter distribution for the highest applicable ink concentration.

To further investigate this effect the two patches on DPP samples were additionally classified as larger and smaller patch. With this method, a diameter ratio R between the larger and the smaller patch was obtained and a mean value was calculated for every printing parameter (compare section 8.4.1). The resulting values are displayed in Fig. 3.22(b). All samples have a value below or close to 1.15, except the DPP particles printed with the highest applicable ink concentration. All of the later samples possess a value above 1.2, which was chosen as a self-imposed limit for symmetrical DPP. The decreasing diameter during DPP production and the asymmetrically sized patches for high ink concentration could evolve based on the same effect. During SPP production, a hard glass substrate is used as the counterpart of the soft PDMS stamp. In the case of DPP two soft PDMS stamps are used. As the same force was applied during all printing experiments, a softer stamp material leads to a damping of printing pressure. Therefore, the particles would not bend the PDMS stamp to the same degree and the patch diameter would decrease. That is in particular the case for the second patch as it is only applied during the second step. The

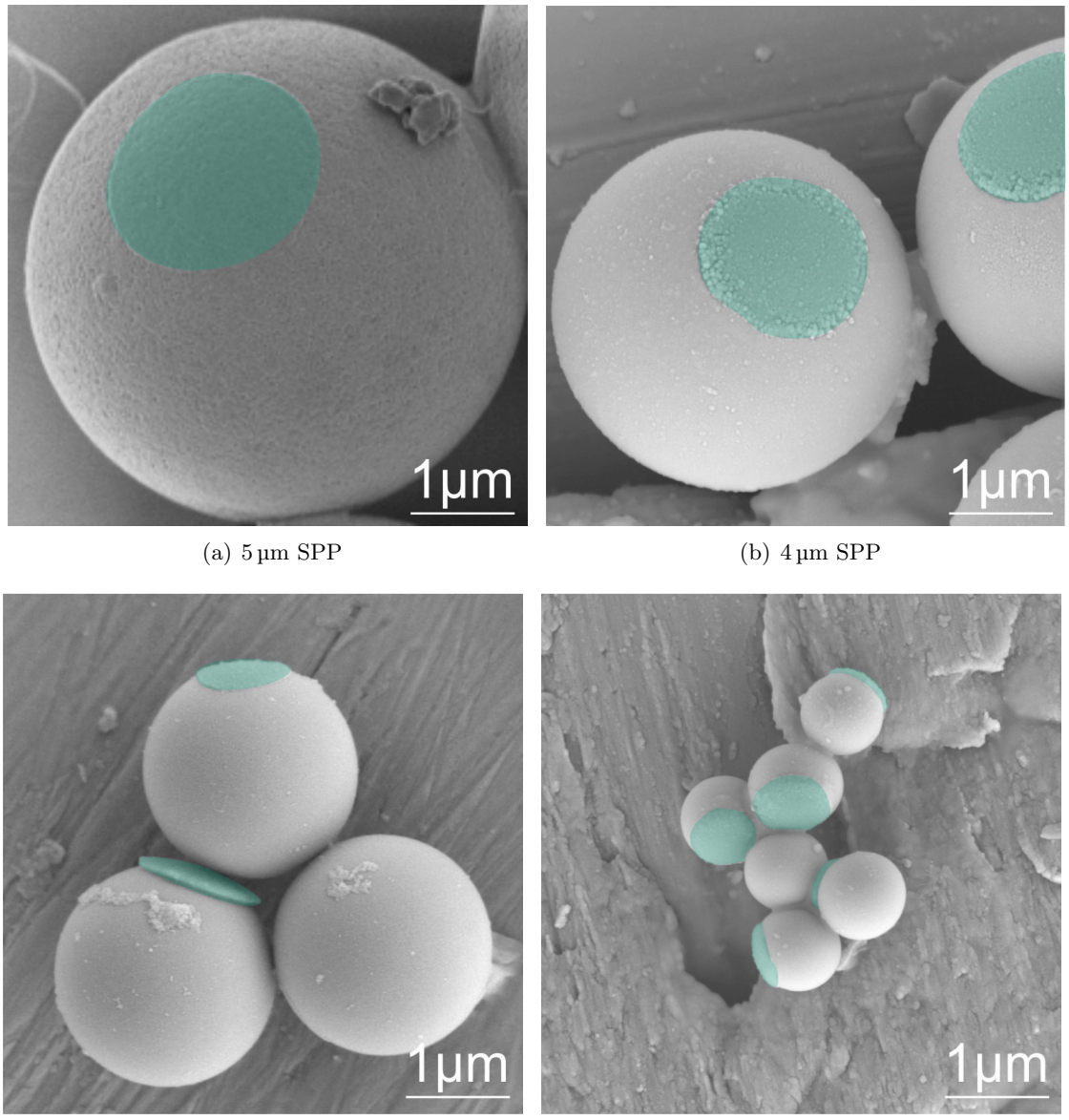

(a) 5 µm SPP

(b) 4 µm SPP

(c) 2 µm SPP

(d) 1 µm SPP

Figure 3.19 SEM images of all single patched particle sizes printed with 1 wt% PEI.

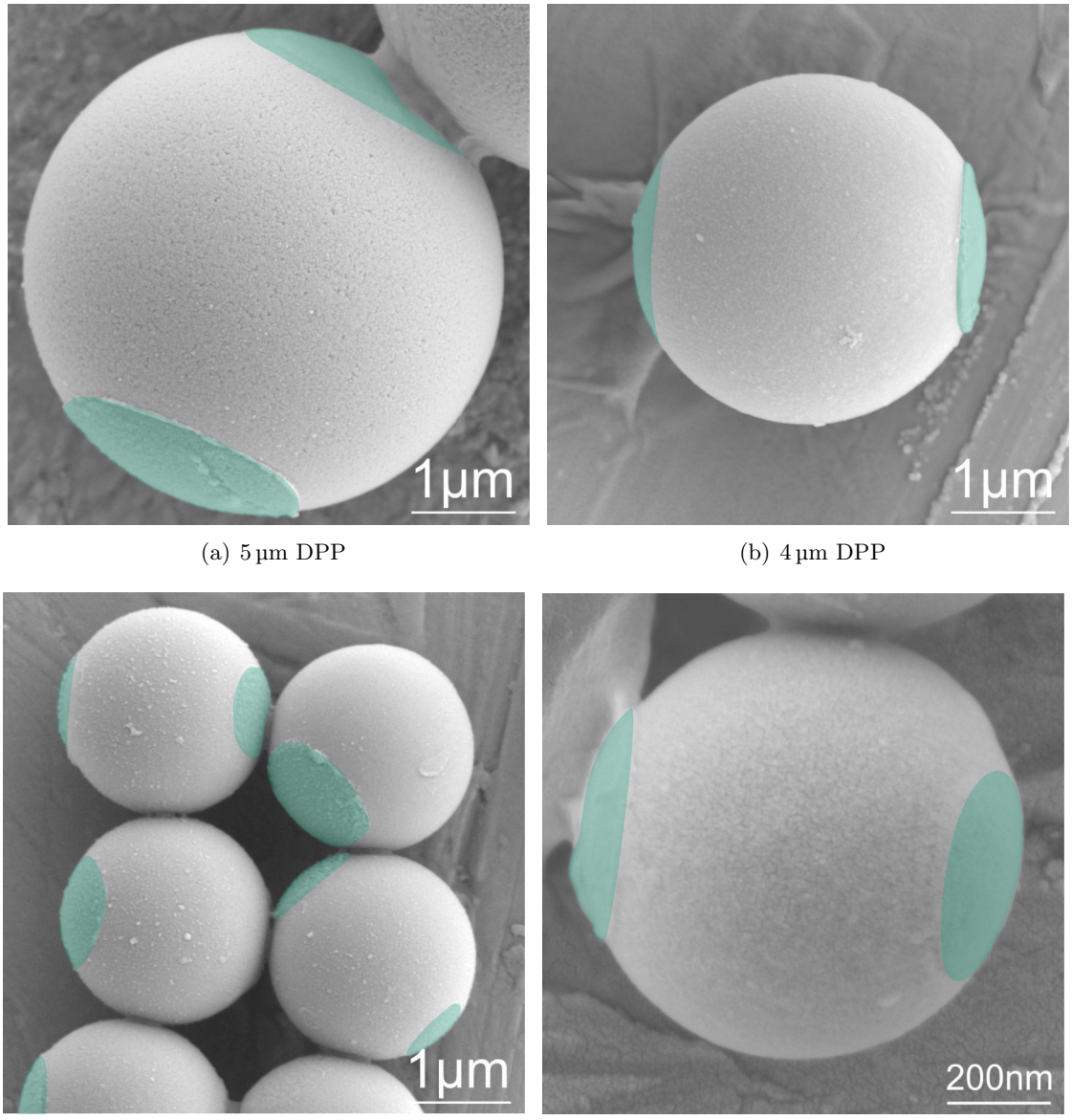

(a) 5 µm DPP

(b) 4 µm DPP

(c) 2 µm DPP

(d) 1 µm DPP

Figure 3.20 SEM images of all double patched particle sizes printed with 2 wt% PEI.

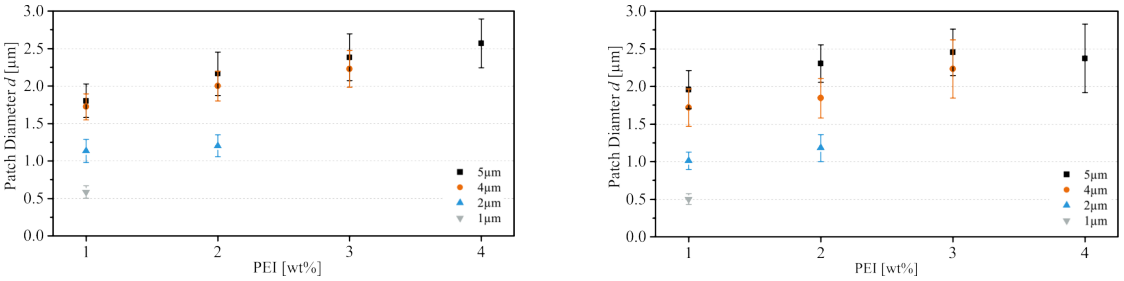

(a) Patch diameter of SPP (b) Patch diameter of DPP

Figure 3.21 Diagrams show the patch diameter for all single and double patched particles, including all particle sizes and PEI concentrations. Error bars represent the standard deviation.

first patch was obtained by printing against a hard glass substrate. However, only high ink concentrations seem to lead to a significant asymmetrical effect. It is possible that thicker polyelectrolyte films are not penetrated during the second printing step and therefore the particles are not completely embedded into the ink. During particle release only a fraction of the underlying ink is removed and smaller patches, in comparison to the first one, are produced. All results concerning DPP production are difficult to interpret, but lower ink concentrations achieve a good quality of trivalent particles with adjustable patch diameter.

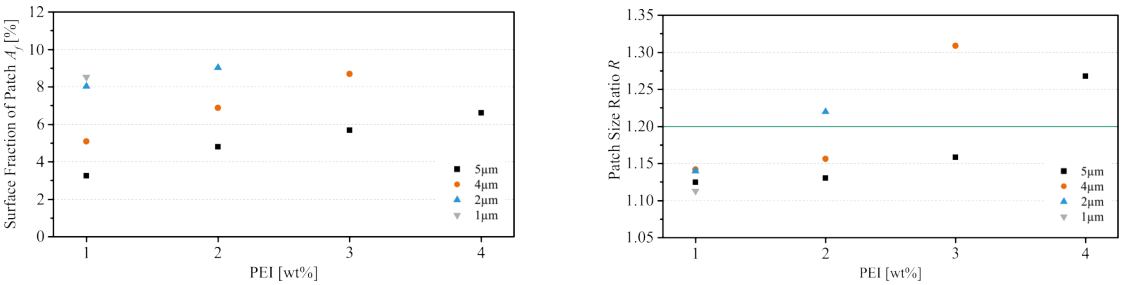

(a) Surface fraction of patch (b) Patch size ratio of DPP

Figure 3.22 Diagrams show the surface fraction of the patch for all SPP and the patch size ratio for all DPP, including all particle sizes and PEI concentrations. Error bars represent the standard deviation.

Additionally, another key figure was calculated, which is valuable for particle assembly experiments. Fig. 3.22(a) shows the surface fraction of the patch A_f for all SPP revealing the actual functionalized surface area. The corresponding values can be found in section 9.1. For this method, the patch size was calculated by assuming a disc-like shape for the patch and calculating the overall surface area of the particles (see section 8.4.1). These values range from 3.2 % for the 5 µm spheres printed with 1 wt% PEI up to 9.0 % for the 2 µm silica particles printed with 2 wt% PEI, which again shows the broad distribution range of this process. Controlling the patchiness of particles is an essential property for further self-assembly experiments.

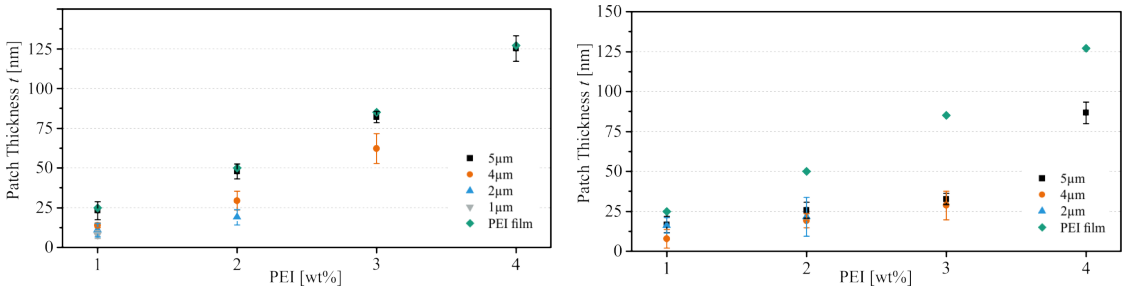

(a) Patch thickness of SPP

(b) Patch thickness of DPP

Figure 3.23 Diagrams show the patch thickness for all single and double patched particles, including all particle sizes and PEI concentrations. Error bars represent the standard deviation.

3.3.2 Patch Thickness

The patch thickness t measured indirectly via AFM is displayed in Fig. 3.23(a) for SPP and in Fig. 3.23(b) for DPP, respectively. The corresponding data is displayed in section 9.1. As introduced in section 2.5, the height of the PEI films deposited on silica wafer pieces was already measured. These values are additionally displayed in the diagrams to compare the measured results with the maximum achievable limit. Remarkably these values are in perfect agreement with the measured patch thickness for the 5 µm SPP. This course shows that a complete removal of the underlying PEI layer takes place for this particle size. Smaller particles achieve only reduced values. These results suggest two different explanations: First, the kinetic energy, which is produced in the ultrasonic bath during particle release, is higher for the 5 µm silica spheres and particle release is therefore faster. In the case of smaller particles the produced energy is reduced and therefore the release time is increased. During this longer time period the solvent is able to penetrate the ink and weaken the cohesion forces inside the PEI. Therefore a partial patch release is possible due to cohesion fracture and the patch thickness is decreased. The second more feasible explanation will be discussed in detail in section 5.2. In short, calculations have shown, that the printing pressure for individual particles decreases with decreasing particle size. This effect occurs due to a higher packaging of smaller particles and therefore a force distribution to a greater number of contact areas between the particles and the ink layer. For this reason smaller particles show thinner patches, as they are not as deeply embedded into the ink layer compared to the 5 µm spheres, because a reduced pressure is applied.

Corresponding t values for DPP are reduced in comparison to the SPP results. As already explained in the previous section for the patch diameter, this effect seems to be a

results of the usage of two soft stamping materials in contrast to the hard glass substrate used for SPP. Therefore, the second patch could be thinner, because particles are not completely embedded into the ink layer. Interestingly, all sphere sizes show among each other almost the same patch thickness for ink concentrations between 1 and 3 wt% PEI. A reason for this effect is difficult to discuss, as this effect was not visible for SPP particles. It is possible, that a differentiation is not possible due to the relative broad error margins and the smaller absolute values. A slight influence of the air plasma etching process is also still feasible (compare section 3.2.1).

Generally speaking, these results show that the production of real 3D patches is only to an extent transferable to trivalent particles. SPP reach applicable patch thicknesses up to 125 nm, while DPP only reach a value of 25 nm. Higher ink concentrations tend to result in asymmetrical patch geometries. Nevertheless, this effect could be an intended goal for particles with differently sized patches on the surface.

3.3.3 Patch Yield

A very important factor of this production techniques is a high yield of synthesized patched particles. The patch yield Y was obtained for 3D SPP and DPP (released in acetone) by fluorescence microscopy as the mean value of different FITC labelled samples (compare section 8.4.1). Tab. 3.1 displays the achieved yields for single patched particles and various printing parameters. Patch yield was not obtained for 1 µm silica particles, because of insufficient data volume.[†] Fluorescence microscopy was difficult at this particle size due to high Brownian motion and therefore the identification of real patches. The remaining SPP sizes show a patch yield over 85 % for all printing parameters. These are excellent values and could possible be even higher. Due to particle rotation, missing patches could be concealed behind the sphere, averted from the camera field of view.

The corresponding results for the patch yield of DPP are displayed in Tab. 3.2 and confirms this explanation. The table shows Y_{DPP} values, corresponding only to clearly visible particles with two distinct patches, and Y_{SPP} values, which show only one patch. In this case, even if particle rotation is present, at least one surface functionalization is always visible due to the 180° angle between the patches. These results show a mean $\bar{Y}_{\mathrm{SPP}}$ value for all printing parameters of (94 ± 5) %, which means almost full conversion for the

[†]Patch yields were not calculated for samples below 50 particles.

Table 3.1 The patch yield for 3D single patched particles Y_{SPP} at different particle sizes and increasing ink concentration obtained by fluorescence microscope.

PEI [wt%]	$Y_{SPP\ 5\,\mu m}$	$Y_{SPP\ 4\,\mu m}$	$Y_{SPP\ 2\,\mu m}$
1	86 %	98 %	87 %
2	90 %	93 %	86 %
3	88 %	86 %	
4	92 %		

Table 3.2 The patch yield for 3D double patched particles Y_{DPP} at different particle sizes and increasing ink concentration. Y_{SPP} of the same samples also included.

PEI [wt%]	$Y_{DPP\ 5\,\mu m}$ (Y_{SPP})	$Y_{DPP\ 4\,\mu m}$ (Y_{SPP})	$Y_{DPP\ 2\,\mu m}$ (Y_{SPP})
1	69 % (96 %)	98 % (100 %)	73 % (91 %)
2	81 % (97 %)	78 % (93 %)	70 % (94 %)
3	57 % (86 %)	79 % (100 %)	
4	72 % (92 %)		

production of 3D single patched particles via microcontact printing. The mean $\bar{Y}_{DPP}$ value with (76 ± 11) % ranges clearly below, but some printing parameters remarkably showed conversions up to 98 %. However, as the production of trivalent particles showed generally lower performance in comparison to single patched particles, a full conversion is not to be expected for this by hand approach, without further mechanical assistance.

3.4 Multi Patched Particles[†]

Following the μCP approach for the production of SPP and DPP using flat stamps, the possibilities of wrinkled structured substrates were investigated. For this, wrinkled stamps were produced by stretching and simultaneous air plasma treatment of PDMS pieces (compare section 2.3). During this research it was discovered, that printing would not be successful using these stamps due to their hard surface. To achieve wrinkles with high wavelengths ($\lambda \geq 1\,\mu m$), a long plasma treatment time is necessary, which results in a thick silicon oxide layer. This drawback was circumvented by moulding of PDMS replica of these wrinkles. For this approach, the original PDMS stamp was functionalized

[†]Results in this section were conducted in cooperation with Daniela John from Fraunhofer IAP. They are described in detail in her dissertation and in a joint publication.[87,96] The underlying concept and data evaluation were performed together, while Daniela John synthesized the wrinkled substrates and executed the printing.

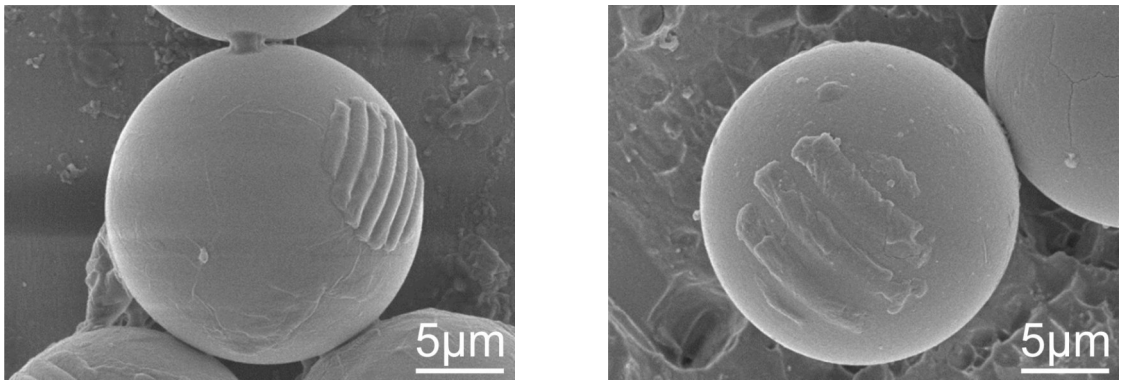

(a) $\lambda = 1.5\,\mu m$ (b) $\lambda = 3\,\mu m$

Figure 3.24 SEM images of MPP produced by printing 20 µm silica particles with different wrinkled stamps loaded with 4 wt% PEI. The decrease of striped structures on the particle surface with increasing wavelength λ is visible.

with n-octyltriethoxysilane by gas phase silanization to passivate its surface. Afterwards a replica was formed by pouring freshly mixed PDMS over the original stamp. After crosslinking the two stamps could be separated from each other and the new soft wrinkled stamp could be used for microcontact printing experiments.

SEM images in Fig. 3.24 display 20 µm silica particles, which were printed from one side with wrinkles possessing different wavelengths λ. The stamps were loaded with 4 wt% of PEI. A transfer of the striped structure onto the particle surface is clearly visible. As expected, smaller λ values led to a higher number of lines per modification side (or patch). With a wavelength of 1.5 µm a patch consists of seven individual PEI lines was achieved. By doubling the wavelength to 3 µm a number of three to five lines is visible, depending on the particle and distinctness of the transferred structure. To show that this line transfer from wrinkled stamps is also feasible for the sandwich approach, differently labelled polyelectrolyte inks were prepared and printed onto opposite sides of the particles. The resulting fluorescence microscope images are illustrated in Fig. 3.25. The figure includes light, fluorescence and overlay images. For these large silica spheres the line structures are already slightly visible via light microscope. The fluorescence channel displays the two distinctly labelled particles sides in red and green (RBITC & FITC), which confirms successful sandwich printing for these set of parameters. The geometry of sandwich printed MPP is even better visualized via SEM in Fig. 3.25(d). A curiosity of this approach is the transfer of thick structures rather then lines consisting of polymer monolayers onto the particle surface. The reason for this observation is an effect during spin coating of the ink. Investigations on loaded wrinkles showed that the polyelectrolyte

is filling the grooves during this process rather then evenly distributing across the PDMS surface. Therefore, the transferred structures are again replicas of the wrinkles. This transfer from the groove during microcontact printing is known as *intaglio* printing. In the course of this dissertation no further experiments were conducted using structured PDMS or other stamping materials.

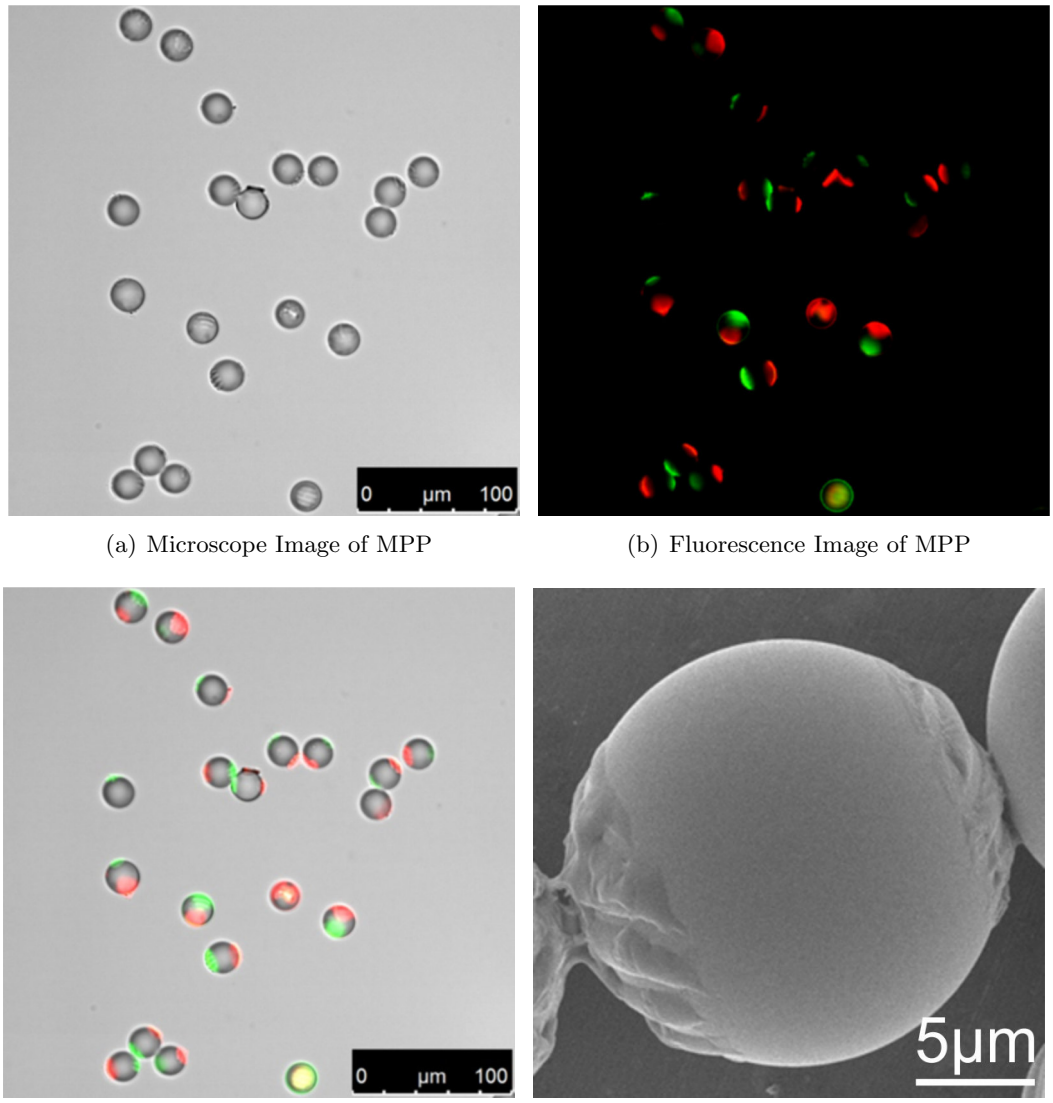

(a) Microscope Image of MPP

(b) Fluorescence Image of MPP

(c) Overlay Image of MPP

(d) SEM Image of MPP

Figure 3.25 Fluorescence microscope and SEM images of sandwich printed 20 µm silica particles using wrinkled PDMS stamps. The wavelength λ of the wrinkles is 3 µm. Different coloured PEI patches were labelled using fluorescein isothiocyanate (green) and rhodamine B isothiocyanate (red) prior to printing process.

CHAPTER 4

Self-Assembly of Anisotropic Particles

A detailed evaluation of the achievable geometries of patchy silica particles has been described in the previous chapter. However, it did not comment on their behaviour in solution nor on further functionalization methods leading to sophisticated coupling. This chapter will initially introduce the electrostatic behaviour of divalent particles achieved by printing with polyethylenimine ink in alcoholic and aqueous solutions, as well as its particular reaction to changing pH. Furthermore, magnetic, biological and supramolecular coupling systems specificly, adapted for this μCP process, were investigated to find the most promising tool for prospective self-assembly experiments.

4.1 Electrostatic Interactions and pH Dependence

Initially, there was a strong expectation to observe random self-assembly behaviour between the printed particles (SPP & DPP) in aqueous solutions, as the underlying mechanism of the μCP approach is based on the electrostatic interaction between the negatively charged particle surface and the positively charged polyethylenimine. However, this effect was not observed during first microscope experiments in ethanol or water. At first it was assumed that the labelling agent was responsible for the missing attraction between patches and particle surfaces. The labelling agent FITC was originally introduced in order to visualize the patches. FITC reacts with free amine groups on the PEI patch and therefore shields the positive surface which could interact with particle surfaces. To investigate this effect experiments without it were conducted.

Fig. 4.1 displays microscope images of 5 µm SPP without further functionalization or labelling with fluorescent dyes. A highly concentrated dispersion of particles in water was prepared to amplify possible impacts, which would lead to self-assembly. Although some connected particle are visible at this high concentration, the majority of particles do not

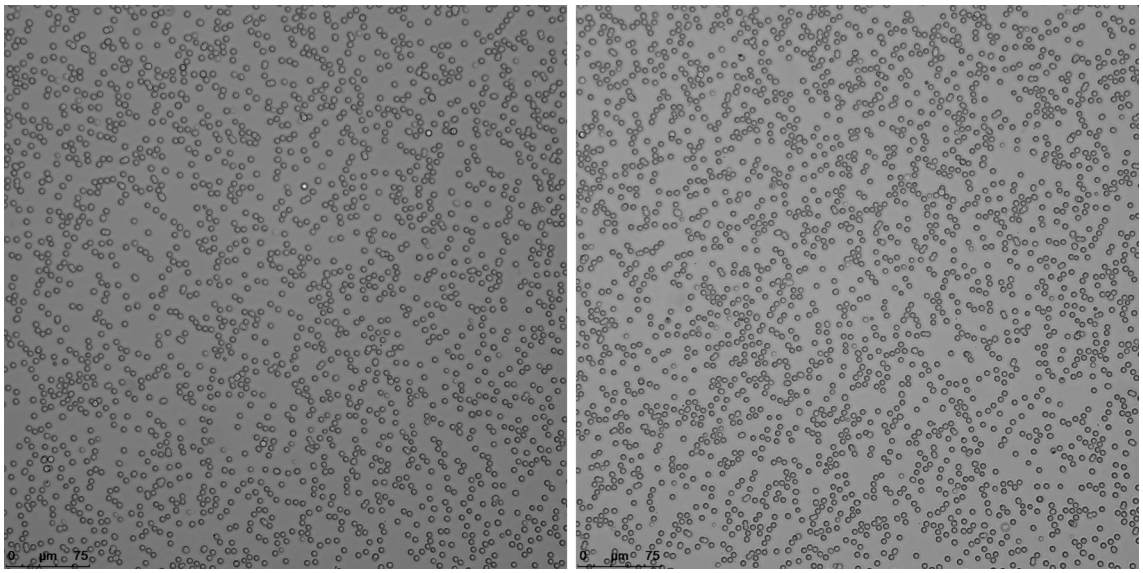

Figure 4.1 Light microscope images of non-functionalized 5 µm SPP printed with 3 wt% PEI and subsequently dispersed at high concentration in water.

assemble in any manner. Also, no large agglomerates were visible in this sample due to successful treatment in an ultrasonic bath. A clear indication for no or only insufficient attraction forces between the two oppositely charged surfaces. It seems that this system does not fulfil the requirements for coupling behaviour between divalent particles.

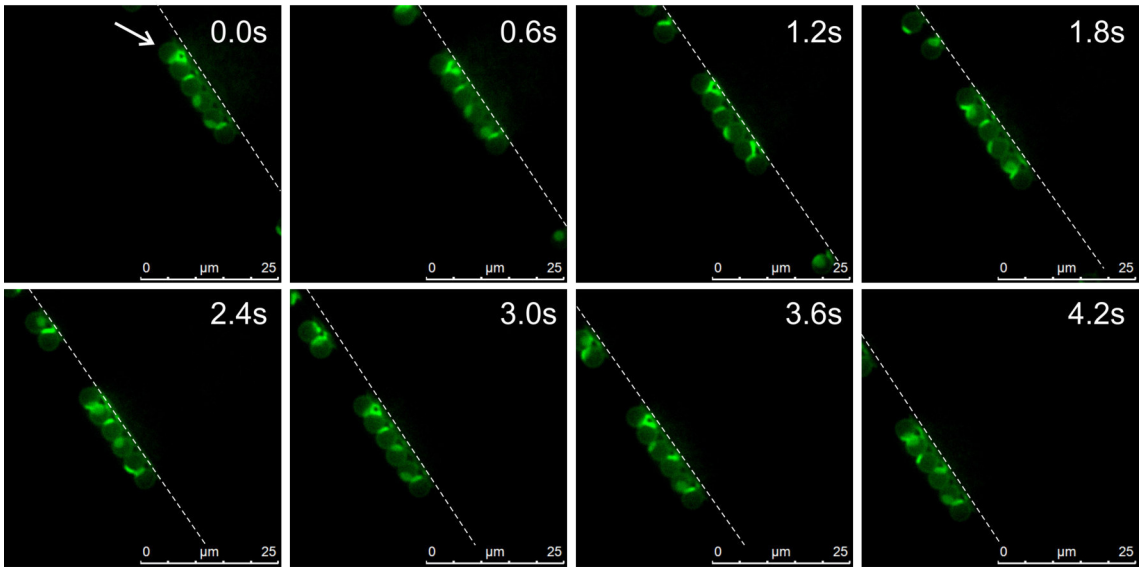

Figure 4.2 This series of images shows 4 µm SPP printed with 3 wt% PEI and labelled with FITC at a moving ethanol-air interface (striped line).

To proof this statement, a special scenario was documented and analysed using fluorescence microscopy. The series of pictures in Fig. 4.2 shows a couple of printed and labelled SPP at a moving ethanol-air interface (striped line). The particles are in direct

contact with each other, but still retain their rotational freedom without visible attraction forces between the particle-particle, patch-patch or particle-patch surface. At this point an attractive coupling between the divalent patches without further chemical or physical modification was excluded.

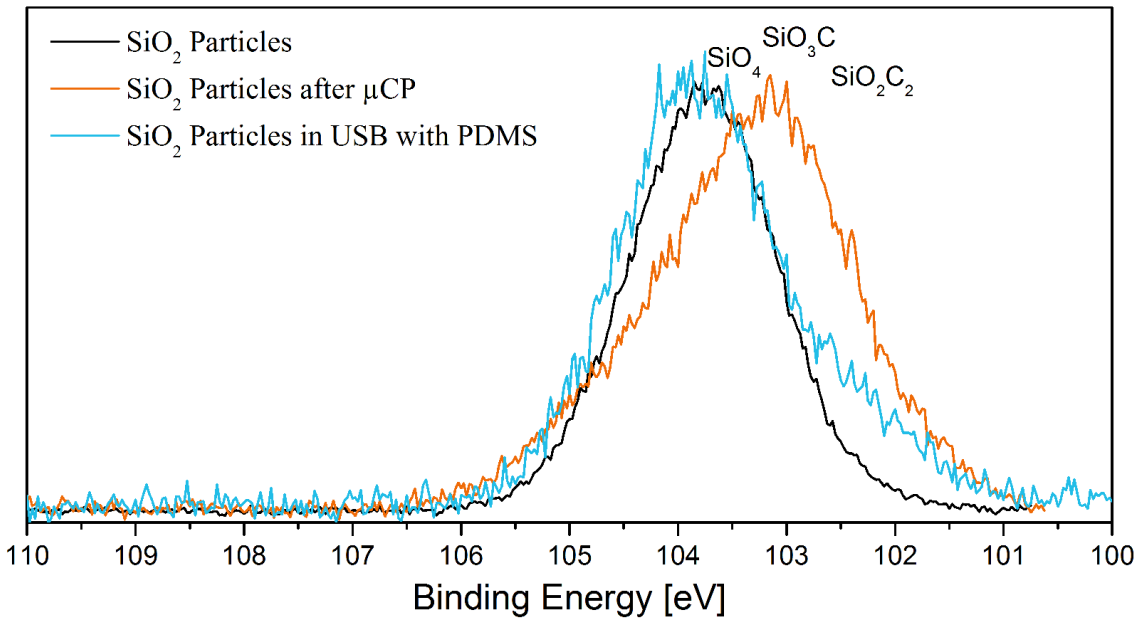

Figure 4.3 Diagram shows the silicon oxide binding energy region measured by XPS.

A reasonable explanation for this behaviour was found by investigating another peculiarity of PDMS stamps. Commonly the transfer of low molecular weight fragments of PDMS during printing is possible. These oligomers can contaminate the substrate during printing, as small chains can diffuse from the inside of the PDMS stamp. Publications on this effect have shown, that this transfer can be minimized using oxygen plasma treatment to seal the surface of the stamp by oxidizing PDMS, leading to a silicon oxide layer.[191] In the course of this research the same process with comparable parameters was used to prevent sample contamination. Nevertheless, additional XPS experiments regarding this problem were conducted. Fig. 4.3 shows XPS measurements of the binding energy region of silicon for three varying samples. The first sample was a blank test of purchased silica particles. Only one clear signal corresponding to the SiO_4 group of silica particles was observed. The second sample shows silica particles with printed PEI patches. The signal shows a poorer signal-to-noise ratio due to the low concentration of measured particles and a slight shift to lower binding energies. This shift can be explained by the presence of SiO_3C and SiO_2C_2 groups indicating a slight contamination of the printed samples with

PDMS oligomers. A final experiment was executed to exclude the diffusion of oligomers from the PDMS stamp during the particle release. For this, blank silica particles were dispersed in acetone, a piece of PDMS stamp was submerged into the solvent and this mixture was treated for 25 min in an ultrasonic bath to simulate the particle release process. The XPS results show again a worse signal-to-noise ratio due to low concentration, however no shift of the binding energy peak is observed and hence no diffusion of oligomers from the PDMS stamp during particle release occurs. These results show clearly that a slight transfer of PDMS oligomers takes places during microcontact printing. Therefore, it is possible that a small amount of hydrophobic chains are still located on the patch surface and shield the positive charge of the underlying amine groups. An attractive force between the silica particle surface and PEI patches would be prevented. These results would explain the missing strong agglomeration of the printed particles in aqueous solutions. Admittedly, these findings were initially very unpleasant, because further chemical functionalization would be impossible due to shielding. However, as the following sections 4.3 and 4.4 will show, that is not the case. Results indicate only a slight presence of PDMS oligomers, which do not interfere with patch modification, but do prevent strong agglomeration of divalent SPP in aqueous solutions, which is a huge benefit for self-assembly experiments.

To additionally investigate the stability of printed PEI patches in water, pH dependent experiments with SPP were conducted. Fig. 4.4 shows a series of microscope images of labelled SPP at increasing pH values. Between a pH value of 4 and 10 all particles show clear patches without any disintegration. The patch stability in water at intermediate pH values is good, although no time resolved experiments were conducted. It is to be expected, that during a longer time period polymer chains could dissolve from the patch surface. Exceeding the iso-electric point of the silica surface or of the polyethylenimine at a pH of 2 and 12 respectively, a new behaviour becomes observable. Remarkably, PEI patches detach from the particle surface without losing their structural integrity. This fact is a strong argument for the used high molecular weight PEI and its particular entanglement during spin coating. The stability of the PEI patches in water is still intact without electrostatic stabilization from the particle surface. The detachment itself is explained by the reduction of charged groups on the silica surface or the polyethylenimine, respectively. If the pH is reaching values below 3, particle surface groups (e.g. hydroxy groups) will be protonated and therefore losing the electrostatic bonding. At pH values higher then 11 PEI

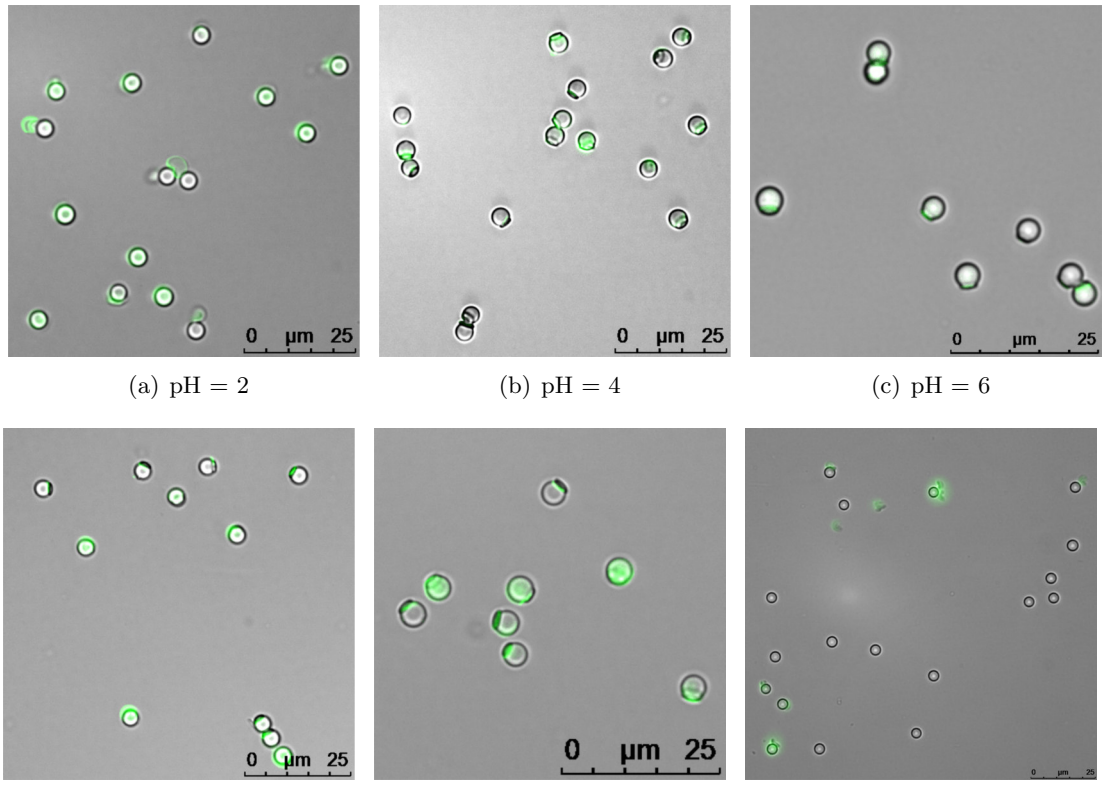

(a) pH = 2 (b) pH = 4 (c) pH = 6

(d) pH = 8 (e) pH = 10 (f) pH = 12

Figure 4.4 Light microscope images of single patched particles at different pH values.

becomes deprotonated leading to the same results. This mechanism could be deliberately triggered to detach coupled particles, release incorporated nano additives from the patch into surrounding solvent or to recycle already printed silica particles. Accordingly another potential function is introduced into this simple system.

4.2 Magnetic Coupling using Superparamagnetic Nanoparticles

As stated before in section 2.9, it is possible to incorporate nano additives into the polymer matrix of the PEI patches by dispersing them into the polymer ink prior to spin coating. For that reason, superparamagnetic iron oxide particles were purchased to investigate the possibility of magnetic field directed self-assembly of SPP particles (Fig. 4.5).[192,193] Without a magnetic field the domains inside of superparamagnetic materials (Weiss domain) do not possess an external magnetic dipole. However, by applying a field the domains align and a single nanoparticle exhibits a magnetic dipole $\vec{m} \neq 0$.[194] The proposed concept is based on the idea that an external magnetic field induces self-assembly between different particles, by magnetically bonding of their patches. The subsequent addition of a homobifunctional linker should stabilize the coupling between the PEI patches by crosslinking of free amine

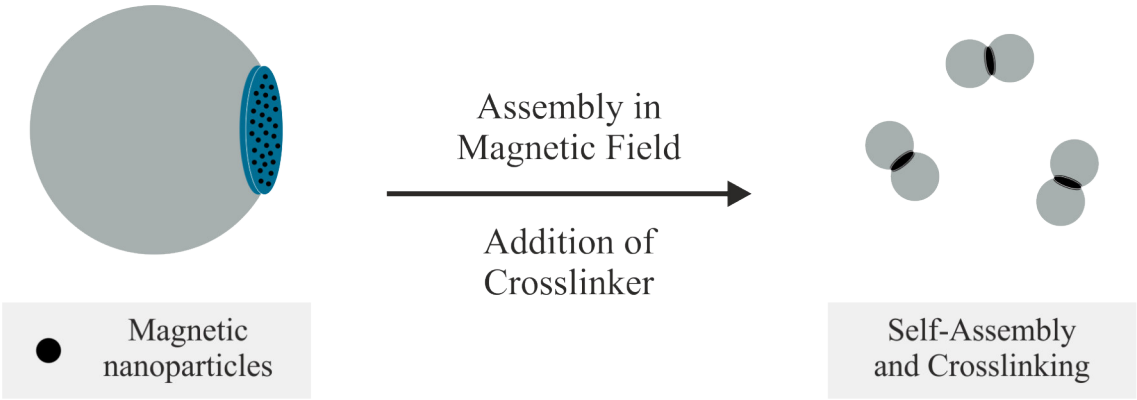

Figure 4.5 Schematic diagram of the SSP coupling using superparamagnetic nanoparticles as nano additives inside the patches. After applying an external field the printed patches should assemble and the addition of a homobifunctional linker should enable stable coupling.

groups. After this step the external magnetic field could be removed without losing the established particle dimers. For other applications a detachment of the particles without crosslinking could be achieved by simple removal of the external magnetic field. Subsequent experiments would introduce trivalent particles with two magnetic patches for self-assembly into particle strings.

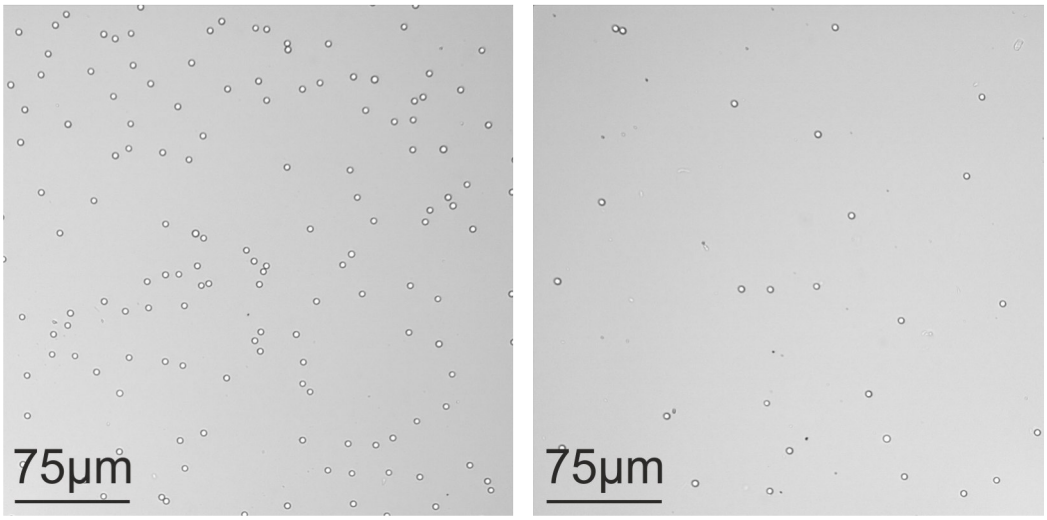

Figure 4.6 Light microscope images show 4 µm SPP with superparamagnetic iron oxide nanoparticles incorporated into the PEI patch after alignment in the magnetic field and addition of a homobifunctional crosslinker.

However, although this concept seemed promising and would have been a very elegant way for self-assembly application, it was experimentally not successful. Fig. 4.6 displays microscope images of 4 µm SPP with incorporated superparamagnetic iron oxide nanoparticles after self-assembly between two neodymium magnets and addition of the crosslinking agent. A detailed protocol can be found in section 8.2.6. The figure shows large scale

images of magnetic SPP, however non of them showing any observable self-assembly into dimers. Several attempts have been conducted following slightly adjusted protocols, but no sufficient dimer formation could be achieved. As there are multiple possible sources of error leading to an unsuccessful experimental result, this concept was discarded. One of the first explanations was the failed incorporation of the nano additives into the PEI patch. As no indirect measurement was possible in contrast to quantum dots (fluorescence signal), it was not certain if the iron oxide nanoparticles would be embedded into the PEI matrix. An alternative experiment using 1 µm SPP under otherwise comparable conditions was conducted showing an unusual results, but simultaneous providing the proof for successful incorporation of magnetic nano additives into the patches of larger silica particles.

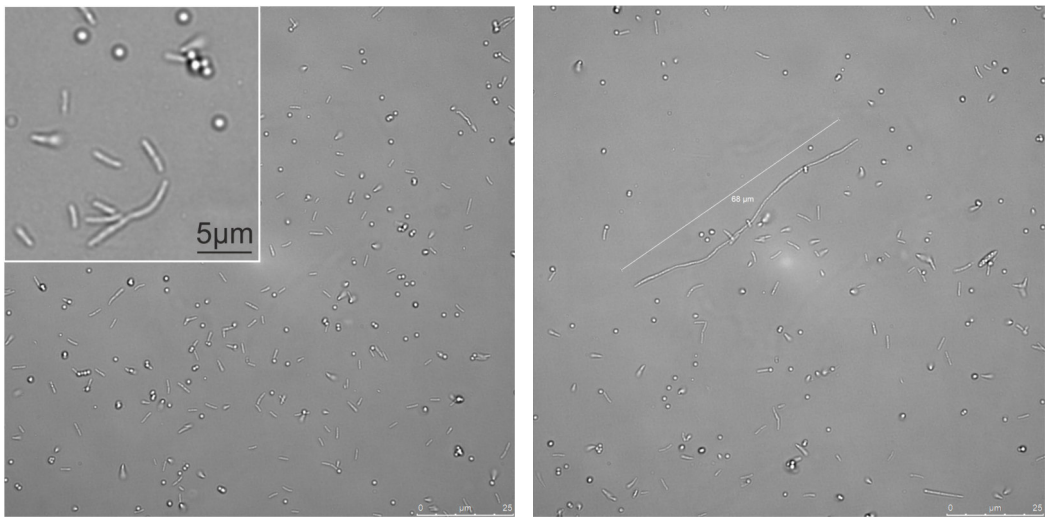

Figure 4.7 Light microscope images show 1 µm SPP with superparamagnetic iron oxide nanoparticles incorporated into the PEI patch after alignment in the magnetic field and addition of a homobifunctional crosslinker. Observable lines consisting of superparamagnetic iron oxide nanoparticles.

Fig. 4.7 displays further microscope images of 1 µm SPP with incorporated magnetic nano additives after alignment in an external magnetic field. As described in chapter 3 the polymer ink thickness had to be reduced for printing on smaller silica particles. Therefore the achieved patch thickness t for 1 µm SPP was reduced to (8 ± 2) nm. As the used nano additives possess an average diameter of (20 ± 5) nm, they cannot be completely embedded into the PEI patch, but can be at least attached to the particle surface. The images show isolated silica spheres and in addition long thin line- or rod-like structures. Some of these structures reach a length of up to 68 µm. As there are no other components, these structures must consist of magnetic nanoparticles, which were detached from the PEI patch and aligned by the external field along the magnetic field lines. During microscope imaging

the formed structure are still stable. These findings show two important results: First, the alignment of the magnetic nano additives in an external magnetic field is possible. Second, the embedding of the nano additives into thicker PEI patches (e.g. on 4 µm SPP) is successful, as no self-assembly of iron oxide particles into rod-like structures was observed. However, these findings also seem to indicate that the magnetic force between different patches is not strong enough to create a stable bond between the used SPP. Additionally, it is not clear how the particle interact inside the patches. It could be possible that the attractive forces of the nano additives only occurs inside the PEI patch and does not reach below the patch surface. This effect could lead to agglomeration of the nanoparticles inside the patch or destruction of the surrounding polymer matrix, if the magnetic field is strong enough. As already mentioned further experiments were discarded, because to many questions arose during this investigation, leading to too many additional experiments. This section is intended to be a cause of thought for following research attempts, as it is not clear if other experimental conditions could still lead to a favourable result.

4.3 Avidin-Biotin Coupling

In contrast to the previously described attempt of incorporating magnetic nano additives into the PEI patch, this section describes the chemical functionalization of later with avidin and biotin to induce self-assembly between printed particles.[195,196] The avidin-biotin complex is used in various biotechnological applications due to its high affinity constant for the production of stable biomolecular structures.[197,198] Furthermore, the following approach illustrates the versatility of three-dimensional patches by utilizing the created unused volume as well as the high density of functional groups on their surface. This concept using 5 µm silica spheres is illustrated in Fig. 4.8. Detailed protocols of the described approach can be found in section 8.2.5. As a first step, two different particles species were designed. While both were printed with the same PEI concentration (3 wt%) and under the same printing condition, one was fluorescent labelled using quantum dots inside the 3D patch by blending them into the polymer ink prior to printing. After the release in acetone the quantum dots remain in the thick PEI matrix, adding a further physical properties to the system. With this approach it is possible to mark certain particles without changing the chemical surface of the patch or the particle.

Fig. 4.9(a) shows a FM images of the quantum dot labelled species. The fluorescence

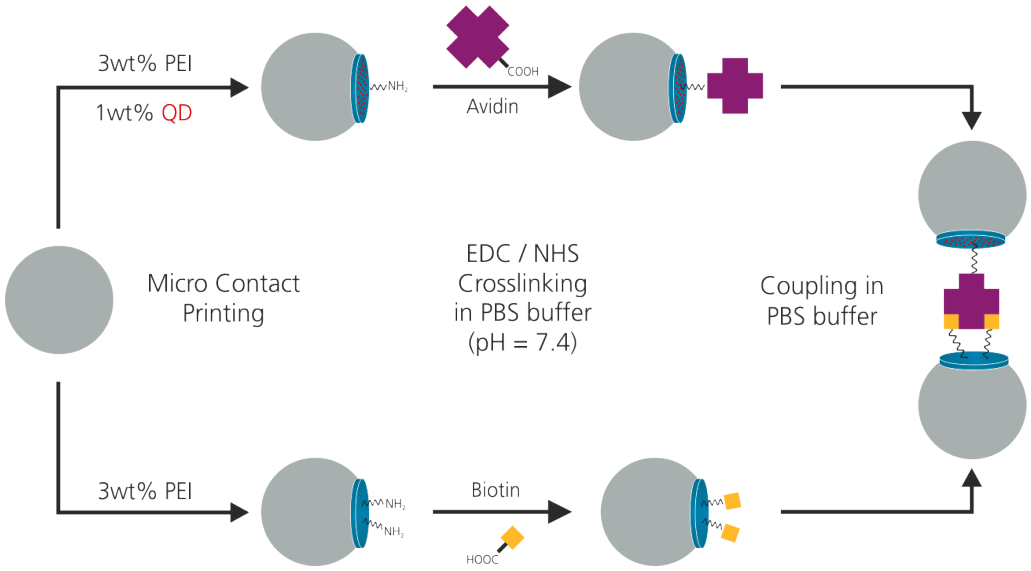

Figure 4.8 Schematic diagram of the synthesis route for avidin and biotin functionalized single patched particles for the formation of coupled heterodimers.

signal contrast is very good and throughout this research no leakage of quantum dots into the surrounding solvent was observed. That is a very important factor as other positively charged surfaces could otherwise be contaminated by the negatively charged quantum dots, e.g. the PEI patches of the second particle species. For the sake of completeness, a sample of the second species was labelled with FITC to test for successful printing prior to further functionalization. The corresponding results are displayed in Fig. 4.9(b). The next step was the patch modification of labelled and unlabelled species with avidin and biotin, respectively. The chemical modification was conducted using the established EDC/NHS method which activates the carboxilic acid groups of avidin and biotin with a reactive NHS ester. This ester reacts in a second step with the free amine groups on the patch surface.[199,200] Fluorescence microscope images in Fig. 4.9(c) and 4.9(d) were recorded in PBS-buffer to verify that no agglomeration of the two distinctly functionalized species with each other took place during this stage (additional images see appendix 9.3.2). Labelled avidin-SPP and biotin-SPP did not show any agglomeration at this point. Biotin-SPP did not show fluorescent labelling, as the free amine groups were occupied by the attached biotin and no subsequent highlighting using FITC was conducted.

Finally, both species were joined and mixed together in water for 15 min. Afterwards fluorescence microscope images were recorded and are displayed in Fig. 4.10. Due to the strong binding forces between avidin and biotin, the modified SPP self-assembled into heterodimers, as only one particle shows a fluorescent signal. It is clearly visible that the

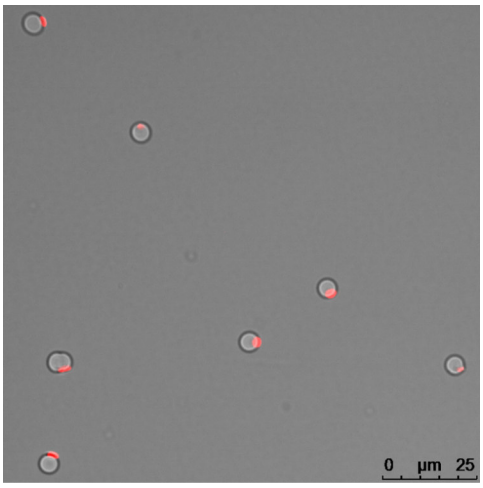

(a) SSP labelled with Quantum Dots

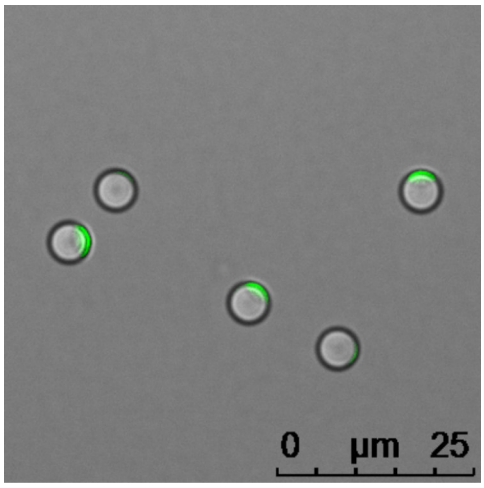

(b) SSP labelled with FITC

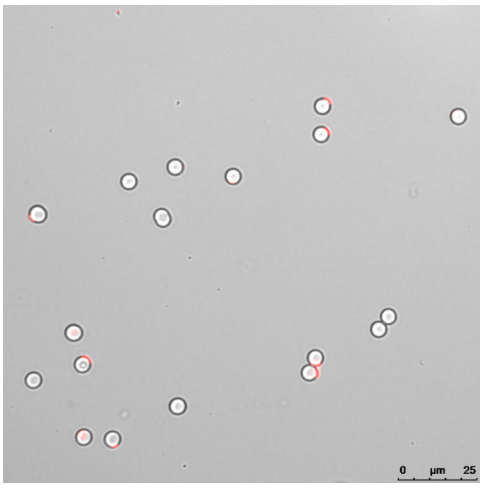

(c) Avidin-SPP in PBS

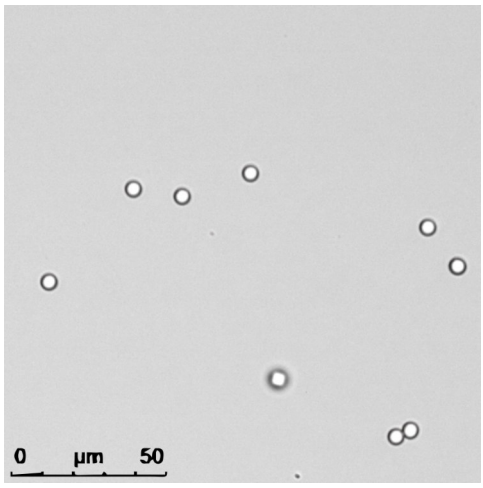

(d) Biotin-SPP in PBS

Figure 4.9 Fluorescence microscope images of labelled SPP prior and after modification with avidin and biotin via EDC/NHS coupling. Image were taken in water and PBS-buffer respectively.

particles bind along the line connecting their centres, through the labelled avidin-patch. In order to give a qualitative statement on the achieved coupling, a statistical evaluation was conducted. For this process, several microscopic images of the mixed sample were analysed for three different particle species: Coupled heterodimers, free or agglomerated fluorescent avidin-SPP and the corresponding biotin-SPP. With these values it was possible to calculate a maximum amount of achievable heterodimers in this sample, consisting of a single avidin- and biotin-SPP. The corresponding microscope images can be found in section 9.3.2. With this method a binding efficiency of up to 55 % could be achieved. This is an impressive value considering the large size of these silica particles (5 µm), the rather low concentration deliberately chosen and the fact that a successful coupling is only possible for a direct collision between two complementary patches. The motion of silica

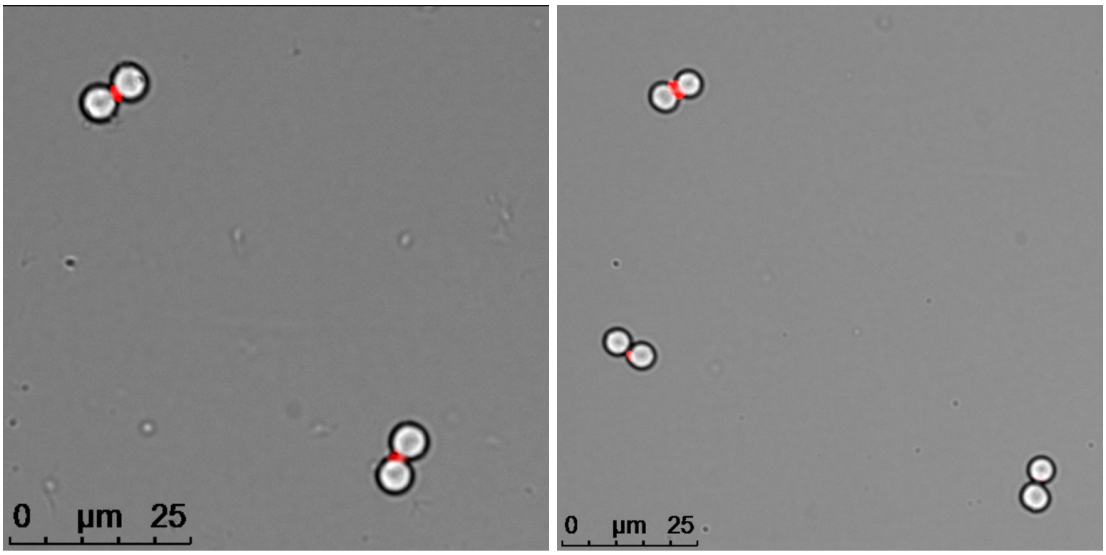

Figure 4.10 Achieved avidin-biotin heterodimers after joining of both modified particle species.

particles of this size is mainly affected by gravity and not by Brownian motion. Therefore, the efficiency of the used system is very high and underlines again the high accessibility of the used 3D patches.

4.4 Supramolecular Coupling using Host-Guest Chemistry[†]

After the successful coupling of printed particles using avidin and biotin, other coupling systems with additional functionality were investigated. The light responsive host-guest chemistry consisting of cyclodextrins (CD) and azobenzenes is a well established and switchable coupling system.[201–210] The attractive interaction between azobenzene and the cyclodextrin is based on an entropy gain in solution. The circular cyclodextrin possesses a cavity and while it is dissolved in water, this space is normally filled with water molecules. In its non-polar linear *E*-isomer form the azobenzene can enter this cavity replacing the water molecules and therefore leading to an increase in entropy. For this reason, all experiments with this system had to be performed in aqueous solution. Still, this coupling is not irreversible. The azobenzene is not trapped inside the CD molecule and is able to freely leave the host molecule. The two substances are in a constant dynamic equilibrium leaning on the side of the host-guest complex. By radiation of the azobenzene compound with UV light the molecule can be switch into its polar and bend *Z*-isomer. In this chemical configuration the molecule cannot access the CD cavity. Therefore, the

[†]Cyclodextrin and arylazopyrazoles derivates used in this section were kindly synthesized and provided by Sven Sagebiel from the University of Münster.

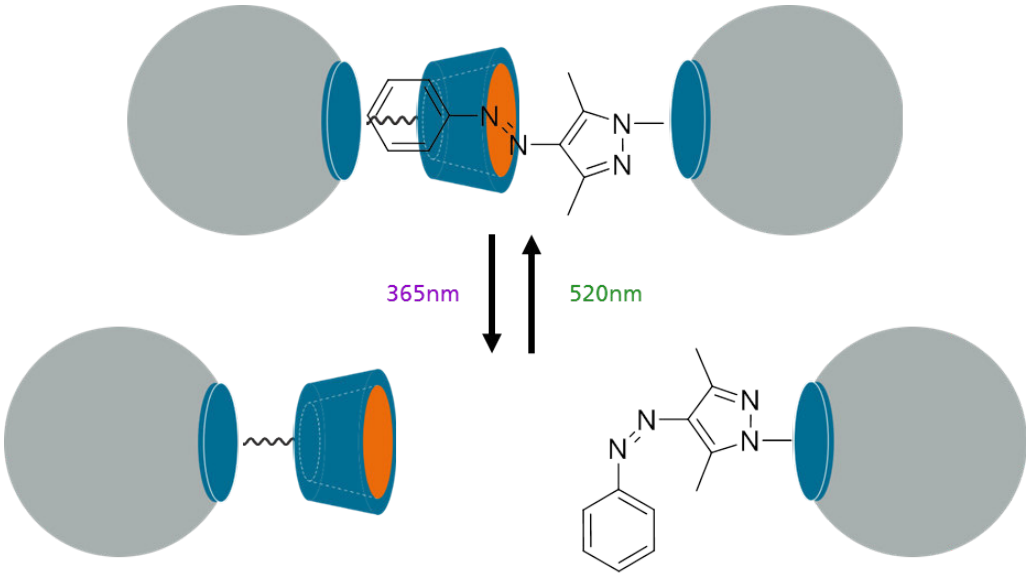

Figure 4.11 Schematic diagram of cyclodextrin and arylazopyrazole functionalized single patched particles for the formation of heterodimers.

equilibrium is shifted onto the released form of the guest molecule. A problem of this azobenzene system is its incomplete photoswitching and the low thermodynamic stability of the *Z*-isomer. These problems have been addressed by Stricker *et al.* by modifying the chemical structure of this guest molecule by using water soluble arylazopyrazoles (AAP).[211] This coupling system was transferred onto divalent single patched particles and its concept is displayed in Fig. 4.11. Two different species of SPP were modified with CD and APP functionalities respectively. This functionalization was conducted similar to the already described avidin-biotin approach using EDC/NHS coupling, because both provided molecules possessed a carboxyl group for attachment (compare section 8.2.5). After functionalization the two species were dispersed in water and afterwards joined and mixed for 15 min to produce heterodimers. Without any further radiation treatment AAP molecules possess its non-polar and linear form, which is able to access the CD cavity. To increase the number of generated heterodimers by improving the collision frequency, a smaller silica particle size of 2 µm was chosen, in comparison to avidin-biotin coupling. However, as patch thickness measurements for 2 µm spheres have shown that the value for t only reaches (19 ± 5) nm, no quantum dots were incorporated into the PEI patches to prevent cross contamination of potentially leaking nano additives.

Fig. 4.12 shows microscope images of the coupled heterodimers. In comparison to previously shown results for the avidin-biotin coupling, the concentration of formed heterodimers has been significantly increased. Nevertheless, images still show particles

without coupling partner. A reason for this findings could be a mismatch in numbers of CD and AAP modified particles in the system. In such a scenario one species could ran out of possible counterparts. Another point could be insufficient time during self-assembly or an unsuitable mixing form. The best results concerning this point, were obtained by carefully tilting of the sample inside a closed vessel, so that the dispersion is fully moved from one side of the container to the other. More intensive mixing methods, e.g. ultra sonification, led to no or only insufficient dimer formation. In comparison to the avidin-biotin coupling, this system seems to be more vulnerable to external kinetic energy, which could be explained by its dynamic nature and could be deliberately used to cleave the formed dimers. Still, a binding efficiency was calculated for this system. Corresponding images can be found in section 9.3.3 (compare Fig. 9.13). Under these condition that the uncoupled particles consist of an equal amount of CD and AAP modified particle, a binding efficiency of 72 % was calculated. The usage of smaller silica spheres and the transfer to another coupling system was therefore successful and even higher binding efficiency could be achieved.

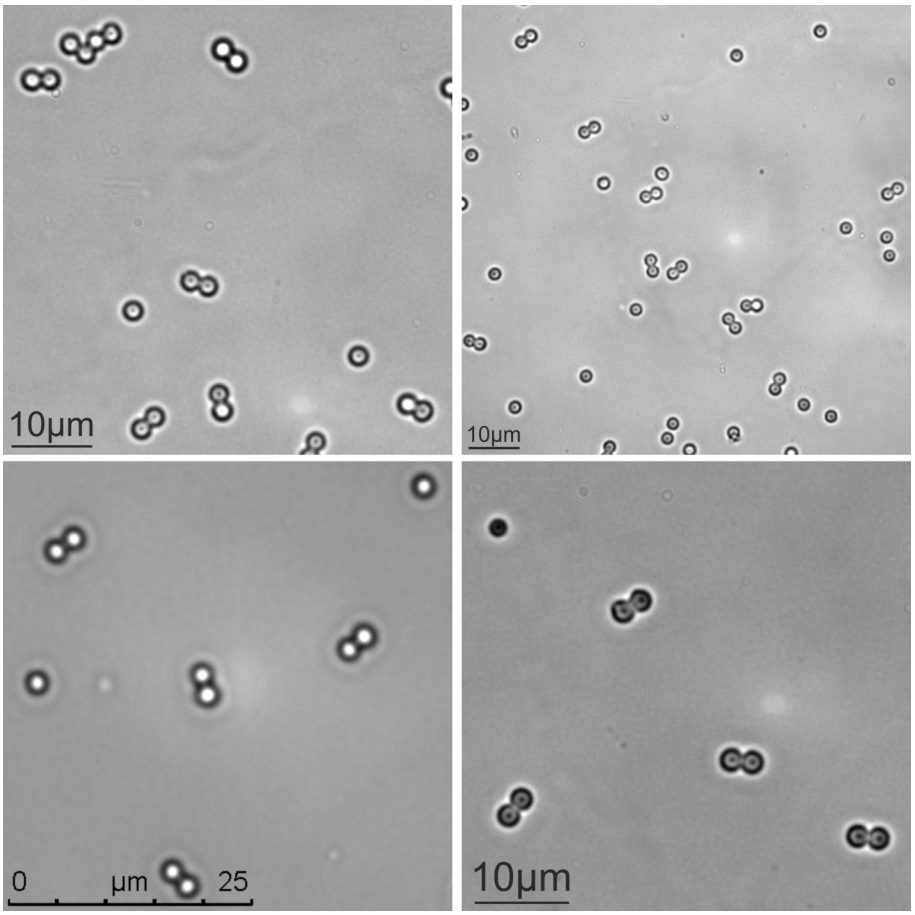

Figure 4.12 Light microscope images of single patched particles functionalized with cyclodextrin and arylazopyrazole during their formation into heterodimers.

4.5 Self-Assembly of Amphiphilic Particles in Various Solvents

Besides the self-assembly investigations on physical incorporation of nano additives and the chemical modification of the patches, another synthesis route was explored. The concept is based on the enormous library of easily available silanes, which allows a high flexibility and a wealth of possibilities for chemicals systems.[212] Combined with simple reaction conditions it forms an ideal tool for the functionalization of silica particle surfaces. Normally, particle functionalization is conducted in alcoholic or dry organic solutions based on the reactivity of the used alkoxysilane. However, for our approach, combining microcontact printing and silica particle modification, chemical vapour deposition is more suitable.

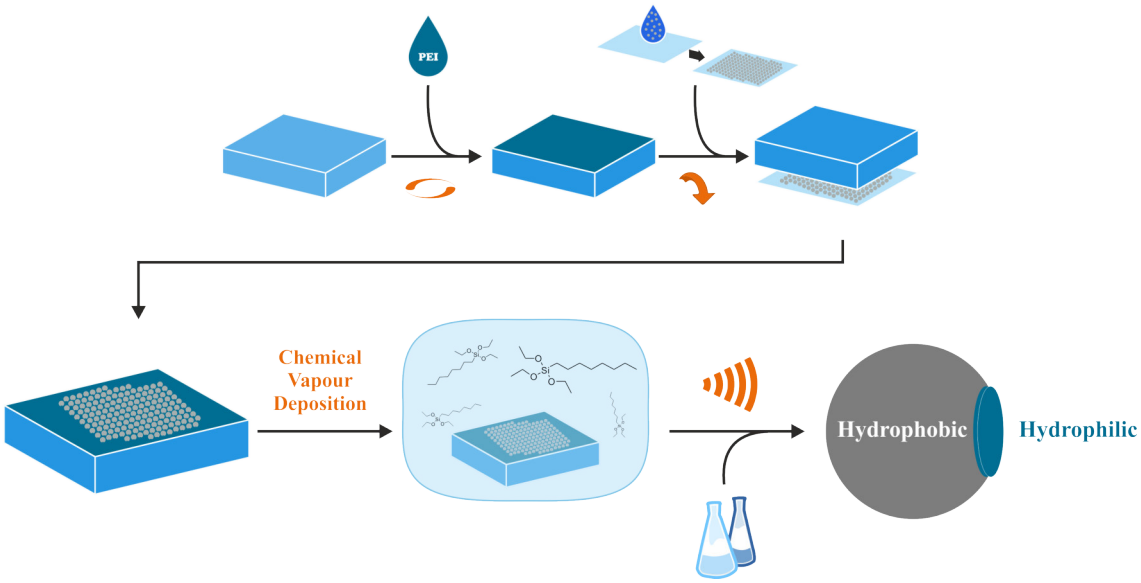

Figure 4.13 Schematic diagram of the synthesis route for amphiphilic SPP, by chemical vapour deposition of octyltriethoxysilane after the first printing process.

Fig. 4.13 displays the synthesis route of this approach. The idea was to keep the particles attached to the PDMS stamp after the first printing step. Therefore the blank silica surface pointed upwards and is easily reachable by chemical vapour. The reaction can be conducted inside a desiccator with a silane reservoir under reduced pressure in order to initiate the gasphase reaction. After functionalization the loaded PDMS stamps can be removed from the desiccator and the modified particles can be released from the stamp as usual by ultrasonication. For this approach, hydrophobic octyltriethoxy silane was chosen for the production of highly amphiphilic particles. A detailed description of the modification process can be found in section 8.2.5. Microscopic images of modified particles, released from the stamp using acetone and labelled with FITC, are displayed in Fig. 4.14.

The particles are thoroughly dispersed in ethanol using ultrasonication to observe if the printing is still successful. An overall great quality of patches on the particles was obtained. The printing process and especially the particle release mechanism is not prevented by the vapour deposition or the applied low pressure. Additionally, no large amount of bigger agglomerations are visible. This means that ethanol is still an adequate solvent for the modified particles, despite their highly amphiphilic surface. To investigate the influence of different solvent polarities on the structure formation of amphiphilic particles, modified particles were transferred into water, ethanol and toluene, thoroughly dispersed using ultrasound. Afterwards samples were placed into coverglass container with lid to prevent solvent evaporation and were allowed to self-assemble freely for 30 min. Although all particles showed good stability in all solvents, small agglomeration could be observed for all polarities. FM images of these measurements are displayed in Fig. 4.15.

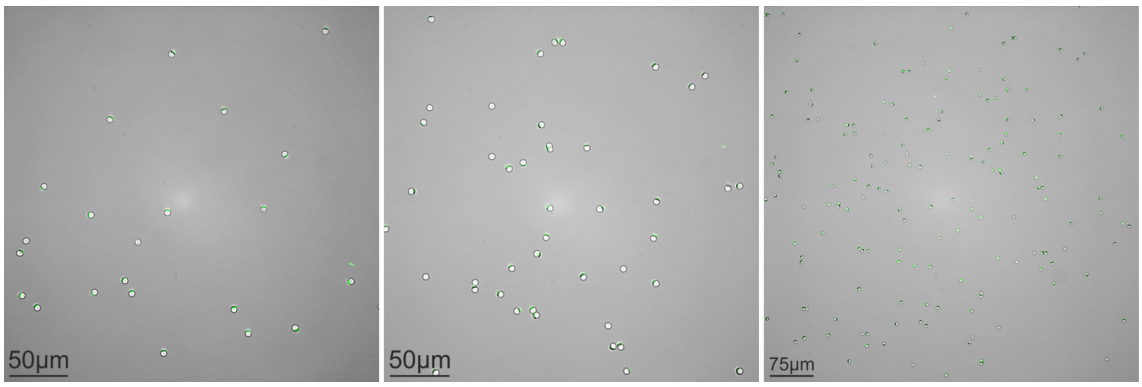

Figure 4.14 Light microscope images of amphiphilic patched particles labelled with FITC dispersed in ethanol using ultrasonication.

First, amphiphilic particles in water were observed. All three images show small particle structures aligned and floating. All hydrophilic patches consisting of polyethylenimine are directed outwards pointing to surrounding water. The particles are connected to each other with the modified hydrophobic surface. Second, the particles dispersed in ethanol are shown. These images do not enable distinct statements regarding patch orientation as some point inwards, but the majority displays the same behaviour as previously observed for particles in water. Finally, the toluene samples show the complete opposite. All patches visible for these agglomerations, are directed inwards, shielding the hydrophilic patches from the non-polar solvent.

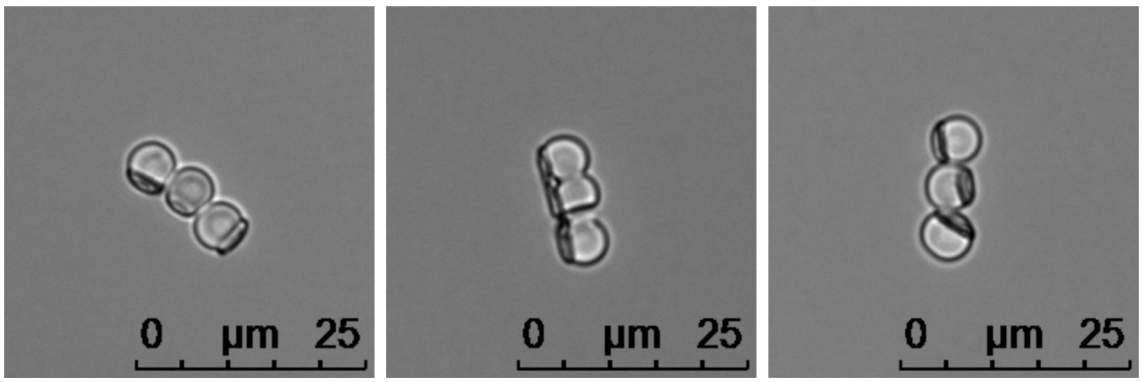

(a) SSP in Water

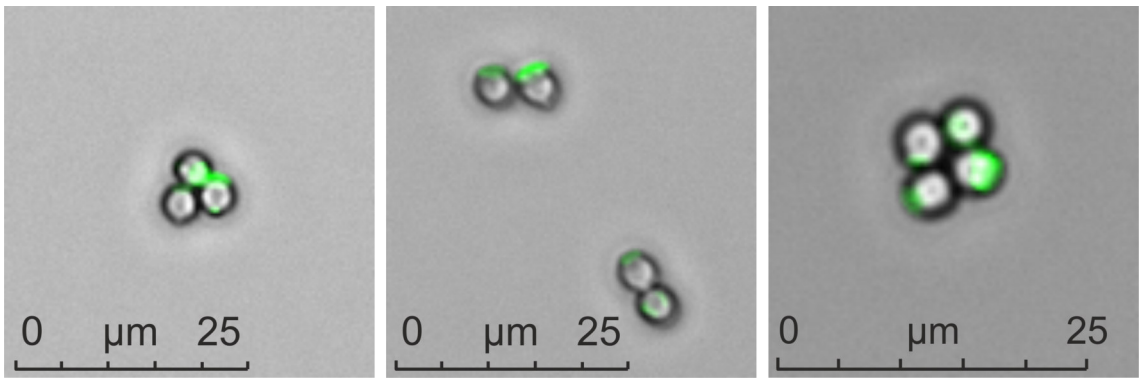

(b) SSP in Ethanol

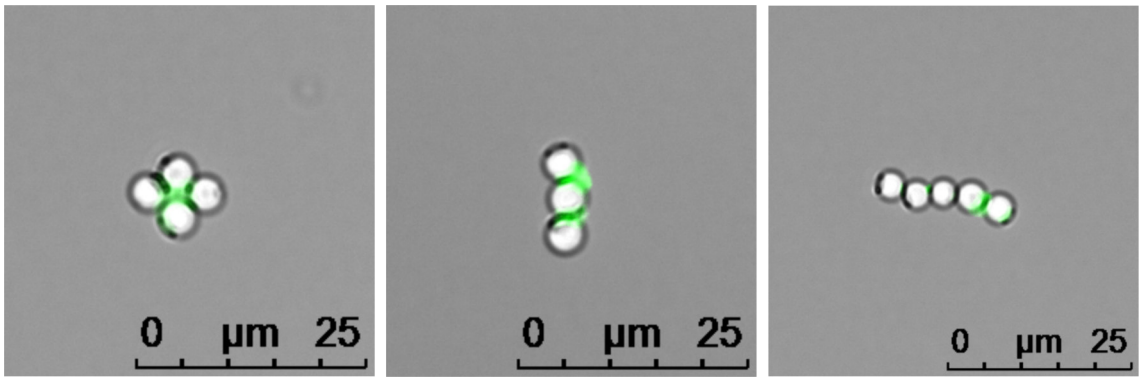

(c) SSP in Toluene

Figure 4.15 Light microscope images of amphiphilic patched particles labelled with FITC showing their cluster formation in different solvents.

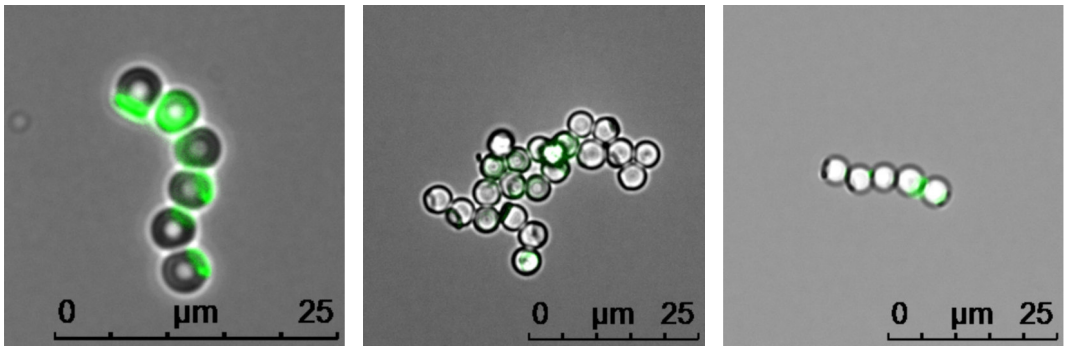

(a) SSP in water (b) SSP in ethanol (c) SSP in toluene

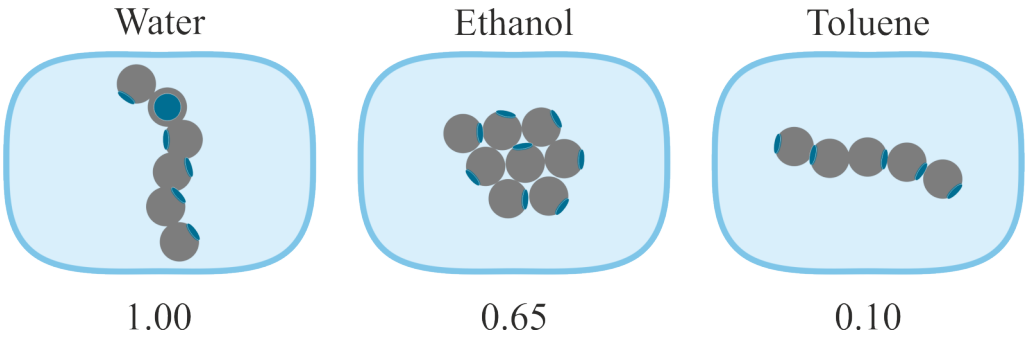

Figure 4.16 Light microscope images of two distinct cluster formations of amphiphilic patched particles and a schematic diagram illustrating the cluster formation depending on the relative polarity of the solvent.

This behaviour is described in more detail in Fig. 4.16. Fluorescence images of three agglomerates in different solvents are displayed, accompanied by two-dimensional sketches to clarify the evolved structures. By scaling the relative polarity of water to 1.00 the variation between the solvents becomes more clearly, as ethanol and toluene possess a relative polarity of 0.65 and 0.10, respectively.[213] The string like structure obtained in water shows that all hydrophilic patches are turned outwards due to the high polarity of water. In contrast to this behaviour, the achieved line structure in toluene illustrates the shielding of patches from the very non-polar toluene. In between, an unstructured agglomerate in ethanol does not show any preferred direction of the patches. These images show how a simple intermediate step can alter the behaviour of printed particles in various solvents. Using this process in combination with other reported coupling systems could lead to a higher recognition number between particles and prevent wrongly aligned couples. Furthermore, as already mentioned, this technique is not limited to modification with alkyl chains as presented here. Silanes with more sophisticated structures or functional groups could be used to directly induce crosslinking events between particles.

CHAPTER 5

Theoretical Considerations and Control of Printing Pressure

The preceding investigation have shown the achievements of this new microcontact printing approach and its recognisable scope of application. Certain characteristics however, require still further considerations. The following topics are mainly accompanied by simple mathematical solutions, which serve as a basis for discussion. First, the recurrent measurement of relatively broad error margins for patch diameters achieved by all printing conditions was analysed and its connection to the naturally occurring particle size distribution was investigated. Second, a more detailed discussion about the differences concerning printing pressure for various used particles sizes is conducted. This evaluation will conclude in a new sophisticated method for microcontact printing using centrifugal force.

5.1 Influence of Particle Size Distribution on Patch Diameter

Taking a look at the results for the patch diameter d of single patched particles in Tab. 9.1 a relatively broad standard deviation for almost all particle sizes and printing conditions becomes obvious. These errors can raise up to 27 % of the measured patch diameter, which is the case for the 1 µm sample. An important point for the quality assessment of this approach were narrow patch diameter distributions, enabling a way to integrate precise self-assembling conditions. During investigations for possible factors, which could lead to a significant broadening of these error margins, the influence of the particle size distribution was evaluated. This parameter is independent from the used printing procedures and is a naturally occurring condition for synthesized silica particles. Therefore, it is possible that the influence will be dependent on the used synthesis route or particle batch.

For this purpose mathematical calculations based on simplified assumptions were conducted. The goal was to receive an initial impression of the overall impact of this factor.

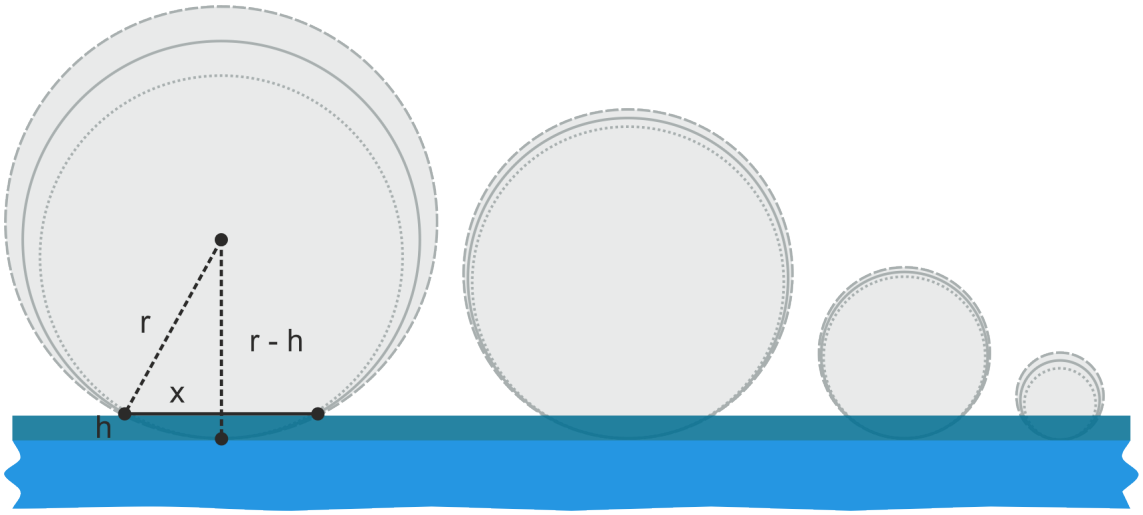

Figure 5.1 Schematic illustration of the influence of particle size distribution on the patch diameter. Four particle sizes (solid line) used in this research, $(5.06 \pm 0.44)\,\mu m$, $(4.08 \pm 0.11)\,\mu m$, $(2.12 \pm 0.06)\,\mu m$ and $(1.01 \pm 0.10)\,\mu m$, are depicted inside a thick ink film, with upper (striped line) and lower (dotted line) size distribution limit. Given variables are particle radius r, ink film thickness h and half patch diameter x.

Fig. 5.1 illustrates the thoughts behind this approach and the necessary variables. The sketch shows four particle sizes embedded inside a thick ink layer, as it would be the case during microcontact printing. Additionally, the upper (striped line) and lower (dotted line) particle size distribution limit is highlighted. All drawn particles sizes are placed on top of the PDMS stamp. This instance already demonstrates the three important and very simplified assumptions used in this calculations:

1. Particles are penetrating the ink layer completely, reaching the PDMS stamp.
2. Ink surface is not disturbed and the layer is not moved during this process.
3. No bending of the PDMS stamp.

All points are obviously a strong simplification of the actual occurring process during printing. Bending of the PDMS surface is more than likely and the ink layer will somehow be deformed by the penetrating particles. Still, the goal at this point is not to give a precise prediction of the achievable patch diameter, as this needs a much more demanding mathematical construct. The influence of the particle size distribution should be obtained. Therefore, these assumptions are an immense assistance for keeping the calculations simple, but meaningful results can be achieved. The diagrams displayed in Fig. 5.2 show the calculated results. For explanation: The theoretical patch diameter is plotted against the PEI film thickness for every particle batch with its corresponding particle size distribution.

In all diagrams the PEI thickness associated with the PEI concentration used for printing is highlighted at single points on the resulting graph (e.g. two used PEI concentrations for the 2 µm particles). First, the theoretical diameter was calculated for the mean particle size. Afterwards, the upper and lower particle size was applied and the resulting data is plotted as red areas surrounding the mean values. With these data points, the resulting theoretical error margin e_x describing this influence for every particle size was calculated and can be found in Tab. 5.1. A detailed description of the used calculations can be found in section 8.4.2.

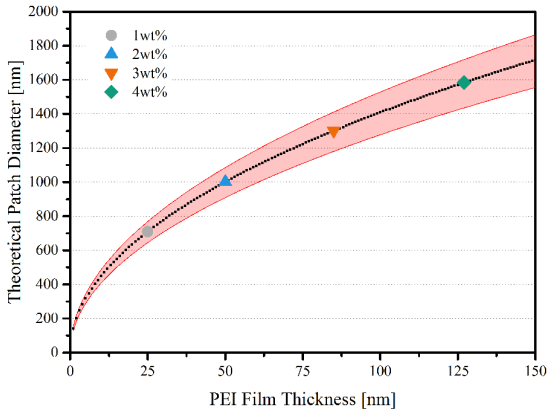

(a) Calculations for (5.06 ± 0.44) µm particles

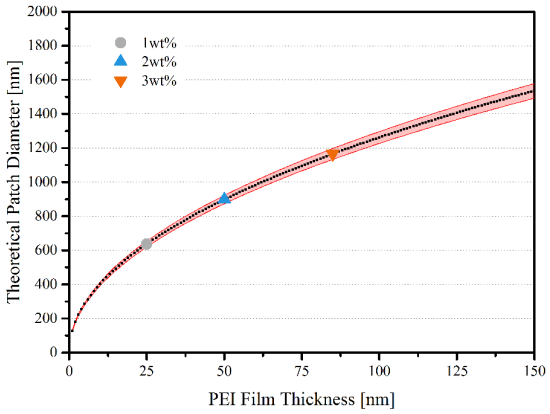

(b) Calculations for (4.08 ± 0.11) µm particles

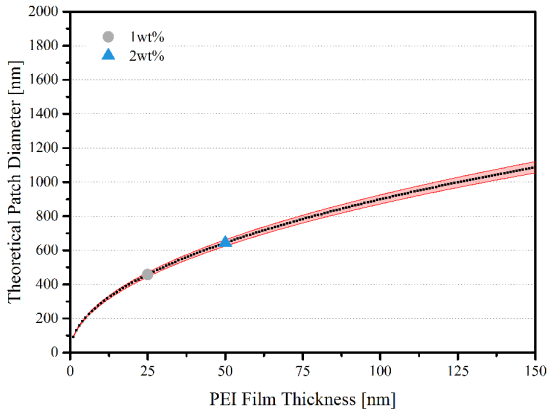

(c) Calculations for (2.12 ± 0.06) µm particles

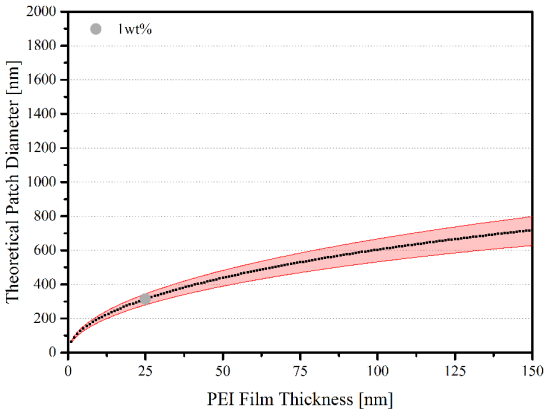

(d) Calculations for (1.01 ± 0.10) µm particles

Figure 5.2 Theoretical patch diameter as a function of the ink film thickness for all particles. Red areas highlight influence of the particle size distribution on the patch diameter. Film thicknesses corresponding to the polymer solutions used experimentally are highlighted in different colours.

The graphs nicely describe the increasing influence of the particle size distribution on the absolute patch diameters with increasing film thickness. Furthermore, a clear distinction between the used particle batches is visible. For example, the calculated influence for the used (5.06 ± 0.44) µm particles is considerably larger in comparison to the (4.08 ± 0.11) µm

Table 5.1 Theoretical calculated error e_x describing the influence of the particle size distribution for different particles sizes on the patch diameter, which was obtained using a simplified mathematical calculation.

PEI [wt%]	$e_{5.06\,\mu m}$	$e_{4.08\,\mu m}$	$e_{2.12\,\mu m}$	$e_{1.01\,\mu m}$
1	0.13 µm	0.04 µm	0.03 µm	0.07 µm
2	0.18 µm	0.08 µm	0.04 µm	
3	0.23 µm	0.12 µm		
4	0.28 µm			
1	59 %	23 %	20 %	88 %
2	62 %	40 %	27 %	
3	74 %	48 %		
4	88 %			

sample as a result of the varying size distribution. In the case of the $(1.01 \pm 0.10)\,\mu m$ sample, the absolute values describing the influence reach higher numbers in comparison to the 2 µm silica particles. This influence depends strongly on the used particles or the synthesis route. Generally, it is more difficult to produce monodisperse silica particles at larger size ($> 1\,\mu m$) in comparison to smaller spheres. The achieved results in Tab. 5.1 are displayed as absolute values and as percentage of the experimentally measured error margin. All results indicate a feasible and significant influence reaching from 20 % to 88 %.

With these findings, the achieved printing quality has to be discussed anew. As the broadening of experimentally obtained patch diameter is, too a significant degree, not the outcome of the actual printing process, but a result of polydisperse particles. The precision of this new approach is clearly higher than initial results would indicate. Especially considering the harsh simplification used for this evaluation. Bending and deformation of the ink layer will certainly increase this effect even further. Furthermore, this evaluation could reveal another important parameter, which was not discussed until this point: Particle surface anomaly due to particle history or differences in the synthesis route. Results show that a large part of the visualized broadening of $d_{5\,\mu m}$ is due to particle polydispersity. In contrast the error margin for $d_{2\,\mu m}$ seems to originate only to small portion from this effect. Still, these particles show a considerable patch diameter distribution. The 2 µm sample was the only purchased silica particle batch delivered dispersed in water and not in dry state. Additionally, due to its narrow size distribution, a further adaptation of

a classical silica synthesis procedure using surfactants could be possible.[121,124,125] This addition on the other hand could lead to disadvantages during the printing process, which would manifest in the measured broadening of d. This connection becomes even more plausible considering that the particle samples with the highest calculated e_x values, due to polydispersity (5 µm & 1 µm), are purchased from the same supplier and both samples do not show stronger additional broadening of d. This indication makes the necessity of precise particle surface composition and its influence during microcontact printing obvious. Further results concerning this effect should be greatly considered to increase reproducibility of this approach and gain a higher comparability between different particle batches.

5.2 Variations of Printing Pressure for Different Particle Sizes

One of the important selection criteria for the usage of polymeric ink in contrast to molecular inks, was the ability to adjust patch parameters (d, t, etc.) at a constant printing force. This feature would increase the flexibility of this approach considerable, especially in view of possible up-scaling procedures. Nevertheless, it is evident that during the printing of micrometer scaled objects even a slight mismatch could lead to significant variations during printing. As described in detail in section 3.3.2 the measured patch thickness t showed a decreasing trend for smaller particles. As all printing conditions were kept constant, the only differentiating parameter was the used particle size. Therefore, investigations concerning the particle size and the resulting patch thickness were conducted, leading to an evaluation of pressures during microcontact printing.

Using silica spheres with varying sizes led to the build-up of particle monolayers with a different packing densities. The illustrations in Fig. 5.3 show the two-dimensional projection of hexagonal densely packed particle monolayers for the used particle sizes. The displayed section has a edge length of 20 µm. All particles exhibit a smaller blue circle, indicating the contact area of the particle surface and the underlying ink layer. For the calculation of this contact area, the assumptions used in section 5.1 were applied. The idea behind this calculations was to obtain a printing pressure for a microcontact printing approach using a 1 x 1 cm^2 substrate while changing the particle size and therefore the achieved contact area. Again, no bending of the PDMS stamp was included. However, as this assumption is true for all four calculations, the systematic error is neglectable for a comparative analysis. A detailed description of the used calculations can be found in

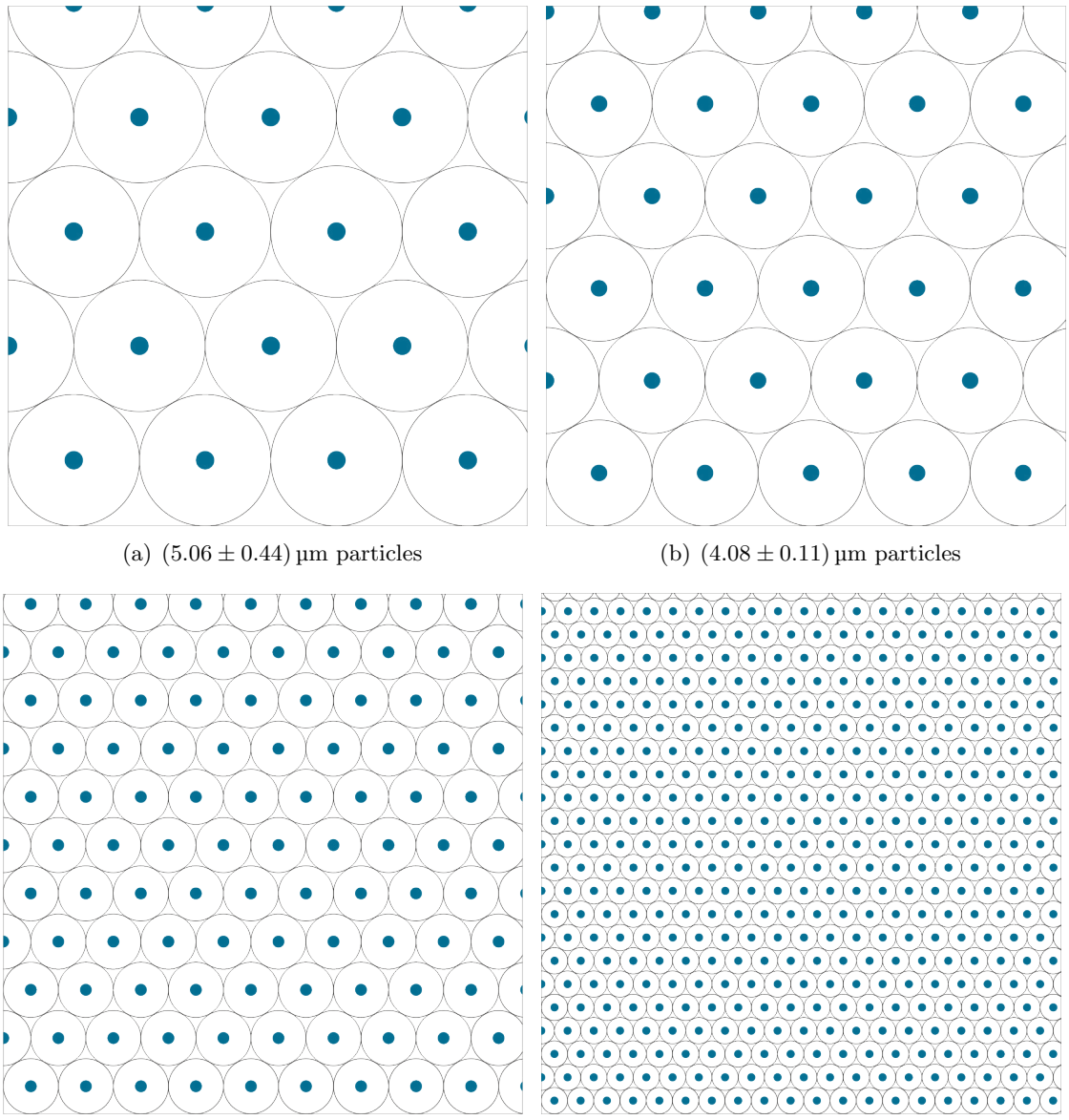

(a) (5.06 ± 0.44) µm particles

(b) (4.08 ± 0.11) µm particles

(c) (2.12 ± 0.06) µm particles

(d) (1.01 ± 0.10) µm particles

Figure 5.3 Illustrations show the monolayer packing of different particle sizes and the blue contact area between the particle surface and the underlying ink film.

section 8.4.3. A significant increase of the contact area for smaller particles is already visible from the shown sketch. Therefore, as the applied printing force is comparable for all printing experiments (compare section 9.4), a decreasing printing pressure for smaller particles was expected. The calculated results are shown in Tab. 5.2 as absolute and relative values scaled to the 5 µm sample. An almost linear decreasing trend is visible for the used spheres. This would certainly confirm the experimentally obtained data, showing thinner patches for smaller particles. The particles will not be embedded as deeply into the ink layer as the comparable 5 µm sample, due to decreasing printing pressure for the individual particle with decreasing sphere sizes.

Several simplification have been made to obtain this evaluation, including no bending of PDMS, perfect monodisperse particle and no deformation or squeezing of the ink layer. Due to these simplifications, the obtained results, especially the absolute values, should be considered with caution. Still, a clear decreasing trend for the printing pressure, which explains the experimentally measured results, was constructed. In respect to comparable conditions between all printing experiments, this effect should be taken into account. However, for the precise tuning of the applied force to counteract this effect, a specialized instrument would have been needed. The following section will introduce an initial attempt to enable precise pressure control.

Table 5.2 Calculated absolute and relative printing pressures for used particle sizes.

Sample	5.06 µm	4.08 µm	2.12 µm	1.01 µm
Pressure	889 kPa	718 kPa	375 kPa	181 kPa
Rel. Pressure	100 %	81 %	42 %	20 %

5.3 Pressure Control using Centrifugal Force[†]

Until this point, all presented results in chapter 3 and 4 were exclusively produced by hand, meaning that no mechanical device was used to improve the alignment or pressure control during microcontact printing. This point alone is a statement for the simplicity of this approach and how the adjustment of the polymer ink layer on the stamps is able to finely tune the achieved patch geometry. Nevertheless, as the previous section 5.2 and its calculation showed, there is obviously a connection between the used particle size, the applied printing force and the resulting printing pressure of the individual particle. In an effort to enhance the pressure control during printing, as well as the parallel alignment of the particle monolayer in respect to the loaded PDMS stamp, a new and innovative design for microcontact printing using centrifugal forces was developed. The structure of this advancement will be described briefly in the following section, as well as initial printing results obtained by this approach.

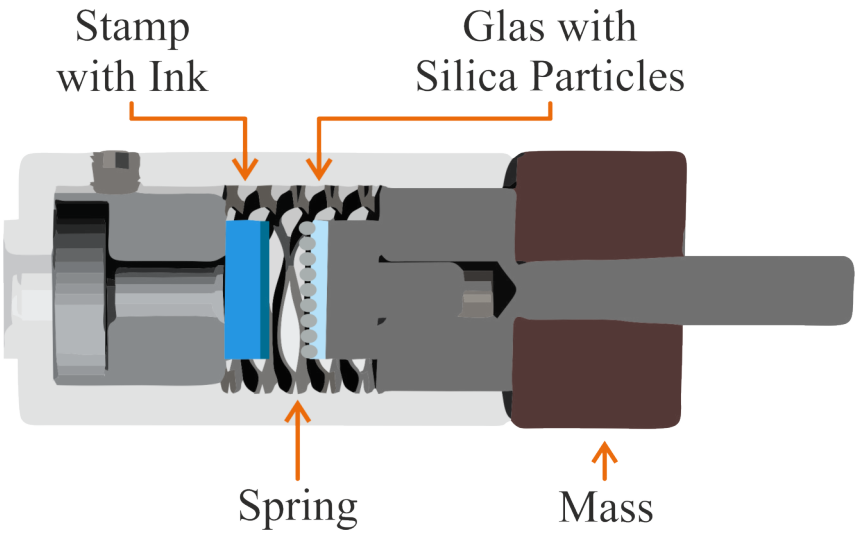

Figure 5.4 Schematic of the inside of the developed centrifuge chamber for microcontact printing of single patched particles.

The idea was to utilize the rotor of an analytical centrifuge (*LUMiFrac*) to apply centrifugal forces onto the used printing substrates. By careful adjustment of the rotation speed of the rotor, precise tuning of the printing force should be achieved. For this purpose new centrifuge chambers had to be planed and constructed, whom would fulfil the necessary specifications. Fig. 5.4 illustrates the rough design of these novel chambers. On the right hand side of the chamber, the glass substrate with the applied silica particle monolayer is

[†]The development and construction of the used centrifuge set-up was conducted with the help of Uwe Rietz and Prof. Dr. Dietmar Lerche from *LUM GmbH* located in Berlin-Adlershof.

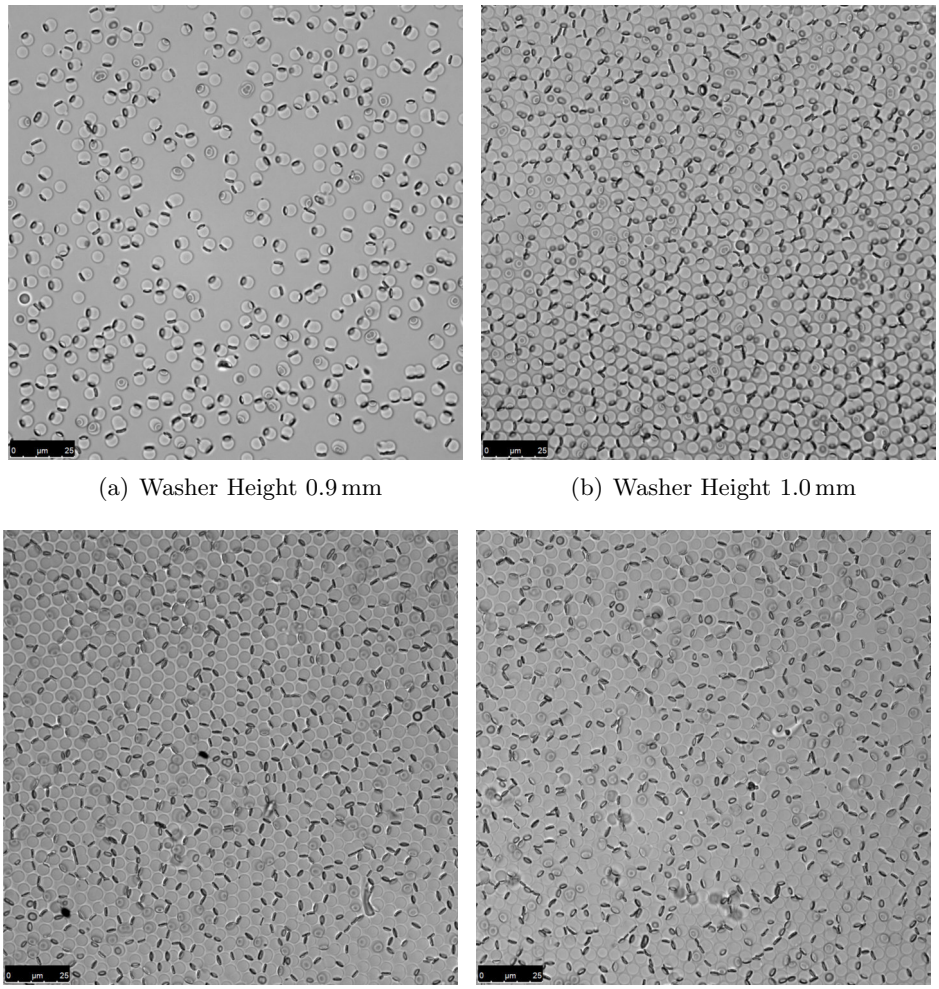

(a) Washer Height 0.9 mm (b) Washer Height 1.0 mm

(c) Washer Height 1.1 mm (d) Washer Height 1.2 mm

Figure 5.5 Light microscope images show single patched particles printed inside the centrifuge chamber. Higher printing pressures were realized using thicker flat washer.

fixed onto a moveable slide connected to a weight. On the left hand side the corresponding loaded PDMS stamp is mounted onto an immobile sample holder. Both substrates are fixated using strong adhesive tapes, which are able to hold the substrates during the centrifuge printing process. Stamp and particle monolayer are separated by a fine wave spring. This spring was installed to obtain an automatic detachment of the two substrates after the printing process. At the start of the experiment the spring separates the two substrates. By increasing the rotation speed the weight will be pressed to the outside of the chamber (movement to the left of displayed illustration). During this process, the weight will work against the spring until the two substrates are connected and the weight touches the inner metallic cylinder. During this event a signal will be send to the centrifuge software to confirm successful contact of the substrates. The exact distance between the substrates and therefore the applied pressure was adjusted using very thin washers, which are installed

under the relevant substrates. After contact, the rotation speed will be decreased slowly, while the wave spring is able to detach the printing substrates carefully. With this set-up, a gentle printing procedure with very good parallel alignment and pressure control is possible. The *LUMiFrac* is able to hold eight distinct chambers to conduct simultaneous printing experiments under various conditions (i.e. different washer selection.)

Table 5.3 The patch yield, diameter and thickness (Y, D, t) for 5 µm 3D single patched particles Y_{SPP} obtained by centrifuge printing at different printing pressures.

PEI [wt%]	$Y_{0.9\,mm}$	$Y_{1.0\,mm}$	$Y_{1.1\,mm}$	$Y_{1.2\,mm}$
3	95 %	92 %	80 %	78 %
PEI [wt%]	$d_{0.9\,mm}$	$d_{1.0\,mm}$	$d_{1.1\,mm}$	$d_{1.2\,mm}$
3	(2.99 ± 0.23) µm	(2.69 ± 0.24) µm	(3.01 ± 0.20) µm	(3.2 ± 2.0) µm
PEI [wt%]	$t_{0.9\,mm}$	$t_{1.0\,mm}$	$t_{1.1\,mm}$	$t_{1.2\,mm}$
3	(74 ± 3) nm	(87 ± 5) nm	(83 ± 4) nm	(82 ± 6) nm

For initial test experiments 5 µm silica particles were printed using a 3 wt% PEI film. Due to steric reasons, circular glass slides and PDMS stamps were produced, but otherwise equal preparation conditions for the printing process were used. Starting with four different washer settings with a thickness of 0.9 mm. 1.0 mm, 1.1 mm and 1.2 mm first experiments were conducted. The washer thicknesses of 0.9 mm translates into almost no contact between the substrates, while 1.0 mm gives a complete contact of stamp and particle monolayer. Thicker washer settings were used to further increase the pressure during printing. The resulting single patched particles are displayed on the microscope images in Fig. 5.5. The pictures for all washer settings show a remarkable concentration of printed particles with very distinct patches. These findings are without a doubt the best printing results obtained during this research. The patch yield for all samples was calculated and the numbers are displayed in Tab. 5.3. Due to the high concentration of printed particles, between 400 and 1500 particles could be counted for this calculation. Especially the first two washer settings show almost perfect values of up to 92 % to 95 %. For the observable particles without printed patch it is highly likely, that they are missing due to rotational mismatch with the microscope focusing plane, meaning the patch side is directed away from the microscope camera. Higher pressure settings show a drop of patch yields to 80 % and 78 %, respectively.

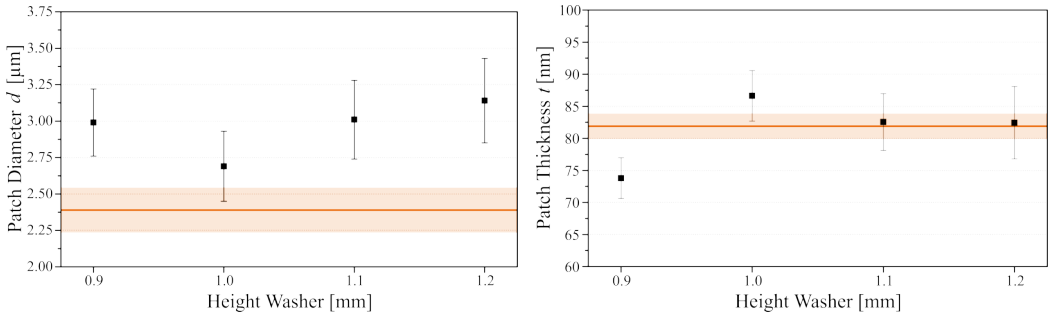

(a) Patch Diameter (b) Patch Thickness

Figure 5.6 Diagrams show the patch diameter and thickness results for all printing pressures tested inside the centrifuge chamber. Orange line and area represent the corresponding result with error margin obtained by hand printing for same printing conditions.

The next calculated results were the average patch diameter d for all washer settings. The received values are displayed in Fig. 5.6 and Tab. 5.3. Starting from the 1.0 mm setting, a continuous rise of the achieved patch diameter is visible. This behaviour is understandable as an increasing pressure leads to a stronger penetration of the PEI layer. Additionally, at higher forces the polymeric film will be squeezed from under the particle, increasing the patch diameter in the process. The plotted orange line with its surrounding area shows the corresponding d value with error margin obtained by hand printing. Its mean value lies slightly below the 1.0 mm washer setting, indicating a higher pressure during centrifuge printing. However, the achieved d value for the first sample appears out of place. It reaches a value comparable to the second highest pressure used in this experiment, which is not in accordance with the explained printing pressure theory. Examining the measured patch thickness values in Fig. 5.6 and Tab. 5.3 give a possible explanation. Again, starting from the 1.0 mm setting, a continuous but very low decrease ($\pm$ 5 nm) of the t value is observable for increasing printing pressure. As stated above, the PEI layer around the silica particle will be deformed or even compressed under printing forces. Therefore, a reduced patch thickness caused by higher printing force becomes comprehensive. Still, the variation is almost not significant given the error range. That holds also true for the comparison with *by-hand* experiments. The corresponding values lies within the newly achieved thicknesses. In contrast to this result, the 0.9 mm sample exhibits the lowest measured printing pressure. The here proposed hypothesis for the unusual printing results are, that the particles are only partially in contact with the PEI layer, leading to a very low patch thickness after particle release. However, the particles are able to remove a broad area of the top PEI layer during this process, leading to strong increase in patch diameter. Another point

could be the missing deformation and compression of the PEI film in contrast to the other achieved results. If the patch is not compressed under this low pressure, the polymer chains could possibly swell to a higher degree during microscopic imaging in ethanol, simulating a generally larger patch geometry. Both explanations are difficult to verify, but should be given here as considerations. The previously addressed drop in patch yield for increased washer settings was partially explained during the measurement of the patch thickness via AFM on the dried PDMS stamps. AFM images of these stamps can be found in the appendix section 9.2.3 (compare Fig. 9.8). The created holes in the PEI film normally produced during particle release in acetone show additional, very deep indentations. These grooves are most likely the results of silica particles being pressed into the PDMS stamps due to very high pressure. An exemplary topographical presentation of the different stamps is given in Fig. 5.7. The first diagram displays a hole, which only represents the missing PEI on top of the PDMS surface, whereas the second shows a deep crack as the result of the penetrating silica particle. This effect will most likely destroy the underlying polymeric ink film and therefore reduce the achieved patch yield.

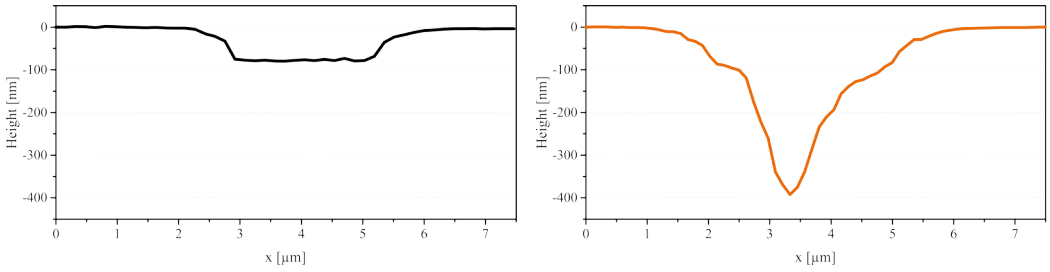

(a) Washer Height 1.0 mm (b) Washer Height 1.2 mm

Figure 5.7 Diagrams show the topographic difference between holes in the PDMS stamp after particle release for different washer settings. Increased pressure due to a 1.2 mm washer thickness leads to rupture of the PDMS stamp under the PEI layer (b).

As a conclusion for the obtained results of this new approach, two important points have to be mentioned: First a remarkable patch yield could be achieved, most likely due to the precise alignment of particle monolayer and PDMS stamp. The two lowest printing pressures even showed full conversion under these conditions. Second, the achieved quality of the patch geometry investigated by fluorescence microscopy is clearly excellent. Unfortunately, this process does not possess a high up-scaling capability for future applications like other methods (e.g. roll-to-roll). Nevertheless, for the moment it sets a benchmark as a production instrument for microcontact printing of silica particles with polyelectrolyte ink.

CHAPTER 6

Conclusion

This research addressed the question, if it is possible to simplify current microcontact printing systems for the production of anisotropic building blocks or patchy particles, by using common chemicals while still maintaining reproducibility, high precision and tunability of the Janus-balance.

Chapter 2 introduced the microcontact printing materials as well as their defined electrostatic interactions. In particular polydimethylsiloxane stamps, silica particles and high molecular weight polyethylenimine ink were mainly used in this research. All of these components are commercially available in large quantities and affordable, which gives this approach a huge potential for further up-scaling developments. The benefits of polymeric over molecular inks was described including its flexible influence on the printing pressure. With this alteration of the μCP concept, a new method of solvent assisted particle release mechanism enabled the switch from two-dimensional surface modification to three-dimensional structure printing on colloidal silica particles, without changing printing parameters or starting materials. This effect opened the way to use the internal volume of the achieved patches for incorporation of nano additives, introducing additional physical properties into the patches without alteration of the surface chemistry.

The success of this system and its achievable range was further investigated in chapter 3 by giving detailed information about patch geometry parameters including diameter, thickness and yield. For this purpose, silica particles in a size range between 1 µm and 5 µm were printed with different ink concentrations to change the Janus-balance of these single patched particles. A necessary intermediate step, consisting of air-plasma treatment, for the production of trivalent particles using ,,sandwich" printing was discovered and comparative studies concerning the patch geometry of single and double patched particles

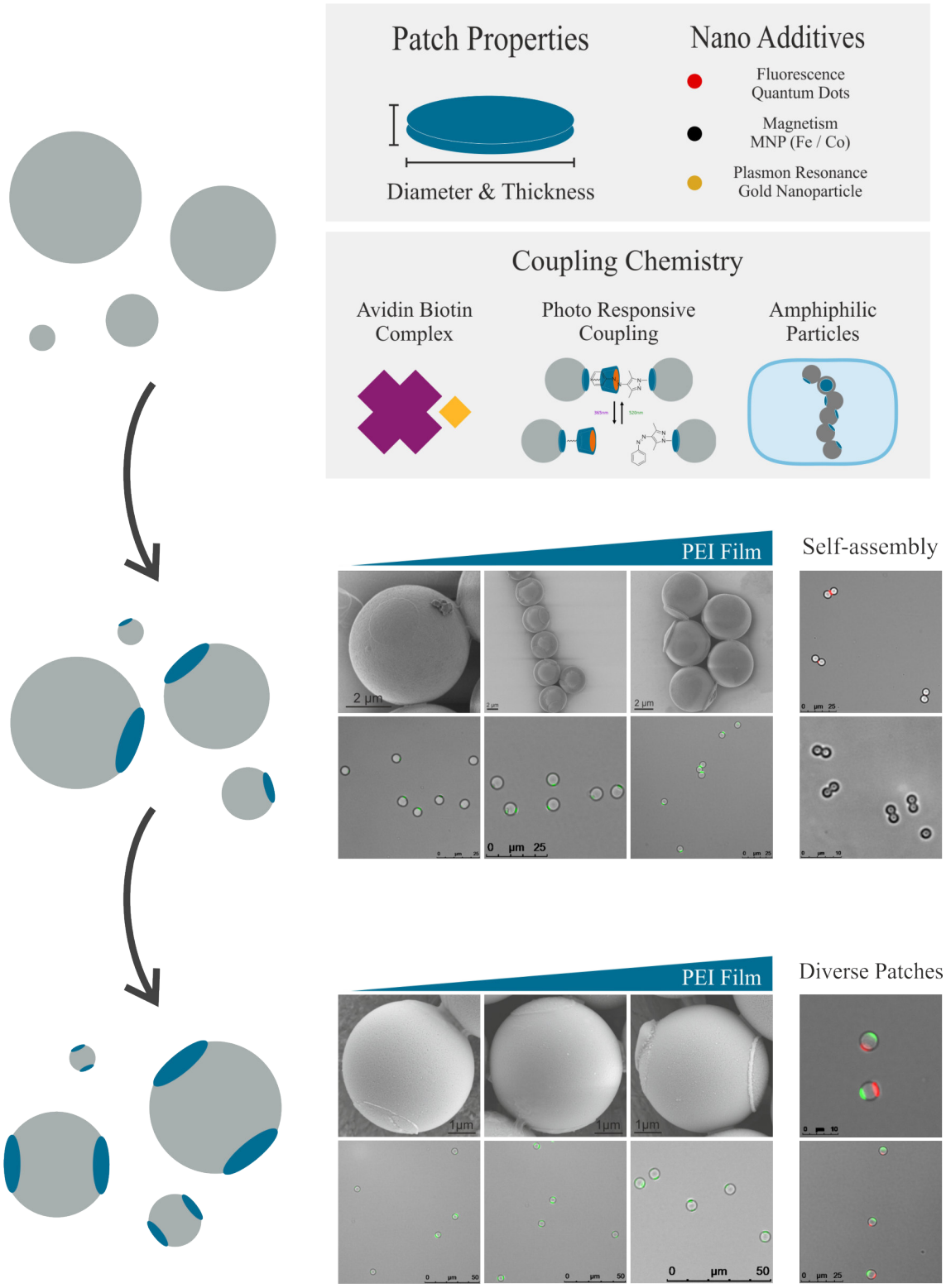

Figure 6.1 This schematic summarizes roughly the achieved results. Starting with the precise control over patch properties like diameter and thickness and the ability of incorporation of nano additives for additional physical properties. Furthermore the researched coupling systems are presented aiming for self-assembly of particle dimers. A small selection of exemplary FM and SEM images for single and double patched particles is presented.

were conducted. Additionally, the usage of structured PDMS stamps during printing was described. These results demonstrate the excellent precision of this approach and opens the pathway for even greater accuracy as further parameters can be finely tuned and investigated, e.g. humidity and temperature during stamp loading.

The performance of these synthesized anisotropic colloids was further investigated in chapter 4, starting with behaviour studies in alcoholic and aqueous dispersions. Here, the stability of the applied patches was studied in a broad pH range, discovering a release mechanism by disabling the electrostatic bonding between particle surface and polyelectrolyte ink. Furthermore, the absence of strong attractive forces between divalent particles in water was investigated using XPS measurements. These results lead to the conclusion that the transfer of small PDMS oligomers onto the patch surface is shielding charges, preventing colloidal agglomeration. However, based on this knowledge, further patch modifications for particle self-assembly were introduced including physical approaches using magnetic nano additives, chemical patch functionalization with avidin-biotin or the light responsive cyclodextrin-arylazopyrazoles coupling as well as particle surface modification for the synthesis of highly amphiphilic colloids. The successful coupling, its efficiency, stability and behaviour in different solvents were evaluated to find a suitable coupling system for future assembly experiments. Based on these results the possibility of more sophisticated structures by colloidal self-assembly is given.

Certain findings needed further analysis to understand their underlying mechanics, including the relatively broad patch diameter distribution and the decreasing patch thickness for smaller silica particles. Mathematical assumptions for both effects are introduced in chapter 5. First, they demonstrate the connection between the naturally occurring particle size distribution and the broadening of the patch diameter, indicating an even higher precision for this μCP approach. Second, explaining the increase of contact area between particle and ink surface due to higher particle packaging, leading to a decrease in printing pressure for smaller particles.

These calculations ultimately lead to the development of a new mechanical micro-contact printing approach, using centrifugal forces for high pressure control and excellent parallel alignment of printing substrates. First results with this device and the comparison with previously conducted by-hand experiments conclude this research. It furthermore displays the advantages of such a device for future applications using a mechanical printing

approach, especially for accessing even smaller nano particles with great precision and excellent yield.

In conclusion, this work demonstrates the successful adjustment of the μCP approach using commercially available and affordable silica particles and polyelectrolytes for high flexibility, reduced costs and higher scale-up value. Furthermore, its was possible to increase the modification potential by introducing three-dimensional patches for additional functionalization volume. While keeping a high colloidal stability, different coupling systems showed the self-assembly capabilities of this toolbox for anisotropic particles.

CHAPTER 7

Zusammenfassung

Diese Forschungsarbeit befasste sich mit der Frage, ob es möglich ist, bekannte Mikrokontaktdruckverfahren, zur Herstellung von anisotropen Bausteinen (*Patchy Particles*), weiter zu vereinfachen. Dabei sollten gängige Chemikalien verwendet werden ohne einen Verlust in Reproduzierbarkeit, hoher Präzision und Feineinstellung der Janus-Balance zu erleiden.

In Kapitel 2 wurden die verwendeten Mikrokontaktdruckmaterialien sowie deren elektrostatische Wechselwirkungen vorgestellt. Insbesondere handelte es sich dabei um Polydimethylsiloxan Stempel, Silikapartikel und hoch molekulare Polyethylenimin Tinte. All diese Produkte sind kommerziel in großen und bezahlbaren Mengen erhältlich. Nicht nur die Vorteile von polymeren Tinten im Gegensatz zu molekularen Tinten wurde beschrieben, sondern auch die hohe Flexibilität dieses Verfahrens bezüglich der verwendeten Druckkraft. Mit dieser Anpassung des Mikrokontaktdrucks, wurde eine neue Methode der Lösungsmittel unterstützten Partikelablösung ermöglicht, mit deren Hilfe ein einfaches Schalten zwischen zwei dimensionaler Oberflächenfunktionalisierung und drei dimensionalem Strukturdrucks möglich war, ohne Druckparameter oder Startchemikalien zu verändern. Dadurch konnte neu erschaffenes internes Volumen verwendet werden um Nanoadditive einzuführen und so zusätzliche physikalische Eigenschaften zu integrieren, ohne die Oberflächenchemie der *Patches* verändert wurde.

Der Erfolg dieses Systems und seine erreichbaren Grenzen wurde gründlichst in Kapitel 3 erforscht, indem detaillierte Geometrieparameter der *Patches* einschließlich Durchmesser, Dicke und Ausbeute, erworben wurden. Hierfür wurden Silikapartikel in einem Größenbereich von 1 µm bis 5 µm mit unterschiedlichen Tintenkonzentrationen bedruckt, um Veränderungen erforschen zu können. Ein notwendiger Luftplasma Ätzschritt für die Produktion von trivalenten Partikeln, mit Hilfe des sogenannten „Sandwich“-Drucks, wurde

erläutert und vergleichende Untersuchen von einfach und zweifach modifizierten Bausteinen wurden durchgeführt. Zusätzlich dazu, wurde die Verwendung von strukturierten Stempel beschrieben. Die Ergebnisse verdeutlichen die exzellente Genauigkeit dieser Methode und öffnet den Weg um eine hoch höhere Präzision zu erreichen da weitere Parametere genau eingestellt und untersucht werden können, z.B. Luftfeuchtigkeit und Temperature während der Stempelbeladung.

Die Performance der herstellten anisotropen Partikel wurde in Kapitel 4 mit Verhaltensstudien in alkoholischen und wässrigen Dispersionen getestet. Dabei wurde die Stabilität der Oberflächenfunktionalisierungen in einem breiten pH Bereich untersucht. Dadurch wurde ein Ablösungsmechanismus bei sehr hohen bzw. niedrigen pH-Werten entdeckt, der zur Deaktivierung elektrostatischer Wechselwirkungen zwischen Partikeloberfläche und Polyelektrolyte Tinte führte. Desweitern wurden die Abwesenheit starker Wechselwirkung der divalenten Partikel in Wasser mit Hilfe von XPS untersucht. Das Resultat zeigte, dass der Transfer kleinster PDMS Oligomere auf die Patchoberfläche zu einer Ladungsabschirmung führte. Dadurch konnte Agglomeration verhindert werden. Aufgrund dieser Ergebnisse wurden weitere Modifikationen für Partikelassemblierung durchgeführt. Hierfür wurde die Einführung von magnetischen Nanoadditiven, die Funktionalisierung mit Avidin-Biotin sowie dem Lichtschaltbaren Cyclodextrin-Arylazopyrazol Komplexen und die Partikeloberflächenfunktionalisierung zur Herstellung amphiphiler Teilchen untersucht. Die Effizienz der Kopplung, deren Stabilität sowie das Verhalten in unterschiedlichen Lösungsmittel wurde beschrieben. Basierend of diesen Ergebnissen können noch anspruchsvollere Strukturen durch kolloidale Selbstassemblierung erzeugt werden.

Einige Ergebnisse dieser Arbeit benötigten zusätzlicher Analyse um die zugrundeliegenden Mechaniken verstehen zu können. Dazu gehörte die relative hohe Streuung des Durchmessers für unterschiedliche Partikelsysteme, sowie das Ausdünnen des *Patches* mit kleineren Silikapartikeln. Mathematische Modelle in Kapitel 5 beschreiben beide Effekte. Dadurch war es möglich einen Zusammenhang zwischen der natürlichen Partikelgrößenverteilung sowie der Verbreitung des Patchdurchmessers festzustellen. Des Weitern konnte eine Verkleinerung der Druckkraft durch eine Erhöhung der Packungsdichte für kleine Partikel beschrieben werden, wodurch eine Erklärung der Ausdünnung möglich war.

All diese Berechnung führten schlussendlich zur Entwicklung eines neuen mechanischen Mikrokontaktdruckverfahrens, welches mit Hilfe von Zentrifugalkräften eine hohe Druck-

kontrolle und eine exzellente parallele Ausrichtung zwischen den Substraten ermöglicht. Erste Ergebnisse, sowie deren Vergleich mit bisher erhaltenen Resultaten schließen diese Forschung ab. Des Weiteren zeigt es die Vorteile einer solchen Vorrichtung für kommende Applikationen, besonders um noch kleinere Nanopartikel mit einer hohen Präzision modifizieren zu können.

Zusammenfassend ist zu sagen, dass diese Forschung die erfolgreiche Anpassung des Mikrokontaktdruckverfahrens mit kommerziel erhältlichen und bezahlbaren Silikapartikeln und Polyelektrolyten demonstriert, um hohe Flexibilität, reduzierte Kosten und ein erweitertes Skalierungspotential zu bieten. Zusätzlich ist es gelungen, die Funktionalisierungsdichte zu erhöhen, indem drei dimensionaler Strukturdruck bisher ungenutztes Volumen schaffen konnte. Während eine hohe kolloidale Stabilität erhalten blieb, ist es gelungen unterschiedliche Kopplungssysteme zu nutzen, um das Selbstorganisationspotential dieser Toolbox für anisotrope Partikel aufzuzeigen.

CHAPTER 8

Materials and Methods

This chapter gives data about all utilized chemicals substances and their origin, that is supplier, synthesis route and corresponding literature source where applicable. Furthermore detailed information of all investigated methods is given. Analytical instruments and their application with employed software along with necessary sample preparations are introduced. Finally, all applied calculations are outlined including defined variables.

8.1 Chemicals

Inorganic particles Dry silica particles with a size of (5.06 ± 0.44) µm and (1.01 ± 0.10) µm were purchased from *Bang Laboratories*, with a size of (4.08 ± 0.11) µm from *Cospheric* and particles in aqueous solution with a size of (2.12 ± 0.06) µm from *microparticles*. InP based core-multi-shell quantum dots were provided by the department Functional Materials and Devices of Fraunhofer IAP. The quantum dots consist of an InPZnS hybrid core covered with one monolayer of ZnSe and six monolayers of ZnS shells.[214] The ligand shell consisted of mercaptopropionic acid molecules which were attached to the quantum dot surface via the thiol group. The peak emission wavelength was 618 nm with a full width half maximum of 68 nm. The quantum yield of the quantum dots was 34%. Superparamagnetic dextran nanoparticles consisting of 55 to 85 wt% of iron oxide in a matrix of dextran (40 000 Da) with a size of 20 nm were purchased from *micromod*. Gold nanoparticles with a size of (25 ± 10) nm were synthesized by reduction of gold(III) chloride trihydrate (*Sigma Aldrich*) with sodium citrate (*Sigma Aldrich*).[215]

Stamp Material and Inks Poly(dimethylsiloxane) (PDMS) stamps were prepared from the Sylgard 184 elastomer kit obtained from *Dow Corning* as described in the methods section below. Aqueous solutions (50 wt%) of linear and branched polyethylenimine

(L/BPEI) were purchased from *Fluka Chemicals* and *Sigma Aldrich*, respectively with a molecular weight distribution of 600 to 1000 kg mol^{-1} for both polyelectrolytes. An aqueous solution of polyacrylic acid (PAA) with a concentration of 45 wt% and a molecular weight of 8000 g mol^{-1} was acquired from *Sigma Aldrich*.

Particle and Patch Functionalization 3-Aminopropyltriethoxysilane (APTES) and octyltriethoxysilane (OTES) were purchased from *abcr GmbH*. Fluorescein isothiocyanate (FITC) was obtained from *Sigma Aldrich*. Salt free avidin was purchased from *Thermo Scientific* and biotin from *Applichem*. N-(3-Dimethylaminopropyl)-N'-ethylcarbodiimide hydrochloride (EDC·HCl) from *Fluka* and N-Hydroxysuccinimide (NHS) from *Sigma Aldrich* were used. Arylazopyrazoles and cylclodextrin functionalized with carboxy groups were kindly provided by Sven Sagebiel from WWU Münster.[64,211] Cysteamine was purchased from *Sigma Aldrich*.

Solvents Ethanol was purchased from *Th. Geyer* (reinst), acetone from *VWR* (ACS reagent) and Dimethylsulfoxid (DMSO) from *Merck* (ACS grade). Milli-Q water (Typ 1, 18.2 MΩ cm) was purified using a Milli-Q Reference water purification system from *Merck* with a Biopak Polisher.

Consumables & Miscellaneous Microscope slides (Superfrost, 90°) and cover slides (20 x 20 mm^2 and 24 x 60 mm^2) were purchased from *Carl Roth*. For long time experiments a Chambered #1.5 German Coverglass system with eight wells was used from the company *Tek-Lab*. As microscope oil the Type F immersion liquid ($n_r = 1.56$) from *Leica* was used. Neodymium magnets with a size of 80 x 80 x 20 mm^3 and a traction force of 400 kg were purchased from *magnetportal.de*. The homobifunctional epoxy-crosslinker Poly(ethylene glycol) diglycidyl ether (2000 g mol^{-1}) was purchased from *Sigma Aldrich*. Silica wafer (Orientation 100, p-type boron) were purchased from *CrysTec*.

8.2 Methods

8.2.1 Synthesis of PDMS Stamps

Poly(dimethylsiloxane) (PDMS) was synthesized on the basis of a commercial available elastomer kit, which consists of monomer and curing agent. To produce flat PDMS stamps 36.3 g of a 10:1 mixture of monomer and curing agent was poured into a clean, plane square polystyrene Petri dish (side length 12 cm) to obtain a 3 mm thick film. The mixture was degassed over night under ambient conditions. During this time all enclosed air bubbles ascend from the bulk material and the film was cured for 2 h at 80 °C. The crosslinked PDMS was cut into 1 x 1 cm^2 pieces or punched out in circular form with a diameter of 1 cm for further use. To further improve the surface properties and roughness of the PDMS stamps a second approach was conducted. A piece of silicon wafer (8 x 8 cm^2) was cleaned using a CO_2 snow-jet.[216] For this the silicon wafer was fixated using vacuum on a hotplate heated to 200 °C. Possible soiling was removed afterwards by a high pressure stream of accelerated dry-ice, which was produced by gaseous carbon dioxide passing through an narrow orifice. With this procedure larger particles were sling away due to the high velocity of the carbon dioxide stream. Furthermore carbon dioxide is a good solvent for various nonpolar organic chemicals, giving it the ability to remove even remains of organic solvent. The silicon surface was activated using air plasma treatment (60 s, 300 W, 0.2 mbar, PlasmaFlecto 10) to increase the amount of active surface groups. Finally the silicon wafer was brought into a desiccator with a reservoir containing 1 mL n-octyltriethoxysilane (OTES) and a vacuum of 0.2 mbar was applied for 30 min. After this the desiccator was closed and the silanization process run for 24 h. The wafer was removed from the desiccator and rinsed thoroughly with ethanol. The modified silicon wafer surface served as a new interface for the synthesis of exceptional flat PDMS stamps. For this the synthesis as described above was repeated using the silicon wafer as a bottom piece to produce a replica. Due to the hydrophilic modification of the silica wafer the PDMS was removable after curing without any residues.

Preparation of Wrinkled Stamps

For the production of wrinkled substrates from PDMS stamp a clamping device was used. PDMS stamp with a size of 1 x 2.5 cm^2 were cut and mounted onto the clamping device.

Subsequently the stamp was stretched to 130 % of its own length while using air plasma treatment (1 to 60 s, 100 to 300 W, 0.05 to 0.2 mbar, PlasmaFlecto 10). After this, the PDMS stamp was released slowly and carefully, to obtain the wrinkled surface stamps.[87]

8.2.2 Silica Particle Monolayer

Silica particles were dispersed in ethanol at different concentrations (see Tab. 8.1), using an ultrasonic bath for 10 min (37 kHz, Elmasonic P). Microscope slides (VWR) were cut into 1 x 1 cm^2 pieces, cleaned with ethanol, dried under nitrogen and activated using air plasma treatment (60 s, 300 W, 0.2 mbar, PlasmaFlecto 10). Monolayers were obtained by drop casting 3 µL of particle dispersion onto the glass substrates. Possible multilayer buildups were removed during additional µCP steps. For the microcontact printing processes in the centrifuge chamber, circular cover glasses with a diameter of 1 cm were used as a substrate to produce particle monolayers.

Table 8.1 Silica particle sizes with corresponding ethanol solution concentrations for the preparation of particle monolayers on glass substrates.

Particle Size	5.06 µm	4.08 µm	2.12 µm	1.01 µm
Concentration	4 wt%	3 wt%	2 wt%	1 wt%

8.2.3 Polyelectrolyte Ink Films and Loading of Stamp Material

The purchased PEI solution was diluted with Milli-Q water to obtain the desired concentrations of 1, 2, 3 and 4 wt%. Other polymeric inks were diluted or formulated accordingly. The surface of flat PDMS stamps was activated using air plasma treatment (60 s, 300 W, 0.2 mbar, PlasmaFlecto 10). The activated PDMS stamps were loaded with polymer ink by spin coating 60 µL ink solution of the desired concentration (60 s at 4000 rpm / Laurell WS-650-23B). No further precautions, except storing them in a dust free container, were conducted until usage for printing. For measuring the film thickness of these samples cleaned silica wafer pieces with a size of 1 x 1 cm^2 were used as substrate. After spin coating of the polymeric ink, the film was scratch using a cannula tip and the height profile was measured using atomic force microscopy.

Incorporation of Nano Additives To achieve additional physical properties inside the patches nano additives were incorporated. For example 1 wt% of quantum dots were

added to the polymeric ink solution (with respect to the polymer weight) prior to spin coating to achieve fluorescent patches. Other research included superparamagnetic iron oxide and gold nanoparticle, where similar nano additive concentrations were used. For the incorporation of quantum dots into anionic inks (e.g. PAA) a ligand exchange with the positive cysteamine was conducted.[217]

8.2.4 Microcontact Printing

Single Patched Particles The fabrication of SPP with 2D or 3D patches was conducted as follows: A silica particle monolayer on a glass substrate was fixated horizontally using a vacuum sample holder. A PDMS stamp loaded the polymeric ink film was brought into contact with the particle monolayer and pressure was applied (approx. 1.3×10^4 Pa, see Fig. 9.14). During separation process of the stamp and glass substrate, particles were embedded into the ink film and were removed with the PDMS substrate. The particle loaded stamp was immersed into 2 mL of solvent, choosing ethanol for 2D and acetone for 3D patches, and the particles were released using an ultrasonic bath (37 kHz, Elmasonic P). Due to the different solubilities of the polymeric inks in the chosen solvent, time needed for particle release was changed from 10 to 25 min for ethanol and acetone, respectively. Single patched particles with 2D or 3D patches were collected and concentrated for further applications using centrifugation.

Double Patched Particles For synthesis of DPP the PDMS stamp after the first printing step, holding the embedded particles, was etched using air plasma treatment (60 s, 300 W, 0.2 mbar, PlasmaFlecto 10) after the separation step. A second printing step was conducted with a new loaded PDMS stamp. After the separation of the two PDMS substrates, only the second stamp was used for particle release and further treatment to ensure a high yield of fully functionalized particles. Solvent assisted particle release was conducted as described above.

8.2.5 Patch and Particle Functionalization

Silica Particle Modification using Silanes For the surface modification of silica particles, 20 mg of any sphere size were dispersed carefully in 5 mL of concentrated hydrochloric acid (HCl). Afterwards the dispersion was boiled for 5 h to activate the particle surface for further functionalization. The particles were washed thoroughly in water (3x) and ethanol

(3x) using centrifugation and redispersion. For the modification using triethoxysilanes, the particles were dispersed in 5 mL ethanol, stirred rigorously and 100 µL of the respective silane were added (e.g. APTES). After reacting over night, the particles were washed in ethanol (3x) to remove excess silane residues and stored in ethanol for further use.

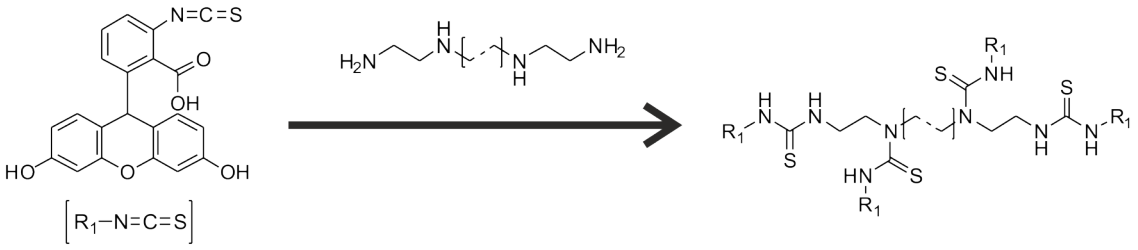

Figure 8.1 The reaction scheme illustrated here shows the exemplary coupling between fluorescein isothiocyanate (FITC) and linear PEI. The reaction was conducted in ethanol at ambient conditions.[218–220]

Fluorescence Labelling of Patches Fluorescent labelling of patchy particles for microscopy was conducted as follows: A sample of released particles was centrifuged and redispersed in a 1 wt% FITC ethanol solution (compare Fig. 8.1). After incubation time of 1 min the sample was washed three times in ethanol by centrifugation and subsequent redispersion using ultrasonic bath (37 kHz, Elmasonic P). Alternatively fluorescence labelling for 3D patches was conduct by introducing quantum dots into the polymeric ink layer prior to printing. For this, 1 wt% of quantum dots were added to the aqueous polymeric ink solution (with respect to the polymer weight) and diluted to the required concentration.

Avidin and Biotin Functionalization Patched particles were functionalized with avidin and biotin by EDC/NHS-crosslinking using their carboxyl group and thereby covalently bonding them to the amines of the PEI patch. 1 mg of EDC was dissolved in 100 µL of PBS-buffer (pH = 7.4), 2 mg NHS in 20 µL DMSO and 1 mg avidin or biotin was dissolved in 500 µL PBS-buffer. A released particle sample was collected and then re-dispersed in 100 µL of PBS-buffer. The EDC, NHS and avidin/biotin solution were mixed into additional 100 µL of PBS-buffer. After 15 min the particle solution was added to this mixture and the vessel was tilted for 2 h (Nutating Mixer). Finally, the functionalized particles were washed three times with PBS-buffer to remove remaining reagents.

Arylazopyrazoles and Cyclodextrin Functionalization Patched particles were functionalized with arylazopyrazoles and cyclodextrin using there carboxyl group and covalently bonding them to the amine groups of the PEI patch by EDC/NHS-crosslinking. 1 mg of EDC was dissolved in 100 µL of PBS-buffer (pH = 7.4), 2 mg NHS in 20 µL DMSO and 1 mg arylazopyrazoles or cyclodextrin was dissolved in 200 µL DMSO. A released particle sample was collected and then re-dispersed in 500 µL of PBS-buffer. The EDC, NHS and avidin/biotin solution were mixed into additional 100 µL of PBS-buffer. After 15 min the particle solution was added to this mixture and the vessel was tilted for 2 h (Nutating Mixer). Finally, the functionalized particles were washed three times with PBS-buffer to remove remaining reagents.

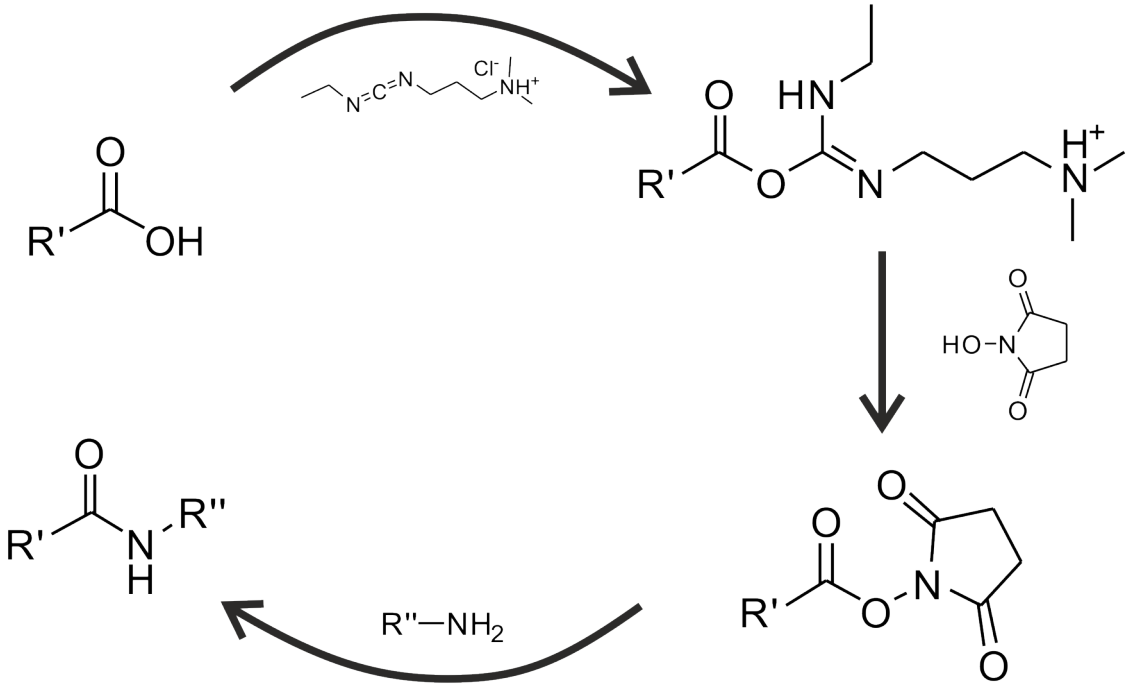

Figure 8.2 Example reaction scheme of the EDC/NHS coupling between a molecule with carboxyl group and a primary amine.

Chemical Vapour Deposition for Amphiphilic Particles The first step of the production of amphiphilic particles via chemical vapour deposition, was an usual µCP process for SPP without releasing the particles from the PDMS stamp. The displayed results were obtained by using 4 µm silica spheres with a PEI concentration of 3 wt% and 2 µm spheres with 2 wt% PEI. The loaded PDMS stamps were located inside a desiccator with small solvent reservoir on the bottom. For the hydrophilic modification of the particle surface, 100 µL of ocytyltriethoxysilane were inserted into the solvent reservoir. The desiccator was

thoroughly closed and connected to a membrane vacuum pump to apply a pressure of 0.4 mbar. After 30 min the vacuum valve was closed and the reaction was conducted for 24 h. Afterwards, the desiccator was open carefully to release entrapped silane vapours and the PDMS stamps were removed. Further particle release and patch labelling was conducted as previously described.

8.2.6 Self-Assembly of Superparamagnetic Patchy Particles

Initially, magnetic single patched particles were printed as described above. A concentration of 4 wt% superparamagnetic nano additives (with respect to the polymer weight) was chosen inside the polymer ink. After particle release in acetone and cleaning in ethanol, the magnetic SPP were dispersed in 150 µL water using ultrasonic bath (37 kHz, Elmasonic P) and inserted into a *Tek-Lab* coverglass chamber with lid. The closed container was directly placed between two neodymium magnets with a distance of 10 cm. After 30 min the homobifunctional crosslinker with epoxy functionality was added (10 µL, 1 g L^{-1}) and the sample remained between the magnets for another 24 h. Finally, the sample was placed onto the fluorescence microscope for imaging.

8.2.7 Swelling Degree Measurement of Polyethylenimine Films

The swelling degree of PEI films was measured by ellipsometry and samples were prepared as follows: A piece of silicon wafer (1 x 1 cm^2) was cleaned using a CO_2 snow-jet.[216] Afterwards the surface was air plasma activated (60 s, 300 W, 0.2 mbar, PlasmaFlecto 10) to remove hydrophobicity. Finally, a 1 wt% PEI solution was spin coated onto the silicon wafer (60 s at 4000 rpm / Laurell WS-650-23B). After drying, the sample was inserted into a vapour chamber with sight glasses for the optical path of the ellipsometry instrument. To simulate the situation during particle release, a solvent reservoir was enclosed with the sample and the film thickness was measured over time.

8.3 Instruments

Atomic Force Microscope Close-up and precise imaging of the PDMS stamps after solvent assisted particle release of printed particles was conducted by atomic force microscopy (AFM) with a *Bruker* Dimension Icon using Tapping Mode with OTESPA-R3 tips ($k = 26\,\mathrm{N\,m^{-1}}$, $f_0 = 300\,\mathrm{kHz}$). Nanoscope (Version 9.1) and Nanoscope Analysis (Version 1.5) were used for measurements and for the image processing, respectively.

Dynamic Light Scattering and Surface Potential Measurement Particle size and zeta potential of fully surface functionalized particles were measured with a *Malvern* Zetasizer Nano ZS possessing a red 633 nm laser. For data processing the *Malvern* Zetasizer Software (Version 7.11) was used. All particle sizes are given as the mean value of the Z-Average of at least five size measurements with its standard deviation. Values for pH-dependent zeta potential measurement are mean values of three measuring points for every pH value with the corresponding standard deviation.

Ellipsometry Film thickness measurement in combination with swelling experiments due to solvent vapour annealing of polyethyleneimine were conducted using an ellipsometer from the company *Optrel GBR* named Multiskop. For data processing the software Elli (Version 3.2) was used.

Fluorescence and Light Microscope All fluorescence and light microscope (FL/LM) pictures were taken with a DMi8 (*Leica*) at different magnifications (20x/40x/63x dry and 100x oil objective). For image processing the LAS X software (Version 2.0.0.14332) from *Leica* was used. A 7.5 µL drop of liquid sample was placed in between to microscope cover slides and for long time experiments or to prevent solvent evaporation, at least 100 µL were used inside a eight-well chamber system.

Scanning Electron Microscope For all scanning electron microscopy (SEM) images a JSM6330F (*JOEL*) and a GeminiSEM 300 (*Zeiss*) at an acceleration voltage of 5 kV were used. Before measuring, the samples were sputtered with platinum layer with a thickness of 4 nm. Further image adaptations (e.g. crop picture, insertion of scale bars, subsequent colouring) was conducted using CorelDRAW (Version 16.4.1.1281) from the *Corel Corporation*.

X-Ray Photoelectron Spectroscopy X-ray photoelectron spectroscopy (XPS) measurements were carried out using an AXIS165 instrument (*Kratos Analytical, UK*). Monochromatic Al-K_α radiation (300 W) was used for excitation. The instrument was run in electrostatic mode and thermal electrons from a filament were used to neutralize the sample charges. CASA-XPS software (Version 2.3.16) was used for data processing. All quantification was carried out after subtracting a Shirley background and Gaussian-Lorentzian functions (30% Lorentz) were used for peak fitting.

8.4 Calculations

8.4.1 Patch Parameters

Patch Diameter

The patch diameter d_i was measured using fluorescence microscope image of the labelled patches for every set of microcontact printing parameters (e.g. 4 µm SPP printed with 1 wt% PEI), but for more than one experiment. The mean value of the patch diameter d was calculated as follows:

$$d = \frac{\sum_{i=0}^{n} d_i}{n} \tag{8.1}$$

The error margin for the patch diameter e_d was calculated as the standard deviation based on a sample as follows:

$$e_d = \sqrt{\frac{\sum_{i=0}^{n} (d_i - d)^2}{n-1}} \tag{8.2}$$

Patch Thickness

The patch thickness t_i was measured using atomic force microscopy of loaded PDMS stamps after the solvent assisted particle release in the ultrasonic bath. Due to the remaining holes inside the ink film, an indirect method of determination of the patch thickness was possible. The mean value of the patch thickness t was calculated as follows:

$$t = \frac{\sum_{i=0}^{n} t_i}{n} \tag{8.3}$$

The error margin for the patch diameter e_t was calculated as the standard deviation based on a sample as follows:

$$e_t = \sqrt{\frac{\sum_{i=0}^{n} (t_i - t)^2}{n-1}} \tag{8.4}$$

Surface Fraction of Patch

For a better impression of the range which is available with this approach, the surface fraction of the patch A_f was calculated. For this, the surface area of the patch was calculated using the determined patch diameter d for all microcontact printing parameters and the surface area of the particle with the particle radius r obtained from the supplier:

$$A_f = \frac{A_{\text{Patch}}}{A_{\text{Particle}}} \cdot 100\% = \frac{\pi \cdot \left(\frac{d}{2}\right)^2}{4 \cdot \pi \cdot r^2} \cdot 100\% \tag{8.5}$$

Patch Diameter Ratio

To compare symmetry of both patches during the synthesis of DPP the patch diameter ratio R was calculated as the quotient of the larger and small patch diameter:

$$R = \frac{d_{\text{large}}}{d_{\text{small}}} \geq 1 \tag{8.6}$$

Patch Yield

In the case of SPP the patch yield Y_{SPP} was calculated as the ratio of particles with one clearly visible patch n_{SPP} and number of particles without n_{Without} plus flawed patches n_{Flawed} in a given sample. For the patch yield of DPP particles Y_{DPP} only particles with two clearly visible patches were accounted for:

$$Y_{\text{SPP}} = \frac{n_{\text{SPP}}}{n_{\text{Without}} + n_{\text{Flawed}}} \qquad Y_{\text{DPP}} = \frac{n_{\text{DPP}}}{n_{\text{Without}} + n_{\text{Flawed}} + n_{\text{SPP}}} \tag{8.7}$$

Yield calculations were performed beginning with a particle number of at least 50 per printing experiment.

8.4.2 Influence of Particle Size Distribution

To calculate the influence of the natural particle size distribution ($r \pm \delta$) on the patch diameter d during microcontact printing, the following simple mathematical model was applied. After printing, the particle is completely emerged into the ink film without altering its surrounding surface (no deformation of the ink). The particle rests on top of the PDMS stamp, which is not penetrable and does not bend (see Fig. 5.3). This model is very simplified and will give an absolute minimum for the influence of the particle size

distribution, since bending of the soft PDMS stamps is more than reasonable and will lead to an increase in the absolute patch diameter value. By measuring the polymer film thickness for the used PEI solutions (compare Fig. 2.10) h was obtained for all samples. The particle radius r_i is taken from the manufacturers records which possesses a certain range (cv. = coefficient of variation = δ). Therefore we are able to use:

$$\begin{aligned}(r_i - h)^2 + x^2 &= r_i^2 \\ x^2 &= r_i^2 - (r_i - h)^2 \\ x &= \sqrt{r_i^2 - (r_i - h)^2} \\ x &= \sqrt{r_i^2 - r_i^2 + 2r_i h - h^2} \\ x &= \sqrt{2r_i h - h^2}\end{aligned} \tag{8.8}$$

With this we are able to calculate the influence limits on the patch diameter $d_{\pm\delta}$ as follows:

$$d_{\pm\delta} = 2x = 2\sqrt{2(r_i \pm \delta) \cdot h - h^2} \tag{8.9}$$

The resulting graphs, calculated error describing this influence e_x and corresponding discussion can be found in section 5.1.

8.4.3 Printing Pressure for Different Particle Sizes

In order to calculate the change of printing pressure P for different particle size systems or flat substrates at a given printing force F, a mathematical model system was constructed (compare Fig. 5.3). Starting from a square substrate with the surface area A_{Subs} (edge length a), the amount of monodisperse particles n_{Part} with the diameter $2r_i$ which are necessary to build a dense monolayer on top was calculated. To take into account the two-dimensional close-packing of equal spheres, the corresponding packaging factor f was introduced.[221] For this two-dimensional projection A_{Part} of the particles space was introduced:

$$n_{\mathrm{Part}} = \frac{A_{\mathrm{Subs}}}{A_{\mathrm{Part}}} \cdot f = \frac{a^2}{\pi \cdot r_i^2} \cdot \frac{\pi}{3\sqrt{2}} \tag{8.10}$$

Additionally, the contact area between each particle and the polymer ink A_{ConPart} film was calculated by using the patch diameter d_x obtained in the previous mathematical

assumption (compare section 8.4.2) for different particles sizes without including the influence of the particle size distribution δ:

$$A_{\text{ConPart}} = \pi \cdot \frac{{d_x}^2}{2} \tag{8.11}$$

With this, the total contact area between all particles and the polymer film on the substrate A_{Contact} could be calculated:

$$A_{\text{Contact}} = A_{\text{ConPart}} \cdot n_{\text{Part}} \tag{8.12}$$

Finally the printing pressure for different values of d, representing the various particles sizes, could be calculated as follows:

$$P_x = \frac{F}{A_{\text{Contact}}} = \frac{F}{\left(\frac{{d_x}^2}{2} \cdot \frac{a^2}{r_i^2} \cdot \frac{\pi}{3\sqrt{2}}\right)} \tag{8.13}$$

For better visualization a relative printing pressure P_r scaled to the printing pressure of the 5 µm sample was introduced:

$$P_r = \frac{P_x}{P_{5\,\mu\text{m}}} \cdot 100\,\% \tag{8.14}$$

The achieved results and their discussion can be found in section 5.2.

8.4.4 Surface Roughness

To compare different PDMS manufacturing processes the roughness of the stamp surface was obtained using AFM images and the corresponding *Nanoscope* software. The roughness parameter R_q was calculated following the root mean squared method with y_i^2 as the mean square of the measured height profile across the surface:

$$R_q = \sqrt{\frac{1}{n}\sum_{i=1}^{n} y_i^2} \tag{8.15}$$

CHAPTER 9

Appendix

9.1 Tables

The tables in this section summarize the achieved results concerning patch diameter d and thickness t for single and double patched particles (SPP & DPP) with different silica particles sizes and all applicable ink concentrations. The error margins shown here are calculated as the standard deviation based on a sample.

Patch Diameter

Table 9.1 Patch diameter d with standard deviation for single patched particles (SPP) at different particle sizes and increasing ink concentration. Results were obtained using fluorescence microscopy and measuring the patches in different samples.

PEI [wt%]	$d_{5\,\mu m}$	$d_{4\,\mu m}$	$d_{2\,\mu m}$	$d_{1\,\mu m}$
1	$(1.80 \pm 0.22)\,\mu m$	$(1.72 \pm 0.17)\,\mu m$	$(1.13 \pm 0.15)\,\mu m$	$(0.59 \pm 0.08)\,\mu m$
2	$(2.16 \pm 0.29)\,\mu m$	$(2.00 \pm 0.20)\,\mu m$	$(1.20 \pm 0.15)\,\mu m$	
3	$(2.38 \pm 0.31)\,\mu m$	$(2.23 \pm 0.25)\,\mu m$		
4	$(2.57 \pm 0.32)\,\mu m$			

Table 9.2 Patch diameter d with standard deviation for double patched particles (DPP) at different particle sizes and increasing ink concentration. Results were obtained using fluorescence microscopy and measuring the patches in different samples.

PEI [wt%]	$d_{5\,\mu m}$	$d_{4\,\mu m}$	$d_{2\,\mu m}$	$d_{1\,\mu m}$
1	$(1.96 \pm 0.25)\,\mu m$	$(1.72 \pm 0.25)\,\mu m$	$(1.01 \pm 0.11)\,\mu m$	$(0.50 \pm 0.07)\,\mu m$
2	$(2.30 \pm 0.25)\,\mu m$	$(1.84 \pm 0.26)\,\mu m$	$(1.18 \pm 0.18)\,\mu m$	
3	$(2.45 \pm 0.31)\,\mu m$	$(2.23 \pm 0.39)\,\mu m$		
4	$(2.37 \pm 0.45)\,\mu m$			

Table 9.3 The patch surface area as a fraction of the total particle surface A_f for single patched particles (SPP) at different particles sizes and increasing polymer ink concentration.

PEI [wt%]	$A_{f\ 5\,\mu m}$	$A_{f\ 4\,\mu m}$	$A_{f\ 2\,\mu m}$	$A_{f\ 1\,\mu m}$
1	3.2 %	4.6 %	8.0 %	8.6 %
2	4.7 %	6.3 %	9.0 %	
3	5.7 %	7.8 %		
4	6.6 %			

Table 9.4 The patch diameter ratio R for double patched particles (DPP) at different particles sizes and increasing polymer ink concentration.

PEI [wt%]	$R_{\,5\,\mu m}$	$R_{\,4\,\mu m}$	$R_{\,2\,\mu m}$	$R_{\,1\,\mu m}$
1	1.12	1.16	1.16	1.16
2	1.13	1.16	1.16	
3	1.16	1.16		
4	1.16			

Patch Thickness

Table 9.5 Patch thickness t with standard deviation for single patched particles (SPP) at different particle sizes and increasing ink concentration. Results were obtained indirectly using atomic force microscopy on the dried PDMS stamps after particle release.

PEI [wt%]	$t_{\,5\,\mu m}$	$t_{\,4\,\mu m}$	$t_{\,2\,\mu m}$	$t_{\,1\,\mu m}$
1	(23 ± 6) nm	(14 ± 1) nm	(11 ± 4) nm	(8 ± 2) nm
2	(48 ± 5) nm	(29 ± 6) nm	(19 ± 5) nm	
3	(82 ± 4) nm	(62 ± 9) nm		
4	(125 ± 8) nm			

Table 9.6 Patch thickness t with standard deviation for double patched particles (DPP) at different particle sizes and increasing ink concentration. Results were obtained indirectly using atomic force microscopy on the dried PDMS stamps after particle release.

PEI [wt%]	$A_{f\ 5\,\mu m}$	$A_{f\ 4\,\mu m}$	$A_{f\ 2\,\mu m}$
1	(17 ± 5) nm	(8 ± 6) nm	(16 ± 5) nm
2	(26 ± 5) nm	(19 ± 4) nm	(22 ± 12) nm
3	(33 ± 4) nm	(29 ± 9) nm	
4	(87 ± 7) nm		

9.2 Atomic Force Microscope Measurements

The AFM height images displayed in this section are exemplary measurements of dried PDMS stamps after particle release. Results show pictures of the first and, were appropriate, also the second stamp with different silica particles sizes and all applicable ink concentrations. Calculations concerning the patch thickness t were obtained using additional images which are not shown here.

9.2.1 Single Patched Particle Stamps

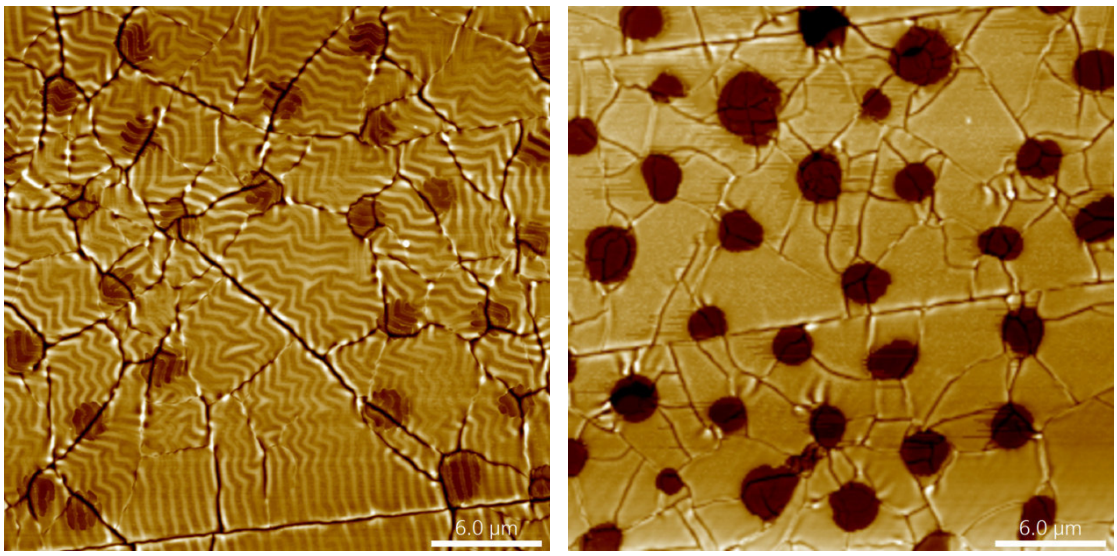

(a) 1 wt% PEI - Height 80 nm

(b) 2 wt% PEI - Height 130 nm

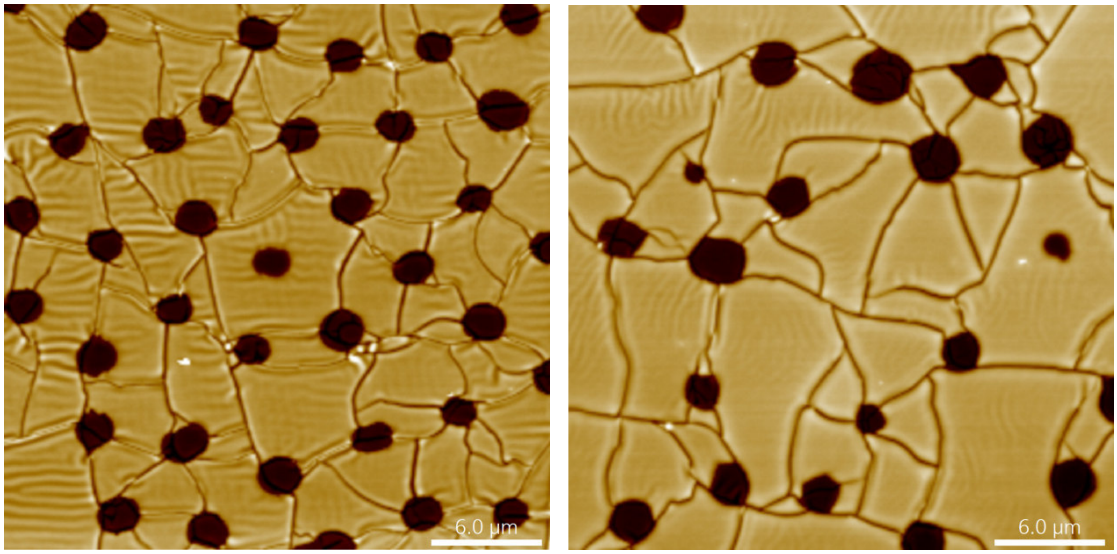

(c) 3 wt% PEI - Height 170 nm

(d) 4 wt% PEI - Height 230 nm

Figure 9.1 AFM images of PDMS stamps loaded with different PEI concentrations after release of 5 µm silica particles in acetone. Images size 30 x 30 μm^2.

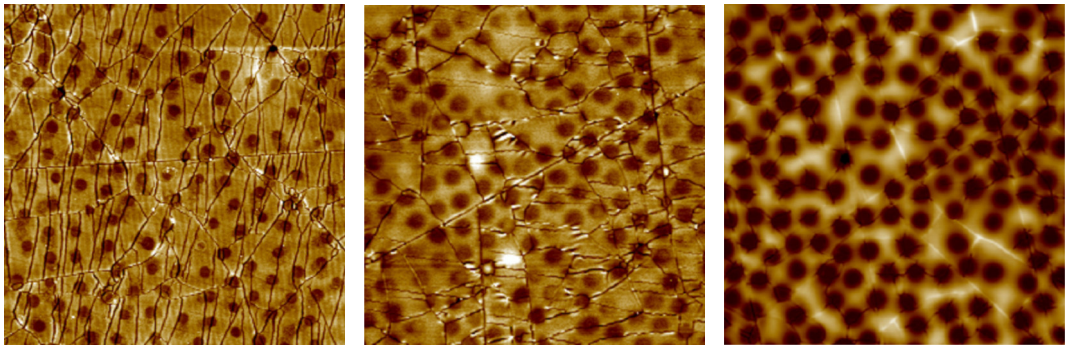

(a) 1 wt% PEI - Height 50 nm (b) 2 wt% PEI - Height 85 nm (c) 3 wt% PEI - Height 160 nm

Figure 9.2 AFM images of PDMS stamps loaded with different PEI concentrations after release of 4 µm silica particles in acetone. Images size 50 x 50 µm^2.

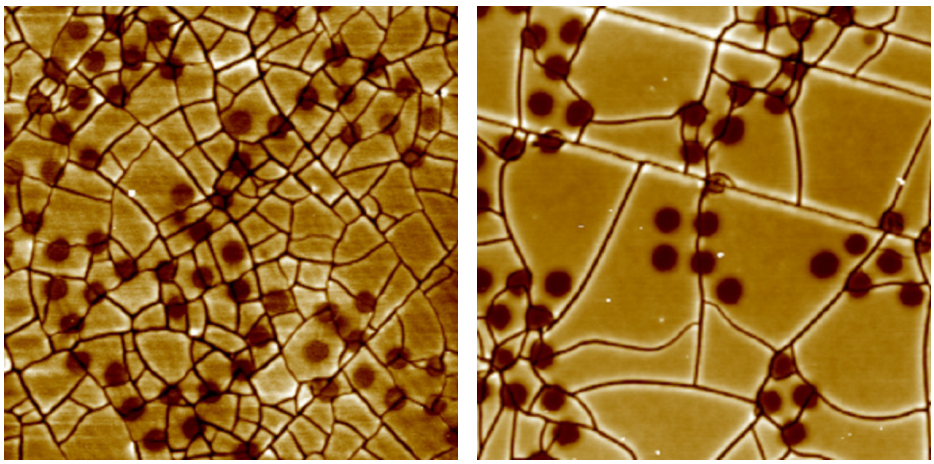

(a) 1 wt% PEI - Height 50 nm (b) 2 wt% PEI - Height 70 nm

Figure 9.3 AFM images of PDMS stamps loaded with different PEI concentrations after release of 2 µm silica particles in acetone. Images size 25 x 25 µm^2.

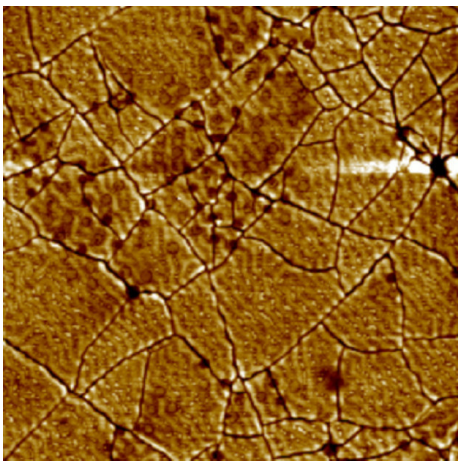

(a) 1 wt% PEI - Height 50 nm

Figure 9.4 AFM images of PDMS stamps loaded with 1 wt% PEI after release of 1 µm silica particles in acetone. Images size 25 x 25 µm^2.

9.2.2 Double Patched Particle Stamps

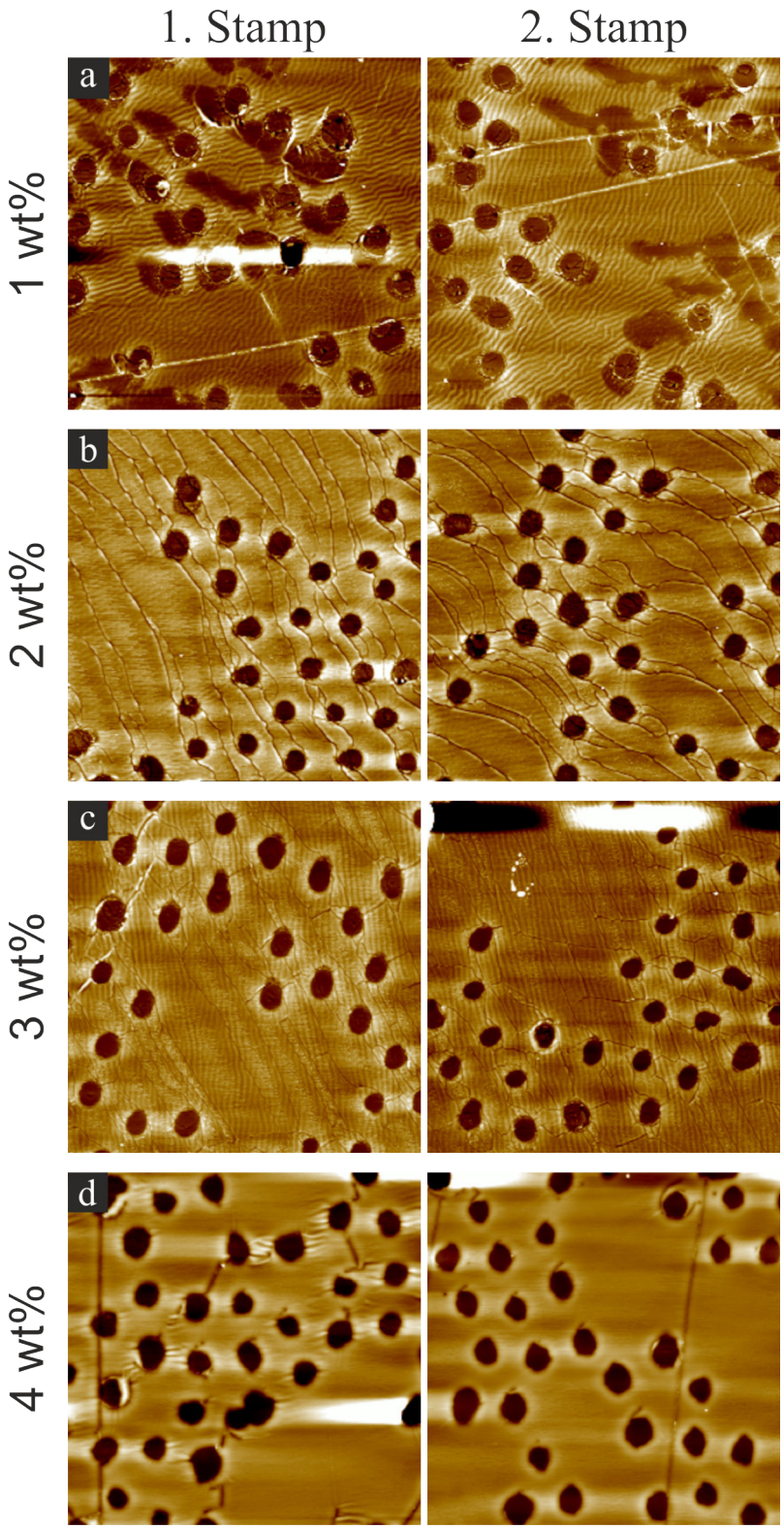

Figure 9.5 AFM images of the first and second PDMS stamps loaded with different PEI concentrations after release of 5 µm silica particles in acetone. Images size 35 x 35 µm^2. Height Scales: a) 55 nm b) 60 nm c) 70 nm d) 180 nm.

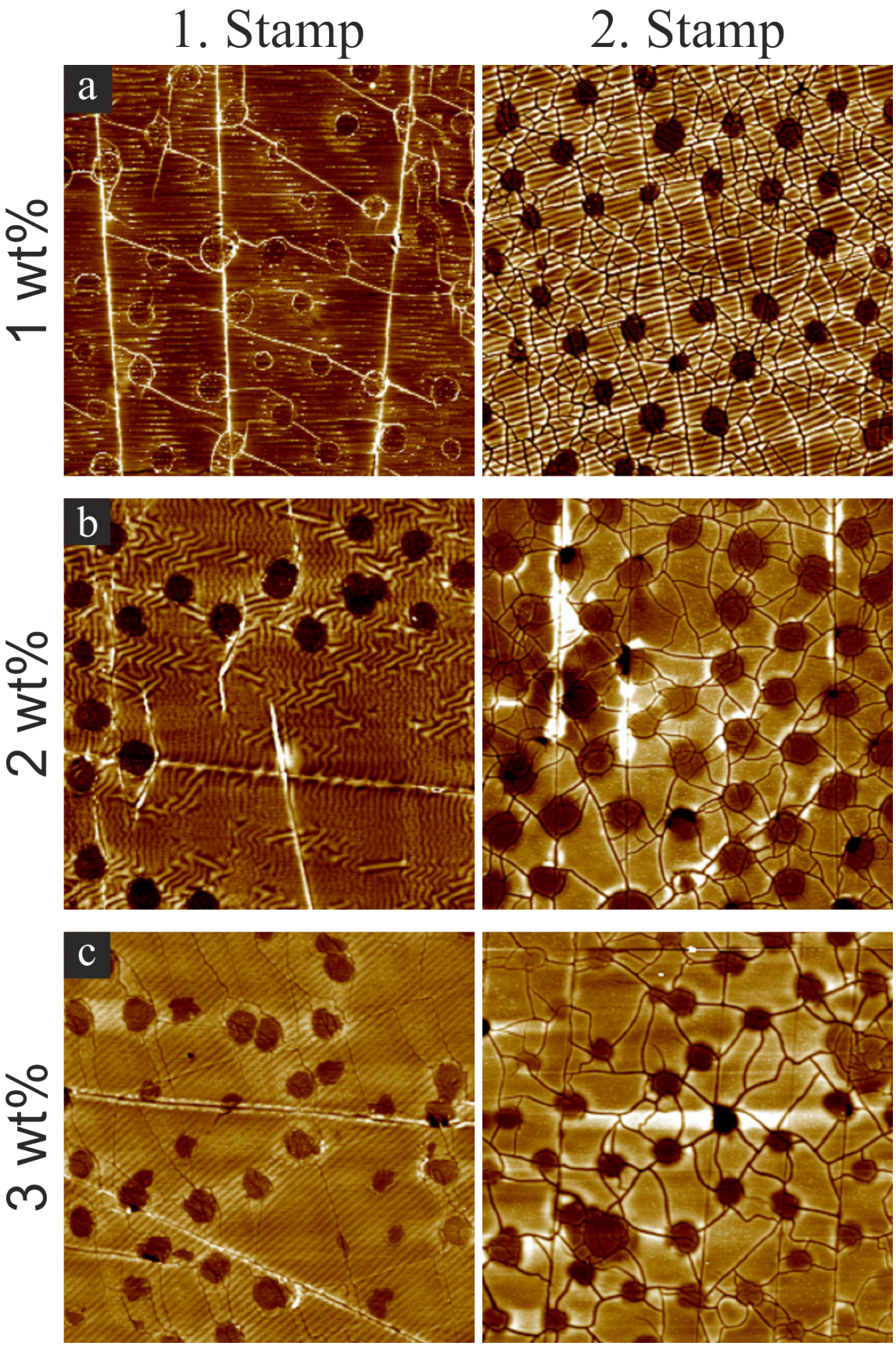

Figure 9.6 AFM images of the first and second PDMS stamps loaded with different PEI concentrations after release of 4 µm silica particles in acetone. Images size 35 x 35 μm^2. Height Scales: a) 30 nm b) 70 nm c) 100 nm.

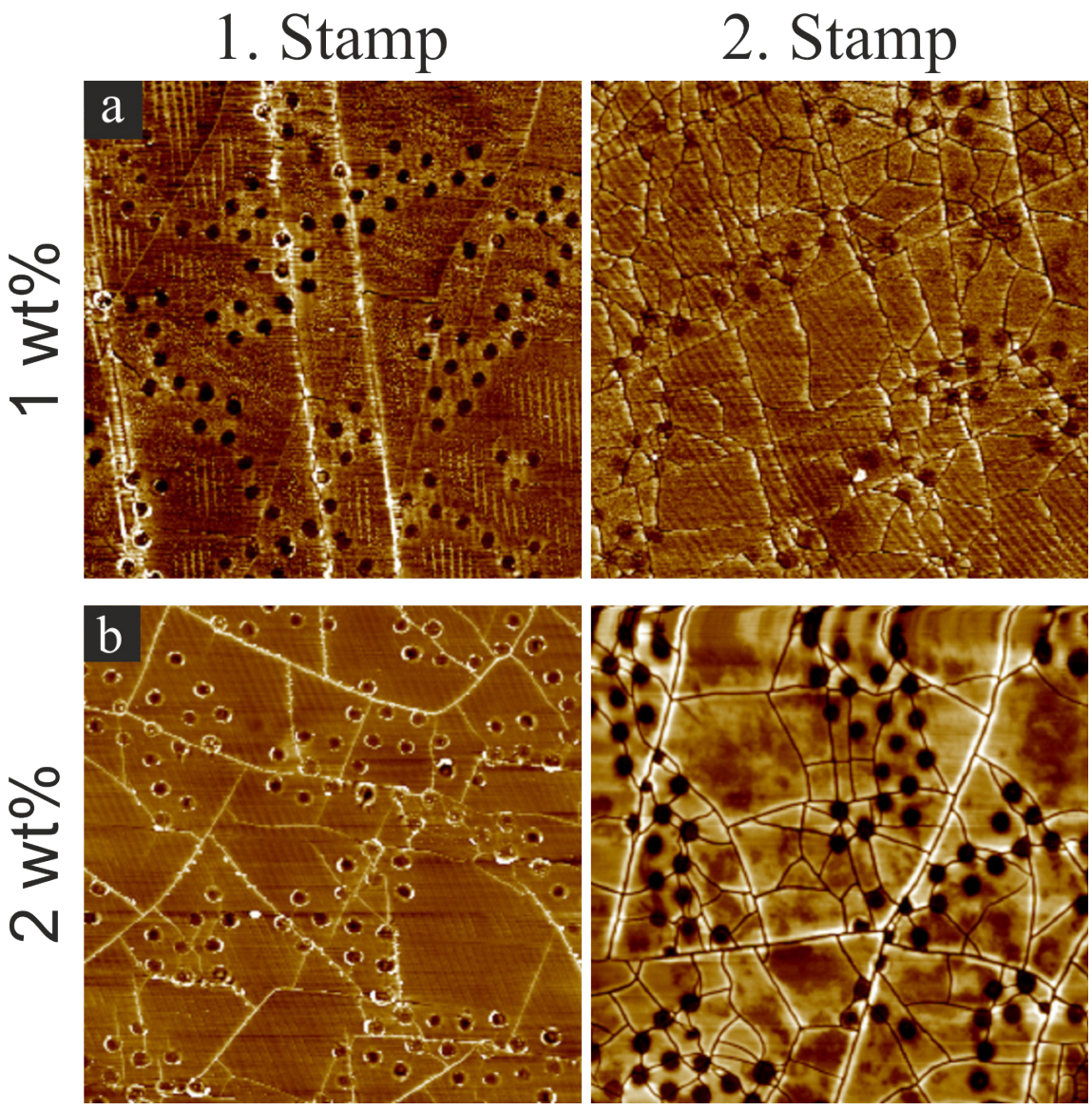

Figure 9.7 AFM images of the first and second PDMS stamps loaded with different PEI concentrations after release of 2 µm silica particles in acetone. Images size 35 x 35 µm^2. Height Scales: a) 30 nm b) 70 nm.

9.2.3 Microcontact Printing using Centrifuge

The AFM height images shown here are exemplary measurement of dried PDMS stamps after particle release. The displayed results are obtained by using the sophisticated microcontact printing approach using centrifugal forces (see section 5.3).

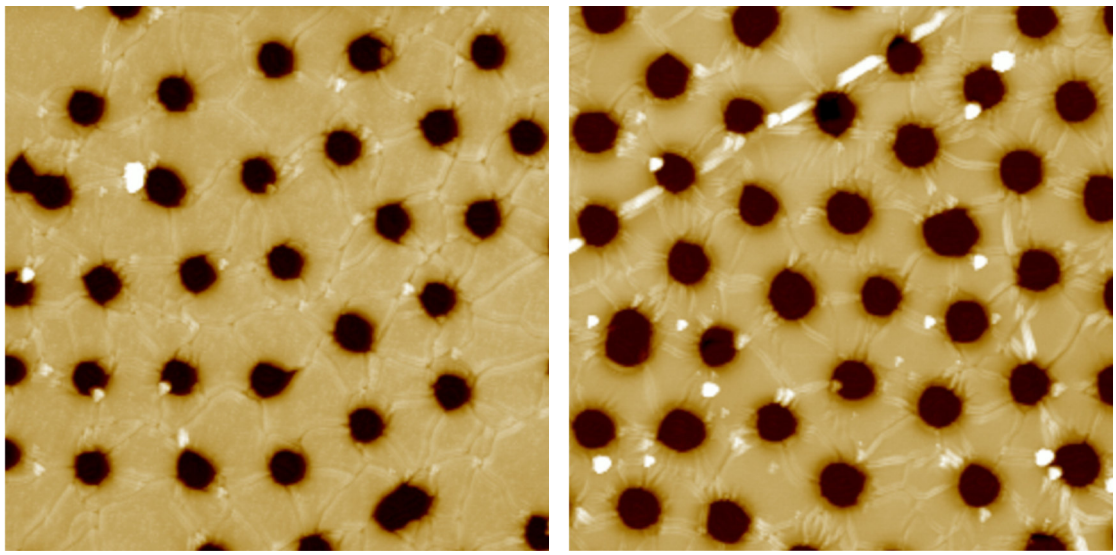

(a) Washer Height 0.9 mm

(b) Washer Height 1.0 mm

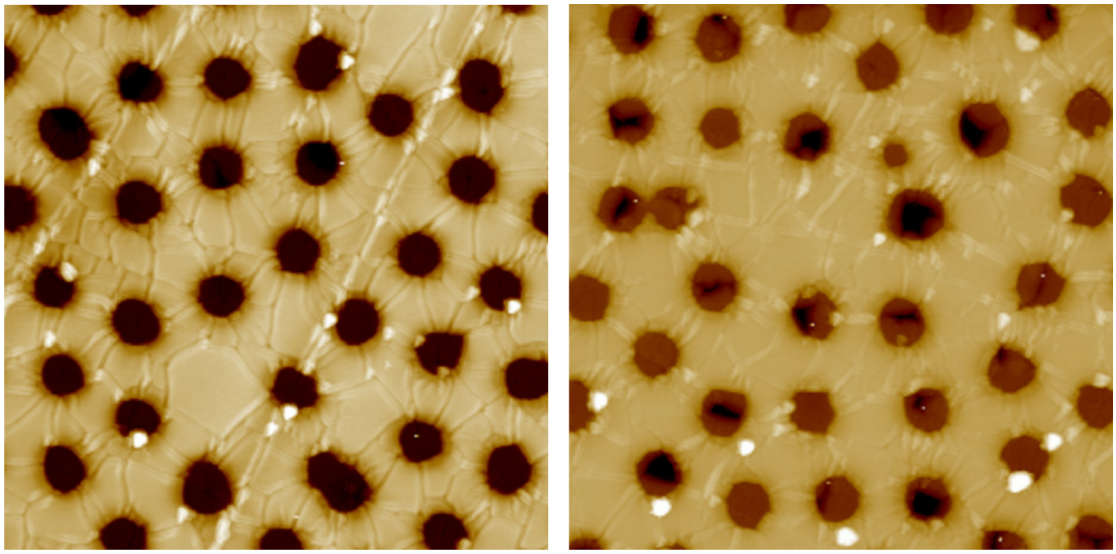

(c) Washer Height 1.1 mm

(d) Washer Height 1.2 mm

Figure 9.8 AFM images of dried PDMS stamps after particle release, produced by microcontact printing *via* centrifuge set-up. Four different printing pressure indicated by differently thick washers were used. Images size 30 x 30 µm^2. Height Scales: a) 150 nm b) 150 nm c) 150 nm d) 290 nm.

9.3 Fluorescence and Light Mircroscope Images

9.3.1 Silica Particle Monolayer

The displayed light microscope images should give an impression of the packing density of different silica particle monolayers and the absence of multilayer formation using the drop casting approach from alcoholic dispersions at low concentrations (compare section 8.2.2).

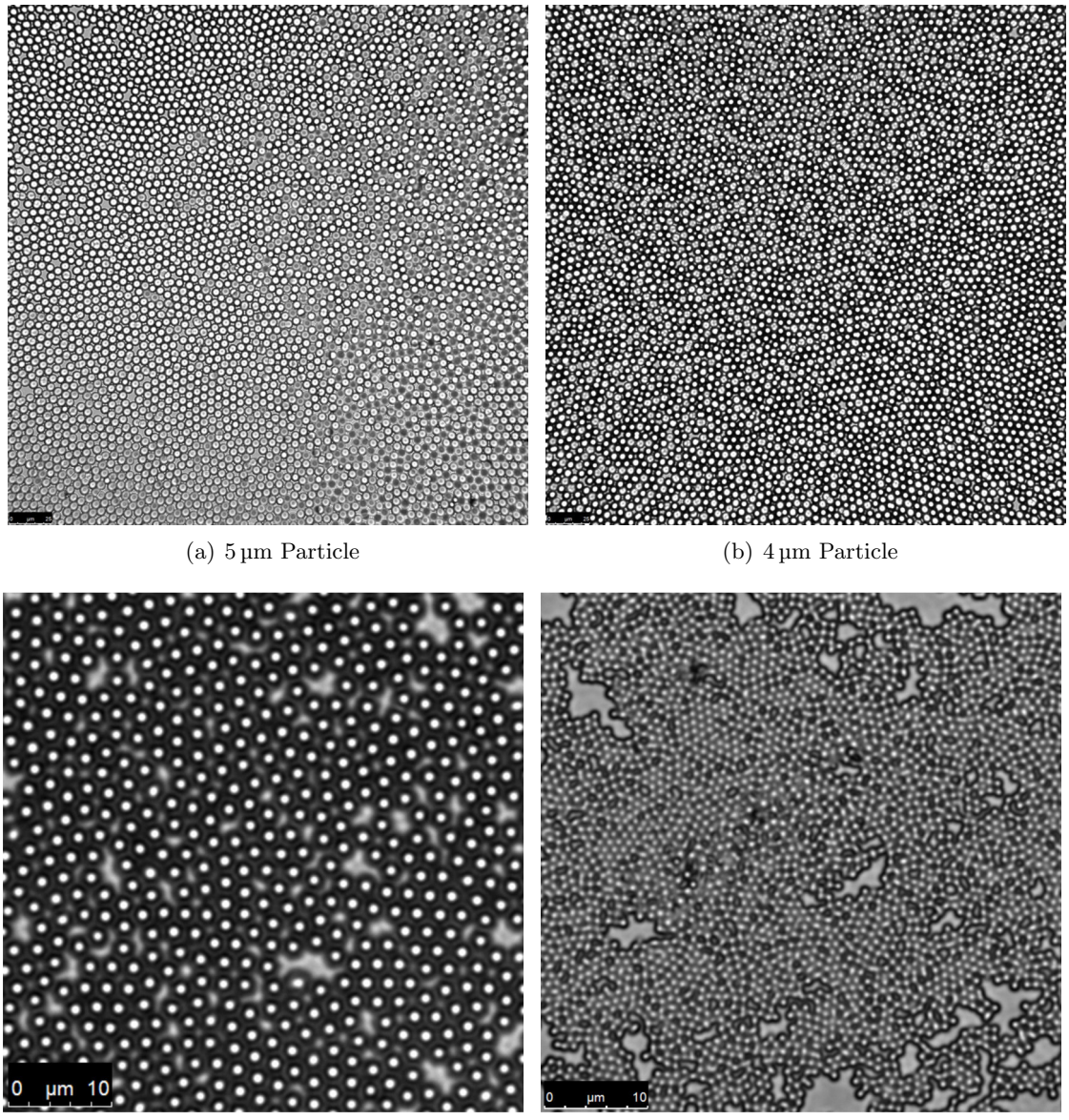

(a) 5 µm Particle

(b) 4 µm Particle

(c) 2 µm Particle

(d) 1 µm Particle

Figure 9.9 Light microscope images of monolayers consisting of different sized silica particles on glass substrate produced by drop casting method.

9.3.2 Avidin-Biotin Coupling

Additional fluorescence microscope images displayed in this section show the behaviour of avidin and biotin modified single patched particles (SPP) prior and after mixing. Without mixing the two species, almost no agglomeration is visible. After mixing the formation of heterodimers becomes noticeable.

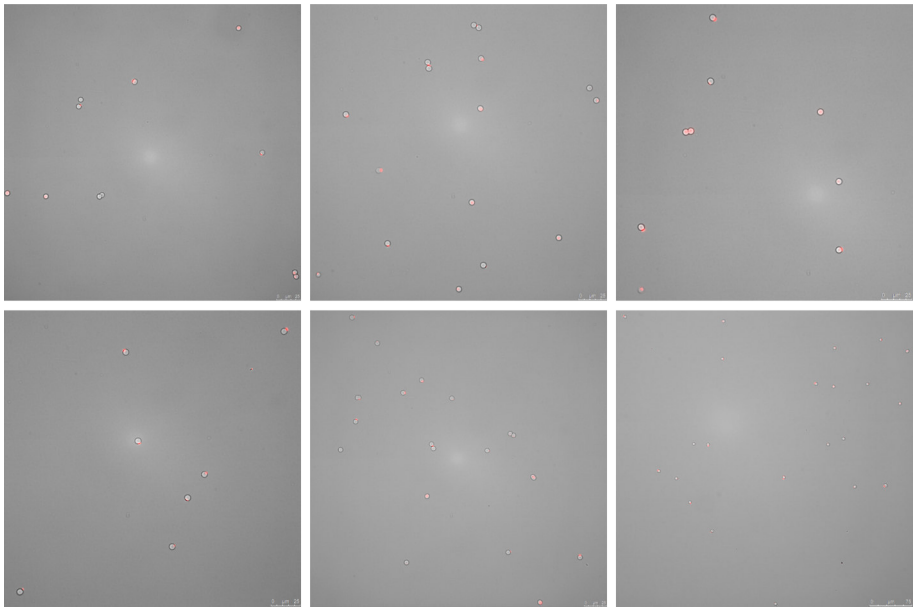

Figure 9.10 Fluorescence microscope images of avidin modified SPP dispersed in PBS-buffer.

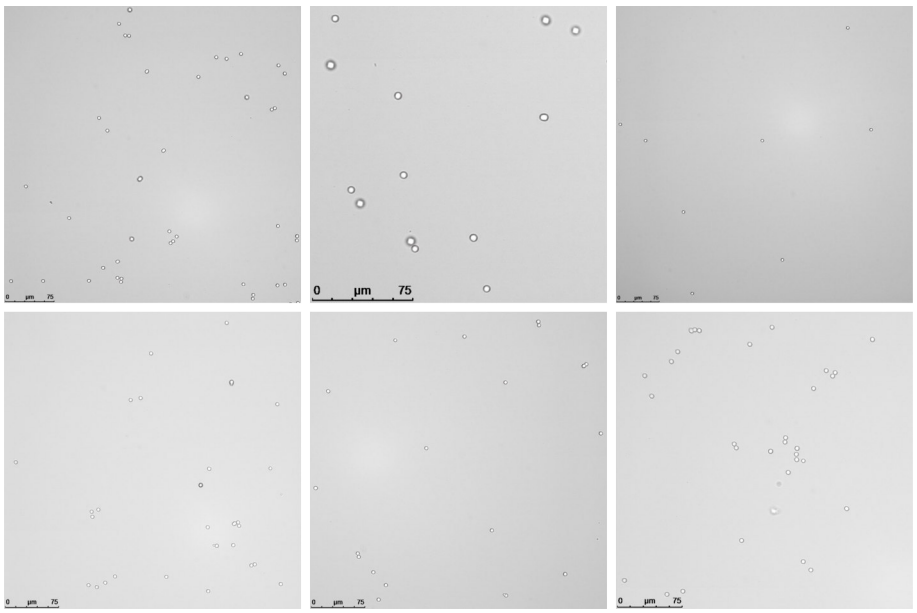

Figure 9.11 Fluorescence microscope images of biotin modified SPP dispersed in PBS-buffer.

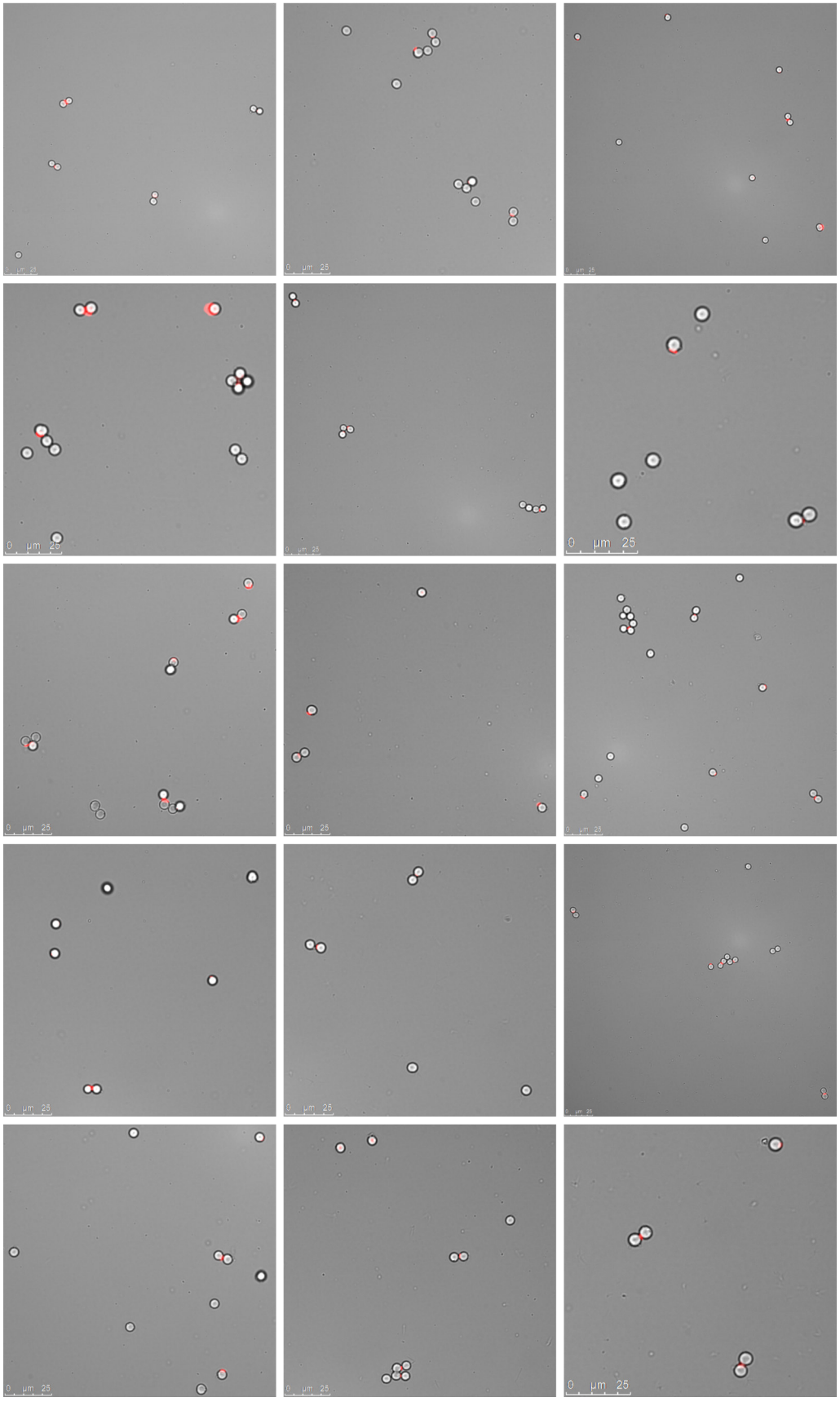

Figure 9.12 Fluorescence microscope images of avidin- and biotin-SPP coupled into heterodimers. A binding efficiency of this coupling system with a value of 55 % was calculated.

9.3.3 Supramolecular Coupling using Arylazopyrazoles and Cyclodextrin

Light microscope images displayed here should show additional images of the heterodimer formation of CD and AAP modified particles. Although singular particles are still visible, the coupling became significant after mixing the two particles species.

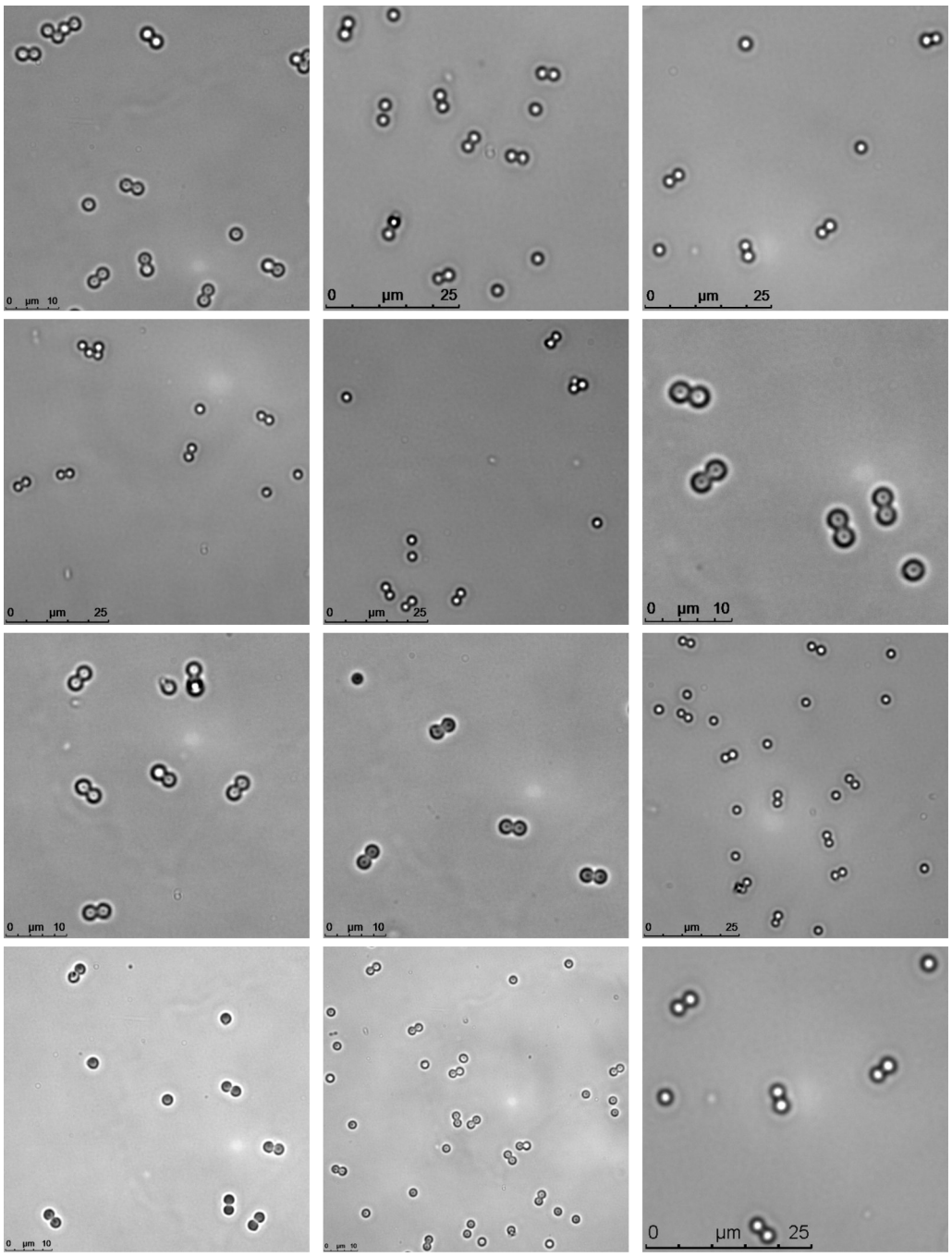

Figure 9.13 Fluorescence microscope images of CD- and AAP-SPP coupled into heterodimers. Presumed that an equal amount of uncoupled particle are modified with CD and AAP, a binding efficiency of 72 % was calculated.

9.4 Printing Pressure Measurement

The figure shows the calculated printing pressures for 43 consecutive printing processes conducted by hand. The pressure was calculated for every point using the area of the PDMS stamp and the used glass substrate and the weight which was read out with a balance during the printing procedure. After this the average printing pressure along with a standard deviation was calculated.

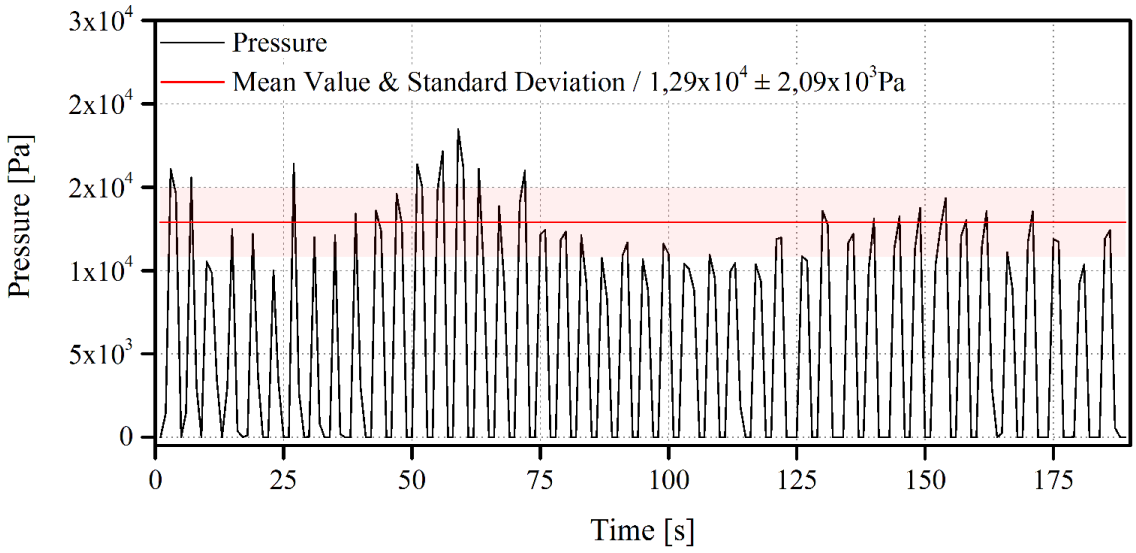

Figure 9.14 Diagram shows the calculated pressure of 43 printing processes over time. An average printing pressure of 1.3×10^4 Pa was calculated. The pressure was calculated using the achieved weight on a balance and the area of the substrates during printing process.

Bibliography

[1] S. C. Glotzer and M. J. Solomon, *Nature Materials*, 2007, **6**, 557–562.

[2] S. M. Yang, S. H. Kim, J. M. Lim and G. R. Yi, *Journal of Materials Chemistry*, 2008, **18**, 2177–2190.

[3] Z. Mao, H. Xu and D. Wang, *Advanced Functional Materials*, 2010, **20**, 1053–1074.

[4] A. B. Pawar and I. Kretzschmar, *Macromolecular Rapid Communications*, 2010, **31**, 150–168.

[5] O. D. Velev and S. Gupta, *Advanced Materials*, 2009, **21**, 1897–1905.

[6] A. P. Gast and W. B. Russel, *Physics Today*, 1998, **51**, 24–30.

[7] F. V. Mikulec, J. D. Kirtland and M. J. Sailor, *Advanced Materials*, 2002, **14**, 38–41.

[8] S. H. Park, D. Qin and Y. Xia, *Advanced Materials*, 1998, **10**, 1028–1032.

[9] M. Holgado, F. García-Santamaría, A. Blanco, M. Ibisate, A. Cintas, H. Míguez, C. J. Serna, C. Molpeceres, J. Requena, A. Mifsud, F. Meseguer and C. López, *Langmuir*, 1999, **15**, 4701–4704.

[10] H. Yan, C. F. Blanford, B. T. Holland, M. Parent, W. H. Smyrl and A. Stein, *Advanced Materials*, 1999, **11**, 1003–1006.

[11] P. V. Braun and P. Wiltzius, *Current Opinion in Colloid and Interface Science*, 2002, **7**, 116–123.

[12] R. R. Bhat, D. A. Fischer and J. Genzer, *Langmuir*, 2002, **18**, 5640–5643.

[13] K. C. Grabar, M. B. Hommer, M. J. Natan and R. G. Freeman, *Analytical Chemistry*, 1995, **67**, 735–743.

[14] N. D. Denkov, O. D. Velev, P. A. Kralchevsky and I. B. Ivanov, *Langmuir*, 1992, **8**, 3183–3190.

[15] N. D. Denkov, O. D. Velev, P. A. Kralchevsky and I. B. Ivanov, *Nature*, 1993, **361**, 26.

[16] A. S. Dimitrov and K. Nagayama, *Langmuir*, 1996, **12**, 1303–1311.

[17] G. Picard, *Langmuir*, 1998, **14**, 3710–3715.

[18] R. Aveyard, J. H. Clint, D. Nees and V. N. Paunov, *Langmuir*, 2000, **16**, 1969–1979.

[19] M. Szekeres, O. Kamalin, P. G. Grobet, R. A. Schoonheydt, K. Wostyn, K. Clays, A. Persoons and I. Dékány, *Colloids and Surfaces A: Physicochemical and Engineering Aspects*, 2003, **227**, 77–83.

[20] J. H. Fendler and F. C. Meldrum, *Advanced Materials*, 1995, **7**, 607–632.

[21] S. O. Lumsdon, E. W. Kaler and O. D. Velev, *Langmuir*, 2004, **20**, 2108–2116.

[22] S. Gupta, R. G. Alargova, P. K. Kilpatrick and O. D. Velev, *Soft Matter*, 2008, **4**, 726–730.

[23] B. Bharti and O. D. Velev, *Langmuir*, 2015, **31**, 7897–7908.

[24] S. Hiltl, J. Oltmanns and A. Böker, *Nanoscale*, 2012, **4**, 7338.

[25] Y. Yin, Y. Lu, B. Gates and Y. Xia, *Journal of the American Chemical Society*, 2001, **123**, 8718–8729.

[26] Y. Masuda, M. Itoh, T. Yonezawa and K. Koumoto, *Langmuir*, 2002, **18**, 4155–4159.

[27] A. V. Terray, J. Oakey and D. W. M. Marr, *Science*, 2002, **296**, 1841–1844.

[28] S. A. Vanapalli, C. R. Iacovella, K. E. Sung, D. Mukhija, J. M. Millunchick, M. A. Burns, S. C. Glotzer and M. J. Solomon, *Langmuir*, 2008, **24**, 3661–3670.

[29] A. van Blaaderen, *Nature*, 2006, **439**, 545–546.

[30] J. Du and R. K. O'Reilly, *Chemical Society Reviews*, 2011, **40**, 2402.

[31] P.-G. De Gennes, *Angewandte Chemie International Edition*, 1992, **31**, 842–845.

[32] Z. Zhang and S. C. Glotzer, *Nano Letters*, 2004, **4**, 1407–1413.

[33] Y. K. Takahara, S. Ikeda, S. Ishino, K. Tachi, K. Ikeue, T. Sakata, T. Hasegawa, H. Mori, M. Matsumura and B. Ohtani, *Journal of the American Chemical Society*, 2005, **127**, 6271–6275.

[34] S. Jiang, Q. Chen, M. Tripathy, E. Luijten, K. S. Schweizer and S. Granick, *Advanced Materials*, 2010, **22**, 1060–1071.

[35] P. D. J. van Oostrum, M. Hejazifar, C. Niedermayer and E. Reimhult, *Journal of Physics: Condensed Matter*, 2015, **27**, 234105.

[36] S. H. Hu and X. Gao, *Journal of the American Chemical Society*, 2010, **132**, 7234–7237.

[37] O. Cayre, V. N. Paunov and O. D. Velev, *Journal of Materials Chemistry*, 2003, **13**, 2445–2450.

[38] T. T. Chastek, S. D. Hudson and V. A. Hackley, *Langmuir*, 2008, **123**, 13897–13903.

[39] L. Feng, R. Dreyfus, R. Sha, N. C. Seeman and P. M. Chaikin, *Advanced Materials*, 2013, **25**, 2779–2783.

[40] Y. Yu, B. Ai, H. Möhwald, Z. Zhou, G. Zhang and B. Yang, *Chemistry of Materials*, 2012, **24**, 4549–4555.

[41] Z. Zhao, Z. Shi, Y. Yu and G. Zhang, *Langmuir*, 2012, **28**, 2382–2386.

[42] R. Brüx, S. Hiltl, V. Schröder, C. Von Essen and A. Böker, *Particle and Particle Systems Characterization*, 2014, **31**, 871–878.

[43] Q. Chen, E. Diesel, J. K. Whitmer, S. C. Bae, E. Luijten and S. Granick, *Journal of the American Chemical Society*, 2011, **133**, 7725–7727.

[44] S. Jiang, J. Yan, J. K. Whitmer, S. M. Anthony, E. Luijten and S. Granick, *Physical Review Letters*, 2014, **112**, 1–5.

[45] J. Yan, S. C. Bae and S. Granick, *Soft Matter*, 2015, **11**, 147–153.

[46] K. B. Shepard, D. A. Christie, C. L. Sosa, C. B. Arnold and R. D. Priestley, *Applied Physics Letters*, 2015, **106**, 1–5.

[47] T. S. Skelhon, Y. Chen and S. A. Bon, *Soft Matter*, 2014, **10**, 7730–7735.

[48] D. J. Kraft, R. Ni, F. Smallenburg, M. Hermes, K. Yoon, D. A. Weitz, A. van Blaaderen, J. Groenewold, M. Dijkstra and W. K. Kegel, *Proceedings of the National Academy of Sciences*, 2012, **109**, 10787–10792.

[49] S. Sacanna, L. Rossi and D. J. Pine, *Journal of the American Chemical Society*, 2012, **134**, 6112–6115.

[50] S. Sacanna, M. Korpics, K. Rodriguez, L. Colón-Meléndez, S.-H. Kim, D. J. Pine and G.-R. Yi, *Nature Communications*, 2013, **4**, 1688.

[51] N. Castro, D. Constantin, P. Davidson and B. Abécassis, *Soft Matter*, 2016, **12**, 9666–9673.

[52] I. Schick, S. Lorenz, D. Gehrig, A. M. Schilmann, H. Bauer, M. Panthöfer, K. Fischer, D. Strand, F. Laquai and W. Tremel, *Journal of the American Chemical Society*, 2014, **136**, 2473–2483.

[53] F. Tu and D. Lee, *Journal of the American Chemical Society*, 2014, **136**, 9999–10006.

[54] L. C. Bradley, K. J. Stebe and D. Lee, *Journal of the American Chemical Society*, 2016, **138**, 11437–11440.

[55] G. R. Yi, V. N. Manoharan, E. Michel, M. T. Elsesser, S. M. Yang and D. J. Pine, *Advanced Materials*, 2004, **16**, 1204–1208.

[56] C. Hubert, C. Chomette, A. Désert, M. Sun, M. Treguer-Delapierre, S. Mornet, A. Perro, E. Duguet and S. Ravaine, *Faraday Discussions*, 2015, **181**, 139–146.

[57] Y. Wang, X. Zheng, Y. Wang, D. J. Pine and M. Weck, *Chemistry of Materials*, 2016, **28**, 3984–3989.

[58] E. Elacqua, X. Zheng and M. Weck, *ACS Macro Letters*, 2017, **6**, 1060–1065.

[59] J. Zhu, S. Zhang, F. Zhang, K. L. Wooley and D. J. Pochan, *Advanced Functional Materials*, 2013, **23**, 1767–1773.

[60] Y. Wang, A. D. Hollingsworth, S. K. Yang, S. Patel, D. J. Pine and M. Weck, *Journal of the American Chemical Society*, 2013, **135**, 14064–14067.

[61] A. H. Gröschel, A. Walther, T. I. Löbling, F. H. Schacher, H. Schmalz and A. H. E. Müller, *Nature*, 2013, **503**, 247–251.

[62] K. Chaudhary, Q. Chen, J. J. Juárez, S. Granick and J. A. Lewis, *Journal of the American Chemical Society*, 2012, **134**, 12901–12903.

[63] S. Jiang and S. Granick, *Langmuir*, 2009, **25**, 8915–8918.

[64] S. Sagebiel, L. Stricker, S. Engel and B. J. Ravoo, *Chem. Commun.*, 2017, **53**, 9296–9299.

[65] T. Kaufmann, M. T. Gokmen, S. Rinnen, H. F. Arlinghaus, F. Du Prez and B. J. Ravoo, *Journal of Materials Chemistry*, 2012, **22**, 6190.

[66] B. Chen, Y. Jia, Y. Gao, L. Sanchez, S. M. Anthony and Y. Yu, *ACS Applied Materials & Interfaces*, 2014, **6**, 18435–18439.

[67] L. Sanchez, P. Patton, S. M. Anthony, Y. Yi and Y. Yu, *Soft Matter*, 2015, **11**, 5346–5352.

[68] P. Seidel and B. J. Ravoo, *Macromolecular Chemistry and Physics*, 2016, **217**, 1467–1472.

[69] X. Zhou, H. Xu, J. Cheng, N. Zhao and S. C. Chen, *Scientific Reports*, 2015, **5**, 1–10.

[70] A. Kumar, N. L. Abbott, H. A. Biebuyck, E. Kim and G. M. Whitesides, *Accounts of Chemical Research*, 1995, **28**, 219–226.

[71] Y. Xia and W. George M., *Annual Review of Material Sciences*, 1998, **28**, 152–84.

[72] D. M. Yanker and J. a. Maurer, *Molecular bioSystems*, 2008, **4**, 502–4.

[73] L. Tang and N. Y. Lee, *Lab on a Chip*, 2010, **10**, 1274.

[74] K. Efimenko, W. E. Wallace and J. Genzer, *Journal of Colloid and Interface Science*, 2002, **254**, 306–315.

[75] Y. Gao and Y. Yu, *Langmuir*, 2015, **31**, 2833–2838.

[76] Y. Zhang, L. Ren, Q. Tu, X. Wang, R. Liu, L. Li, J. C. Wang, W. Liu, J. Xu and J. Wang, *Analytical Chemistry*, 2011, **83**, 9651–9659.

[77] H. Hillborg and U. Gedde, *Polymer*, 1998, **39**, 1991–1998.

[78] J. Genzer and J. Groenewold, *Soft Matter*, 2006, **2**, 310.

[79] W. T. S. Huck, N. Bowden, P. Onck, T. Pardoen, J. W. Hutchinson and G. M. Whitesides, *Langmuir*, 2000, **16**, 3497–3501.

[80] Y. Iwashita and Y. Kimura, *Scientific Reports*, 2016, **6**, 27599.

[81] T. Kaufmann, M. T. Gokmen, C. Wendeln, M. Schneiders, S. Rinnen, H. F. Arlinghaus, S. A. F. Bon, F. E. Du Prez and B. J. Ravoo, *Advanced Materials*, 2011, **23**, 79–83.

[82] C. Ziegler and A. Eychmüller, *Journal of Physical Chemistry C*, 2011, **115**, 4502–4506.

[83] W. Stöber, A. Fink and E. Bohn, *Journal of Colloid and Interface Science*, 1968, **26**, 62–69.

[84] M. Kobayashi, F. Juillerat, P. Galletto, P. Bowen and M. Borkovec, *Langmuir*, 2005, **21**, 5761–5769.

[85] X. Li, O. Niitsoo and A. Couzis, *Journal of Colloid and Interface Science*, 2013, **394**, 26–35.

[86] T. Kaufmann, C. Wendeln, M. T. Gokmen, S. Rinnen, M. M. Becker, H. F. Arlinghaus, F. Du Prez and B. J. Ravoo, *Chemical Communications*, 2013, **49**, 63–65.

[87] D. John, *Ph.D. thesis*, University Potsdam, 2017.

[88] T. Kaufmann and B. J. Ravoo, *Polymer Chemistry*, 2010, **1**, 371–387.

[89] T. Tigges, D. Hoenders and A. Walther, *Small*, 2015, **11**, 4540–4548.

[90] A. Winkleman, B. D. Gates, L. S. McCarty and G. M. Whitesides, *Advanced Materials*, 2005, **17**, 1507–1511.

[91] Dow Corning, *Electronics Sylgard ® 184 Silicone Elastomer*, 2013, https://goo.gl/Lcy9P5.

[92] D. Dendukuri and P. S. Doyle, *Advanced Materials*, 2009, **21**, 4071–4086.

[93] M. J. Uddin, M. K. Hossain, W. Qarony, M. I. Hossain, M. Mia and S. Hossen, *Journal of Science: Advanced Materials and Devices*, 2017, **2**, 385–391.

[94] Dow Corning, *Material Safety Data Sheet Sylgard ® 184 Silicone Elastomer*, 2014, https://goo.gl/B9bpqW.

[95] J. Kim, M. K. Chaudhury, M. J. Owen and T. Orbeck, *Journal of Colloid and Interface Science*, 2001, **244**, 200–207.

[96] D. John, M. Zimmermann and A. Böker, *Soft Matter*, 2018, **14**, 3057–3062.

[97] C. M. Stafford, C. Harrison, K. L. Beers, A. Karim, E. J. Amis, M. R. Vanlandingham, H. C. Kim, W. Volksen, R. D. Miller and E. E. Simonyi, *Nature Materials*, 2004, **3**, 545–550.

[98] D. C. Hyun, G. D. Moon, E. C. Cho and U. Jeong, *Advanced Functional Materials*, 2009, **19**, 2155–2162.

[99] C. Lu, H. Möhwald and A. Fery, *Soft Matter*, 2007, **3**, 1530.

[100] K. Efimenko, M. Rackaitis, E. Manias, A. Vaziri, L. Mahadevan and J. Genzer, *Nature Materials*, 2005, **4**, 293–297.

[101] J. Genzer, D. A. Fischer and K. Efimenko, *Advanced Materials*, 2003, **15**, 1545–1547.

[102] K. Khare, J. Zhou and S. Yang, *Langmuir*, 2009, **25**, 12794–12799.

[103] N. Bowden, W. T. S. Huck, K. E. Paul and G. M. Whitesides, *Applied Physics Letters*, 1999, **75**, 2557–2559.

[104] A. L. Volynskii, S. Bazhenov, O. V. Lebedeva and N. F. Bakeev, *Journal of Materials Science*, 2000, **35**, 547–554.

[105] S. Hiltl, *Ph.D. thesis*, RWTH Aachen, 2015.

[106] microparticles GmbH, *Silicapartikel*, 2018, https://goo.gl/gGNase.

[107] T. Liu, L. Li, X. Teng, X. Huang, H. Liu, D. Chen, J. Ren, J. He and F. Tang, *Biomaterials*, 2011, **32**, 1657–1668.

[108] J. Lu, M. Liong, Z. Li, J. I. Zink and F. Tamanoi, *Small*, 2010, **6**, 1794–1805.

[109] A. Liberman, H. P. Martinez, C. N. Ta, C. V. Barback, R. F. Mattrey, Y. Kono, S. L. Blair, W. C. Trogler, A. C. Kummel and Z. Wu, *Biomaterials*, 2012, **33**, 5124–5129.

[110] H. P. Martinez, Y. Kono, S. L. Blair, S. Sandoval, J. Wang-Rodriguez, R. F. Mattrey, A. C. Kummel and W. C. Trogler, *MedChemComm*, 2010, **1**, 266–270.

[111] A. Liberman, Z. Wu, C. V. Barback, R. Viveros, S. L. Blair, L. G. Ellies, D. R. Vera, R. F. Mattrey, A. C. Kummel and W. C. Trogler, *ACS Nano*, 2013, **7**, 6367–6377.

[112] H. Ow, D. R. Larson, M. Srivastava, B. A. Baird, W. W. Webb and U. Wiesner, *Nano Letters*, 2005, **5**, 113–117.

[113] K. R. Hurley, Y. S. Lin, J. Zhang, S. M. Egger and C. L. Haynes, *Chemistry of Materials*, 2013, **25**, 1968–1978.

[114] Y. Lu, Y. Yin, B. T. Mayers and Y. Xia, *Nano Letters*, 2002, **2**, 183–186.

[115] C. Zhang, B. Wängler, B. Morgenstern, H. Zentgraf, M. Eisenhut, H. Untenecker, R. Krüger, R. Huss, C. Seliger, W. Semmler and F. Kiessling, *Langmuir*, 2007, **23**, 1427–1434.

[116] N. Insin, J. B. J. Tracy, H. Lee, J. P. J. Zimmer, R. M. Westervelt and M. G. Bawendi, *ACS Nano*, 2008, **2**, 197–202.

[117] F. Chen, H. Hong, Y. Zhang, H. F. Valdovinos, S. Shi, G. S. Kwon, C. P. Theuer, T. E. Barnhart and W. Cai, *ACS Nano*, 2013, **7**, 9027–9039.

[118] K. W. Kang, *The Open Nuclear Medicine Journal*, 2010, **2**, 153–156.

[119] L. Kong, E. Mume, G. Triani and S. V. Smith, *Langmuir*, 2013, **29**, 5609–5616.

[120] H. Choi and I. W. Chen, *Journal of Colloid and Interface Science*, 2003, **258**, 435–437.

[121] K. Nozawa, H. Gailhanou, L. Raison, P. Panizza, H. Ushiki, E. Sellier, J. P. Delville and M. H. Delville, *Langmuir*, 2005, **21**, 1516–1523.

[122] X. D. Wang, Z. X. Shen, T. Sang, X. B. Cheng, M. F. Li, L. Y. Chen and Z. S. Wang, *Journal of Colloid and Interface Science*, 2010, **341**, 23–29.

[123] A. van Blaaderen and A. Vrij, *Langmuir*, 1992, **8**, 2921–2931.

[124] N. Shimura and M. Ogawa, *Journal of Materials Science*, 2007, **42**, 5299–5306.

[125] T. S. Deng, Q. F. Zhang, J. Y. Zhang, X. Shen, K. T. Zhu and J. L. Wu, *Journal of Colloid and Interface Science*, 2009, **329**, 292–299.

[126] H. Giesche, *Journal of the European Ceramic Society*, 1994, **14**, 189–204.

[127] S. Han, J. Choi, Y. Yoo, E. C. Jung and S. Lee, *Bulletin of the Korean Chemical Society*, 2016, **37**, 335–343.

[128] Y.-G. Lee, J.-H. Park, C. Oh, S.-G. Oh and Y. C. Kim, *Langmuir : the ACS journal of surfaces and colloids*, 2007, **23**, 10875–10878.

[129] J. Lim, S. W. Ha and J. K. Lee, *Bulletin of the Korean Chemical Society*, 2012, **33**, 1067–1070.

[130] H. Nakabayashi, A. Yamada, M. Noba, Y. Kobayashi, M. Konno and D. Nagao, *Langmuir*, 2010, **26**, 7512–7515.

[131] D. R. Radu, C. Y. Lai, J. Huang, X. Shu and V. S. Y. Lin, *Chemical Communications*, 2005, **10**, 1264–1266.

[132] T. Yokoi, H. Yoshitake and T. Tatsumi, *Journal of Materials Chemistry*, 2004, **14**, 951–957.

[133] S. Jambhrunkar, M. Yu, J. Yang, J. Zhang, A. Shrotri and L. Endo-munoz, *Journal of the American Chemical Society*, 2013, **135**, 8444–8447.

[134] D. Zhao, *Science*, 1998, **279**, 548–552.

[135] J. Yang, J. Lee, J. Kang, K. Lee, J. S. Suh, H. G. Yoon, Y. M. Huh and S. Haam, *Langmuir*, 2008, **24**, 3417–3421.

[136] I. Tissot, J. P. Reymond, F. Lefebvre and E. Bourgeat-Lami, *Chemistry of Materials*, 2002, **14**, 1325–1331.

[137] C. Graf, D. L. Vossen, A. Imhof and A. Van Blaaderen, *Langmuir*, 2003, **19**, 6693–6700.

[138] R. Banga, J. Yarwood, A. M. Morgan, B. Evans and J. Kells, *Langmuir*, 1995, **11**, 4393–4399.

[139] T. S. Deng, J. Y. Zhang, K. T. Zhu, Q. F. Zhang and J. L. Wu, *Colloids and Surfaces A: Physicochemical and Engineering Aspects*, 2010, **356**, 104–111.

[140] A. Gang, G. Gabernet, L. D. Renner, L. Baraban and G. Cuniberti, *RSC Adv.*, 2015, **5**, 35631–35634.

[141] H. Puliyalil and U. Cvelbar, *Nanomaterials*, 2016, **6**, 108.

[142] S. Kobayashi, H. Shirasaka, K. Suh and H. Uyama, *Polymer Journal*, 1990, **22**, 442–446.

[143] C. K. Choudhury and S. Roy, *Soft Matter*, 2013, **9**, 2269–2281.

[144] S. M. Notley and Y.-K. Leong, *Physical chemistry chemical physics : PCCP*, 2010, **12**, 10594–10601.

[145] R. Mészáros, L. Thompson, M. Bos and P. De Groot, *Langmuir*, 2002, **18**, 6164–6169.

[146] H.-J. Yun, H. Hong, J. Lee and C.-J. Choi, *Materials Transactions*, 2014, **55**, 2–6.

[147] M. Neu, D. Fischer and T. Kissel, *Journal of Gene Medicine*, 2005, **7**, 992–1009.

[148] Y. K. Buchman, E. Lellouche, S. Zigdon, M. Bechor, S. Michaeli and J. P. Lellouche, *Bioconjugate Chemistry*, 2013, **24**, 2076–2087.

[149] J. Suh, H.-J. Paik and B. K. Hwang, *Bioorganic Chemistry*, 1994, **22**, 318–327.

[150] K. A. Curtis, D. Miller, P. Millard, S. Basu, F. Horkay and P. L. Chandran, *PLoS ONE*, 2016, **11**, 1–20.

[151] B. An, J. Nam, J. W. Choi, S. W. Hong and S. H. Lee, *Journal of Colloid and Interface Science*, 2013, **409**, 129–134.

[152] B. Li, F. Zhou, K. Huang, Y. Wang, S. Mei, Y. Zhou and T. Jing, *Scientific Reports*, 2016, **6**, 1–9.

[153] J. C. J. C. Roberts, *Paper Chemistry*, Chapman and Hall, 1991, p. 234.

[154] I. N. Kurniasih, J. Keilitz and R. Haag, *Chem. Soc. Rev.*, 2015, **44**, 4145–4164.

[155] D. K. Bonner, X. Zhao, H. Buss, R. Langer and P. T. Hammond, *Journal of Controlled Release*, 2013, **167**, 101–107.

[156] S. Ferrari, E. Moro, A. Pettenazzo, J. Behr, F. Zacchello and M. Scarpa, *Gene Therapy*, 1997, **4**, 1100–1106.

[157] C.-S. Cho, *ISRN Materials Science*, 2012, **2012**, 1–24.

[158] S. Di Gioia and M. Conese, *Drug Design, Development and Therapy*, 2008, 163–188.

[159] B. Brissault, A. Kichler, C. Guis, C. Leborgne, O. Danos and H. Cheradame, *Bioconjugate Chemistry*, 2003, **14**, 581–587.

[160] R. Tanaka, I. Ueoka, Y. Takaki, K. Kataoka and S. Saito, *Macromolecules*, 1983, **16**, 849–853.

[161] L. Tauhardt, K. Kempe, K. Knop, E. Altunta??, M. J??ger, S. Schubert, D. Fischer and U. S. Schubert, *Macromolecular Chemistry and Physics*, 2011, **212**, 1918–1924.

[162] B. D. Monnery, S. Shaunak, M. Thanou and J. H. Steinke, *Macromolecules*, 2015, **48**, 3197–3206.

[163] P. A. Rupar, L. Reisman and P. C. Mbarushimana, *Synthesis of linear PEI by living anionic polymerization*, 2017.

[164] G. D. Jones, A. Langsjoen, M. M. C. Neumann and J. Zomlefer, *Journal of Organic Chemistry*, 1944, **9**, 125–147.

[165] C. R. Dick and G. E. Ham, *Journal of Macromolecular Science: Part A - Chemistry*, 1970, **4**, 1301–1314.

[166] M. Jäger, S. Schubert, S. Ochrimenko, D. Fischer and U. S. Schubert, *Chemical Society Reviews*, 2012, **41**, 4755–4767.

[167] A. Von Harpe, H. Petersen, Y. Li and T. Kissel, *Journal of Controlled Release*, 2000, **69**, 309–322.

[168] S. H. Tan, N. T. Nguyen, Y. C. Chua and T. G. Kang, *Biomicrofluidics*, 2010, **4**, 1–8.

[169] T. Swift, L. Swanson, M. Geoghegan and S. Rimmer, *Soft Matter*, 2016, **12**, 2542–2549.

[170] J. Loiseau, N. Doërr, J. M. Suau, J. B. Egraz, M. F. Llauro, C. Ladavière and J. Claverie, *Macromolecules*, 2003, **36**, 3066–3077.

[171] J. Ji, L. Jia, L. Yan and P. R. Bangal, *Journal of Macromolecular Science, Part A: Pure and Applied Chemistry*, 2010, **47**, 445–451.

[172] I. Ristic, A. Miletic, N. Sad and O. Govedarica, Physical Chemistry 2016, 2016, pp. 685–688.

[173] L. Brocken, P. D. Price, J. Whittaker and I. R. Baxendale, *React. Chem. Eng.*, 2017, **2**, 662–668.

[174] B. M. Van Der Zande, M. R. Böhmer, L. G. Fokkink and C. Schönenberger, *Langmuir*, 2000, **16**, 451–458.

[175] P. He, Y. Gao, J. Lian, L. Wang, D. Qian, J. Zhao, W. Wang, M. J. Schulz, X. P. Zhou and D. Shi, *Composites Part A: Applied Science and Manufacturing*, 2006, **37**, 1270–1275.

[176] V. S. Nguyen, D. Rouxel, R. Hadji, B. Vincent and Y. Fort, *Ultrasonics Sonochemistry*, 2011, **18**, 382–388.

[177] M. Sivasubramanian, K. Nedunjezhian, S. Murugesan and R. Kalpoondi Sekar, *Applied Thermal Engineering*, 2012, **44**, 1–10.

[178] I. M. Mahbubul, I. M. Shahrul, S. S. Khaleduzzaman, R. Saidur, M. A. Amalina and A. Turgut, *International Journal of Heat and Mass Transfer*, 2015, **88**, 73–81.

[179] S. Pradhan, J. Hedberg, E. Blomberg, S. Wold and I. Odnevall Wallinder, *Journal of Nanoparticle Research*, 2016, **18**, 1–14.

[180] W.-B. Tsai, J.-Y. Kao, T.-M. Wu and W.-T. Cheng, *Journal of Nanoparticles*, 2016, **2016**, 1–9.

[181] F. J. Fuchs and Blackstone Ultrasonics, *Ultrasonic Cleaning : Fundamental Theory and Application What is "Ultrasonics"?*, 2002, https://goo.gl/TKzUbR.

[182] Stuart R. Brinkle, *Principles of General Chemistry*, The Magmillan Company, Third Edit edn., 1941.

[183] I. Polysciences, *Polyethylenimine, Branched, Mw 10,000 (bPEI 10000)*, 2018, https://goo.gl/rpP1kg.

[184] J. S. Park, H. J. Hah, S. M. Koo and Y. S. Lee, *Journal of Ceramic Processing Research*, 2006, **7**, 83–89.

[185] J. N. Lee, C. Park and G. M. Whitesides, *Analytical Chemistry*, 2003, **75**, 6544–6554.

[186] P. B. Johnson and R. W. Christy, *Physical Review B*, 1972, **6**, 4370–4379.

[187] D. I. Yakubovsky, A. V. Arsenin, Y. V. Stebunov, D. Y. Fedyanin and V. S. Volkov, *Optics Express*, 2017, **25**, 25574.

[188] Sigma-Aldrich, *Polyethylenimine, branched*, https://goo.gl/QsDNVg.

[189] I. Bangs Laboratories, *Silica Microspheres*, 2013.

[190] I. H. Park and E. J. Choi, *Polymer*, 1996, **37**, 313–319.

[191] B. A. Langowski and K. E. Uhrich, *Langmuir*, 2005, **21**, 6366–6372.

[192] A. G. Kolhatkar, A. C. Jamison, D. Litvinov, R. C. Willson and T. R. Lee, *International Journal of Molecular Sciences*, 2013, **14**, 15977–16009.

[193] L. Tan, B. Liu, K. Siemensmeyer, U. Glebe and A. Böker, *Journal of Colloid and Interface Science*, 2018, **526**, 124–134.

[194] A. S. de Dios and M. E. Díaz-García, *Analytica Chimica Acta*, 2010, **666**, 1–22.

[195] O. Livnah, E. A. Bayer, M. Wilchek and J. L. Sussman, *Proceedings of the National Academy of Sciences*, 1993, **90**, 5076–5080.

[196] E. P. Diamandis and T. K. Christopoulos, *Clinical Chemistry*, 1991, **37**, 625–636.

[197] M. Wilchek and E. A. Bayer, *Methods in Enzymology*, 1990, **184**, 5–13.

[198] J. R. Wayment and J. M. Harris, *Analytical Chemistry*, 2009, **81**, 336–342.

[199] S. H. Hu and X. Gao, *Advanced Functional Materials*, 2010, **20**, 3721–3726.

[200] S. K. Vashist, *Diagnostics*, 2012, **2**, 23–33.

[201] A. Ueno, H. Yoshimura, R. Saka and T. Osa, *Journal of the American Chemical Society*, 1979, **101**, 2779–2780.

[202] I. Tomatsu, A. Hashidzume and A. Harada, *Macromolecules*, 2005, **38**, 5223–5227.

[203] Y. L. Zhao and J. Fraser Stoddart, *Langmuir*, 2009, **25**, 8442–8446.

[204] D. Wang, M. Wagner, H. J. Butt and S. Wu, *Soft Matter*, 2015, **11**, 7656–7662.

[205] R. Klajn, *Pure and Applied Chemistry*, 2010, **82**, 2247–2279.

[206] J. Voskuhl, S. Sankaran and P. Jonkheijm, *Chemical Communications*, 2014, **50**, 15144–15147.

[207] D. P. Ferris, Y. L. Zhao, N. M. Khashab, H. A. Khatib, J. F. Stoddart and J. I. Zink, *Journal of the American Chemical Society*, 2009, **131**, 1686–1688.

[208] L. Peng, M. You, C. Wu, D. Han, I. Öçsoy, T. Chen, Z. Chen and W. Tan, *ACS Nano*, 2014, **8**, 2555–2561.

[209] R. Klajn, J. F. Stoddart and B. A. Grzybowski, *Chemical Society Reviews*, 2010, **39**, 2203–2237.

[210] Z. Liu and M. Jiang, *Journal of Materials Chemistry*, 2007, **17**, 4249–4254.

[211] L. Stricker, E. C. Fritz, M. Peterlechner, N. L. Doltsinis and B. J. Ravoo, *Journal of the American Chemical Society*, 2016, **138**, 4547–4554.

[212] abcr GmbH, *Silanes, Silicones and Inorganic Silicon Compounds*, abcr GmbH, 2014, p. 656.

[213] C. Reichardt, *Solvents and Solvent Effects in Organic Chemistry*, Wiley-VCH Publishers, 3rd edn., 2003.

[214] C. Ippen, T. Greco and A. Wedel, *Journal of Information Display*, 2012, **13**, 91–95.

[215] G. Frens, *Kolloid-Zeitschrift & Zeitschrift für Polymere*, 1972, **250**, 736–741.

[216] R. Sherman and P. Adams, *Precision Cleaning 1996 Proceedings*, 1996, 271–300.

[217] H. Zheng, L. J. Mortensen and L. A. DeLouise, *Journal of Biomedical Nanotechnology*, 2013, **9**, 382–392.

[218] H. Kawauchi, K. Tuzimura, H. Maeda and N. Ishida, *Journal of Biochemistry*, 1969, **66**, 783 – 789.

[219] A. V. Bogolubsky, A. Grishchenko, S. E. Pipko, A. Konovets, A. Chuprina, A. Tolmachev, A. N. Boyko, A. Chekotylo and O. Lukin, *Molecular Diversity*, 2013, **17**, 471–477.

[220] T. Isoda, R. Maeda and A. Minohoshi, *Sensors and Materials*, 2015, **27**, 165–176.

[221] J.-L. Lagrange, *Mémoires de l'Académie royale des Sciences et Belles-Lettres*, 1773, 265–312.

Danksagung

Wie am Ende einer jeden Reise ist es an der Zeit den Menschen zu danken, ohne die diese Arbeit nicht möglich gewesen wäre:

Zu allererst muss ich Prof. Alexander Böker danken. Zum Einen für seine Entscheidung ans IAP in Potsdam zu gehen und zum Anderen, dass er sich bereit erklärte mich mitzunehmen. Es war zu Beginn nicht einfach für mich Aachen hinter mir zu lassen, aber wie es sich herausstellte, war es die richtige Entscheidung für meine Arbeit und mein zukünftiges Leben. Darüberhinaus war er immer bereit und ansprechbar, wenn es Probleme auf dem Weg gab. Vielen Dank dafür!

Ich möchte natürlich den weiteren Gutachtern dieser Arbeit danken, Prof. Ravoo und Prof. von Klitzing. Prof. Ravoo möchte ich weiterhin für die produktive Zusammenarbeit während unserer Kooperation danken. Hinzu kommen noch die restlichen Mitglieder des Promotionsausschusses: Prof. Koetz als Vorsitzender sowie Prof. Taubert und Prof. Santer die den Ausschuss vervollständigten.

Des Weiteren möchte Dmitry Grigoriev and Nikolay Puretskiy danken, die mich tagtäglich bei allen entstandenen Fragestellungen unterstützten. Zum einen bei dieser Forschung und darüber hinaus bei der gemeinsamen Bearbeitung weiterer Projekte. Ab und an musste man mir auch zeigen, dass es nicht gesund ist sich zu viel aufzuregen. Dazu gab es dann immer einen Kaffee und ein Stück Schokolade falls es nötig war! Als nächstes meine Weggefährtin Christine Schulte(-Osseili). Wir sind zusammen aus Aachen abgehauen und ich wünsche mir nichts mehr, als dass sie bald wieder zurück in ihre Heimat verschwinden darf. Du hast es dir verdient! Dazu kommen noch meine neuesten Büro-Kollegen Maria Mathieu und Falko Rottke. Ich möchte mich bei Beiden für mein faules Rumsitzen im Büro und das

bunte Bälle zeichnen entschuldigen (auch Promotion schreiben genannt). Darüber hinaus möchte ich ihnen danken, dass sie sich die Zeit genommen haben meine Arbeit zu lesen und so einige (aber bestimmt nicht alle) Fehler zu entfernen. Es gibt in unserer Gruppe noch mehr Menschen, denen ich danken muss. Ich möchte Ruben Rosencrantz für sein kontinuierlich offenes Ohr danken. Außerdem erklärte er mir alles, was irgendwie mit "Bio" zusammenhing. Die Arbeit war deutlich einfacher mit den richtigen Laborpartnern: Stefan Reinicke, Daniela John, Benjamin Stomps, Himanshu Charan, Xuepu Wang!
Weiterhin möchte ich all den Menschen aus unserem Insitut danken, die uns hier so problemlos aufnahmen, uns ständig unterstützten und halfen. Uns stellten sich viele Fragen und Probleme; ihr habt sie alle gelöst: Katrin Untch, Martin Herzberg, Anett Koch, Sylvana Blaschej, Mario Hoffmann, Matthias Förster, Petra Tersch. Außerdem möchte ich Andreas Bohn und besonders Steffi Grunst für all die TEM und SEM Aufnahmen sowie Andreas Holländer für Kontaktwinkel und XPS Messungen danken.
Ich möchte den Menschen danken, die zwar nicht aktiv an dieser Forschung beteiligt waren, aber ohne die es niemals soweit gekommen wäre. Meinen Eltern, Martina und Dieter Zimmermann, die es geschafft haben mir all die Freiheiten zu geben, die man sich nur wünschen kann. Ich hoffe, ich kann euch nun wenigstens zeigen, dass es sich am Ende gelohnt hat. Danke! Eine Danksagung ohne meine Schwester Anke wäre keine richtige Danksagung, auch wenn ich hier noch einmal betonen muss, dass sie rein gar nichts dazu beigetragen hat! Ich hoffe doch sehr, dasss wir uns in Zukunft häufiger zu Gesicht bekommen.
Und zu guter Letzt möchte ich meiner Freundin Dani danken. Dieser Ausflug nach Potsdam veränderte mein Leben und dafür bist vorallem du verantwortlich. Ich danke dir :)

Eidesstattliche Erklärung

Hiermit erkläre ich, Marc Zimmermann, dass ich die vorliegende Promotionsarbeit mit allen darin enthaltenden Zeichnungen, Grafiken, Abbildungen und Tabellen selbstständig verfasst habe. Sollte ich innerhalb dieser Arbeit den Wortlaut, die Abbildungen oder den Inhalt eines anderen Werkes benutzt haben, wurden diese Stellen unter Angabe der Quellen von mir kenntlich gemacht. Des Weiteren versichere ich, dass ich diese Arbeit an keiner anderen Hochschule eingereicht worden ist.

Potsdam, April 17, 2019